WHIPPLE 10-M TELESCOPE OBSERVATIONS OF POTENTIAL TEV GAMMA-RAY SOURCES FOUND BY THE TIBET AIR SHOWER ARRAY

by

Gary Walker

A dissertation submitted to the faculty of
The University of Utah
in partial fulfillment of the requirements for the degree of

Doctor of Philosophy

Department of Physics

The University of Utah

December 2004

ABSTRACT

An all-sky survey performed with the Tibet Air Shower Array has found a number of potential sources of TeV gamma rays. If they are steady point sources with a Crab-like spectrum, the fluxes implied should be visible with strong significance to the Whipple 10-m telescope with a short exposure. The Whipple Telescope has observed four candidates from the Tibet-II HD survey for approximately 5 hours each and one candidate from the Tibet-III Phase 1 survey for 8 hours. The analysis has failed to find a point source in any of the target regions, and upper limits of $\sim$0.2 Crab have been set.

CONTENTS

LIST OF TABLES

ACKNOWLEDGEMENTS

I would like to thank my wife, LaPriel, for her patient and loving support through nine years of school. I also acknowledge my parents and LaPriel's parents for their support.

I would like to thank my advisor, David Kieda, for his guidance, patience, and encouragement, as well as for allowing me to meet my family obligations. Thanks also to Vladimir Vassiliev for his help in the development of my analysis. I gratefully acknowledge the support of the VERITAS collaboration. Also, an allocation of computer time from the Center for High Performance Computing at the University of Utah is gratefully acknowledged.

In addition, I wish to thank the AAS, SCIENCE magazine, and IOP publishers for allowing me to reprint published figures.

This research is supported by the University of Utah and the National Science Foundation under NSF Grant #0079704. This research is also supported by grants from the U.S. Department of Energy, by Science Foundation Ireland, by PPARC in the UK, and by NSERC in Canada.

CHAPTER 1

GAMMA-RAY ASTRONOMY

1.1 Introduction

Gamma-ray astronomy, which is the study of the universe at photon energies greater than ∼100 KeV (1 KeV is 1000 electron volts), is a new and rapidly developing field. It was first pursued, at least in part, to explain the source of charged cosmic rays. Although this goal has not yet been achieved, gamma-ray astronomy has provided valuable information on high-energy processes in the universe. Past and current observations have provided spectral coverage up to 10 GeV (1 GeV=10^9 eV), and from ∼100 GeV to over 10 TeV (1 TeV=10^{12} eV), and new experiments will fill in the gap. Since gamma rays potentially exist across roughly 15 decades in energy, a variety of detection techniques is needed. Thus, gamma-ray astronomy may be subdivided according to the technique.

1.1.1 Satellites

At energies below ∼10 GeV, observations are possible only outside of Earth's atmosphere, where satellite experiments detect high energy photons directly. Above ∼10 MeV (1 MeV=10^6 eV), a photon entering a satellite detector will produce an electron-positron pair. The satellite determines the direction and energy of the incident photon by tracking the pair through the detector. At lower energies, photons are detected via Compton scattering and the photoelectric effect. Satellite detectors have almost no background because charged cosmic rays are rejected by the use of anticoincidence shielding [1].

Table 1.1 gives a partial list of past, present, and future gamma-ray satellites, listed in chronological order. SAS-2, the first in the table, operated for only six months, but it paved the way for later experiments. COS-B operated for nearly

Table 1.1. A partial list of gamma-ray satellites, past, present, and future

Name	Observation Period	Energy Range	Effective Collecting Area	Field of View
SAS-2[5]	1972-1973	30MeV - >200MeV	640 cm^2	35°
COS-B[6]	1975-1982	30MeV - 5GeV	50 cm^2	$\sim$ 20°
EGRET[7]	1991-2000	20MeV - 30GeV	1500 cm^2	0.5 SR
INTEGRAL[8]	2002-2004?	15KeV - 10MeV	2890 cm^2	9°x9°
AGILE[9]	2005-2007?	30MeV - 50GeV	$\sim$600 cm^2	3 SR
GLAST[4]	2007-2012?	10MeV - 100GeV	8000 cm^2	>2 SR

seven years and detected 25 gamma-ray sources [2]. EGRET was part of the Compton Gamma Ray Observatory, and it was very successful as it detected more than 270 high-energy gamma-ray sources [3]. GLAST, which is scheduled for launch in 2007, is highly anticipated as it will have > 30 times the sensitivity of EGRET and is expected to detect thousands of gamma-ray sources [4].

A major limitation of gamma-ray satellites is the collection area. Since satellites detect gamma rays through direct interaction, the collection area is limited to the physical dimensions of the detector, and this is constrained by launch costs. As is seen in Table 1.1, all of the satellites have a collection area of less than a square meter. The small collection area is offset by the high duty cycle and large field of view. However, as photon energies exceed 10 GeV, the gamma-ray flux (which follows an inverse power-law for most sources) becomes small enough that the satellites lose their efficacy. Therefore, the range between 10 GeV and 100 GeV is a transition region between satellites and ground-based detectors.

1.1.1.1 GRB Satellites

In addition to the satellites listed in Table 1.1, there is another class of satellites devoted to the detection of gamma-ray bursts (GRBs), a phenomenon first noticed in the 1960s. Briefly, GRBs are bursts of gamma-ray photons ranging in duration from the millisecond to the hundred second time scale. A typical burst has a dual power-law spectrum, with the spectrum steepening after the break point of $\sim$1 MeV. The flux is usually in the range of 10^{-6} erg/(cm^{-2} sec). They originate at

cosmological distances, but the source of these bursts is not yet clear [1]. BATSE, the GRB detector on the Compton Gamma Ray Observatory, detected on average one burst per day [1]. The GRB satellite HETE-2 has been operating since 2000 [10], and the SWIFT GRB satellite will be launched later this year [11]. In addition, INTEGRAL has some sensitivity to GRBs [12], as will GLAST [13], but this is not their primary mission.

1.1.2 Ground Based Detectors

At energies above ∼100 GeV, ground-based experiments provide the most effective method of detecting astrophysical sources of gamma rays. Rather than detecting the gamma ray directly, they detect the extensive air shower that is generated when the photon interacts with Earth's atmosphere (this will be discussed in more detail in Chapter 2). As is shown in Figure 1.1, the ground-based experiments may be divided into two groups. Air Cherenkov telescopes detect the Cherenkov light that is produced by the air shower, while the particle detectors detect photons and charged particles from the air shower that reach ground-level. In both cases, because detection relies on the measurement of particles in the extensive air shower, the effective collection area of the detector may be much larger than its physical dimensions.

Table 1.2 gives a partial list of ground-based gamma-ray observatories. Since the collection area depends on the gamma-ray energy, only an approximate estimate is given. However, it is clear that the collection areas for these experiments are on the order of 10^5 times greater than the satellite collection areas, allowing observations of very low flux levels. Next generation experiments such as VERITAS and HESS are designed to bridge the energy gap between satellites and ground-based instruments (10-100 GeV).

The energy range covered by the ground-based instruments is traditionally assigned the label 'Very High Energy' (VHE). The remainder of this dissertation will focus on VHE gamma-ray astronomy.

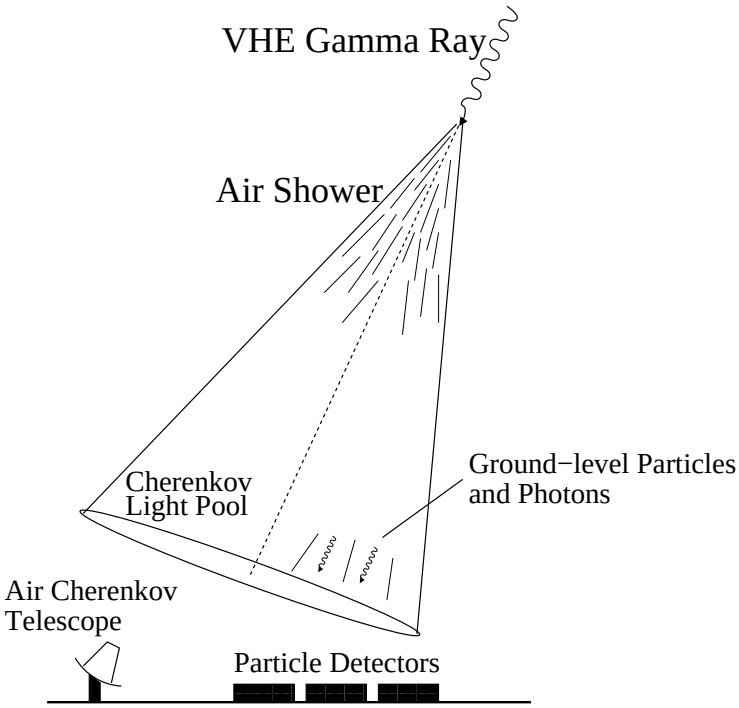

Figure 1.1. Depiction of a gamma-ray air shower. Ground-based detection of the shower is possible through both Cherenkov light and particles which reach ground level. The Cherenkov light pool has a radius of ∼120 meters at ground level [1].

Table 1.2. A partial list of ground-based gamma-ray observatories. IACT means Imaging Atmospheric Cherenkov Telescope, and PD means Particle Detector.

Name	Observation Period	Type	Energy Range	Collection Area (m^2)	Field of View
Whipple[14]	1968-	IACT	>300 GeV	$> 10^4$	2.4°
HEGRA[15]	1997-2002	IACT Array	>500 GeV	$> 10^4$	4.3°
Tibet-III[16]	1999-	PD Array	>3 TeV	22060	All-Sky
Milagro[17]	1999-	PD	4 TeV	4800	All-Sky
HESS[18]	2003-	IACT Array	>50 GeV	$> 10^5$	5°
VERITAS[19]	2006-	IACT Array	>50 GeV	$> 10^5$	3.5°

1.2 Sources of VHE Gamma Rays

Experiments such as the Whipple 10-meter telescope and HEGRA have produced valuable measurements in the VHE range, and the addition of HESS has made an immediate impact. The next generation experiments are expected to detect many VHE sources [1], but at present only a handful have been found with strong significance. Our discussion is limited to sources that were recently given the Weekes grade 'A' [20]. In the discussion, the known VHE production mechanisms will be briefly described.

1.2.1 Crab Nebula

The Crab Nebula is a strong, steady source first detected at TeV energies by the Whipple telescope in 1989 [21]. It is now considered the standard candle for VHE astronomy, and it is routinely used for instrument calibration and the development of analysis techniques. In the TeV range, the spectrum follows an inverse power law, with the differential flux J (in photons) given by

$$J = (3.2 \pm 0.17 \pm 0.6) \times 10^{-7} \times \left(\frac{E}{TeV}\right)^{-2.49 \pm 0.06 \pm 0.04} m^{-2} s^{-1} TeV^{-1},$$

as measured by the Whipple telescope [22]. The HEGRA collaboration reports detection of gamma rays from the Crab up to 80 TeV, with no break from the power-law spectrum [23].

Figure 1.2 shows differential flux measurements of the Crab from several experiments across a wide energy range. The emission below 100 MeV is thought to arise from synchrotron radiation generated by electrons with energies up to 1 PeV. For emission above 100 MeV, the prevalent theory is that high energy electrons interact with ambient photons, boosting them to VHE energies through inverse-Compton scattering [1]. Mathematical models may be used to predict the spectrum, as seen in Figure 1.2, and measurements across the spectrum are used to constrain these models. Such modelling will benefit from future measurements by GLAST and the next-generation ground based observatories.

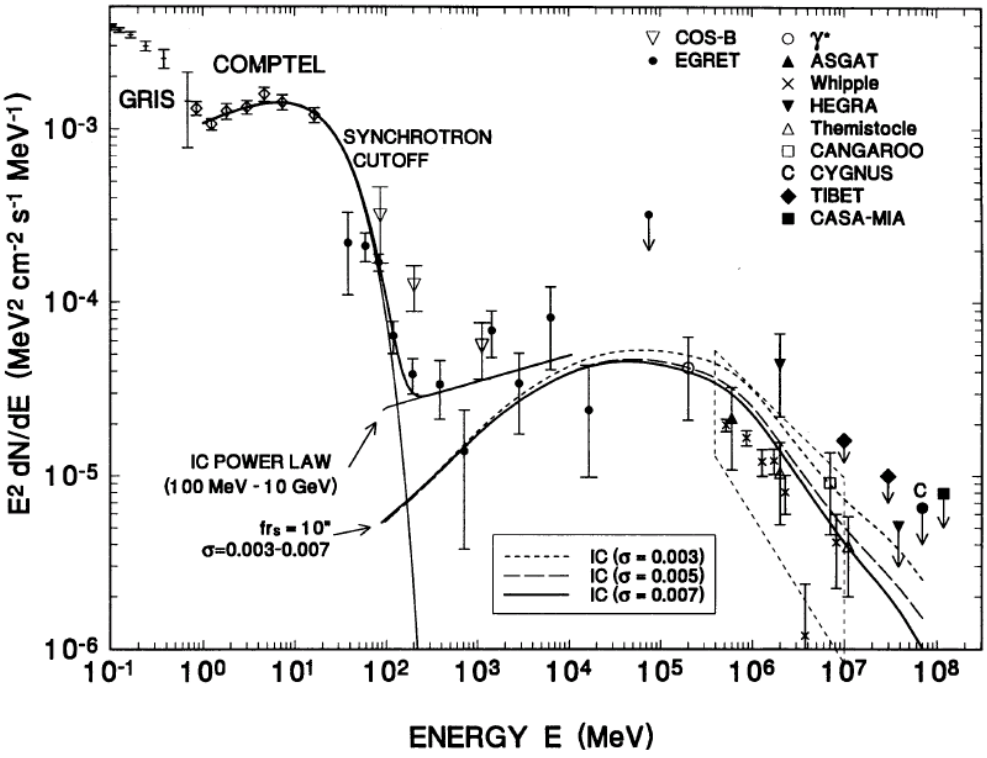

Figure 1.2. Differential flux (scaled by E^2) versus energy for unpulsed emission from the Crab Nebula. The MeV-GeV range measurements come from satellites, while measurements above 100 GeV come from ground-based experiments. Fits from several models are also shown. (Figure from [24], reproduced by permission of the AAS.)

1.2.2 Markarian 421

Markarian 421 (Mrk 421) is a blazar, which is an active galaxy with the jet axis oriented toward us. It is located at a redshift of $z = 0.031$. It was first detected at TeV energies in 1992 by the Whipple telescope [25], and it has since shown strong variability, with recorded outbursts reaching flux levels of 10 times the Crab. Moreover, the variability has been very rapid, with doubling times as short as $\sim$15 minutes [26].

Figure 1.3 shows the photon spectral energy density plot for Mrk 421. In it, the two-humped structure common to blazars can be seen (it is also similar to the Crab). It is widely accepted that the emission is powered by accretion onto a supermassive black hole, from which relativistic jets emanate [1], as seen in Figure

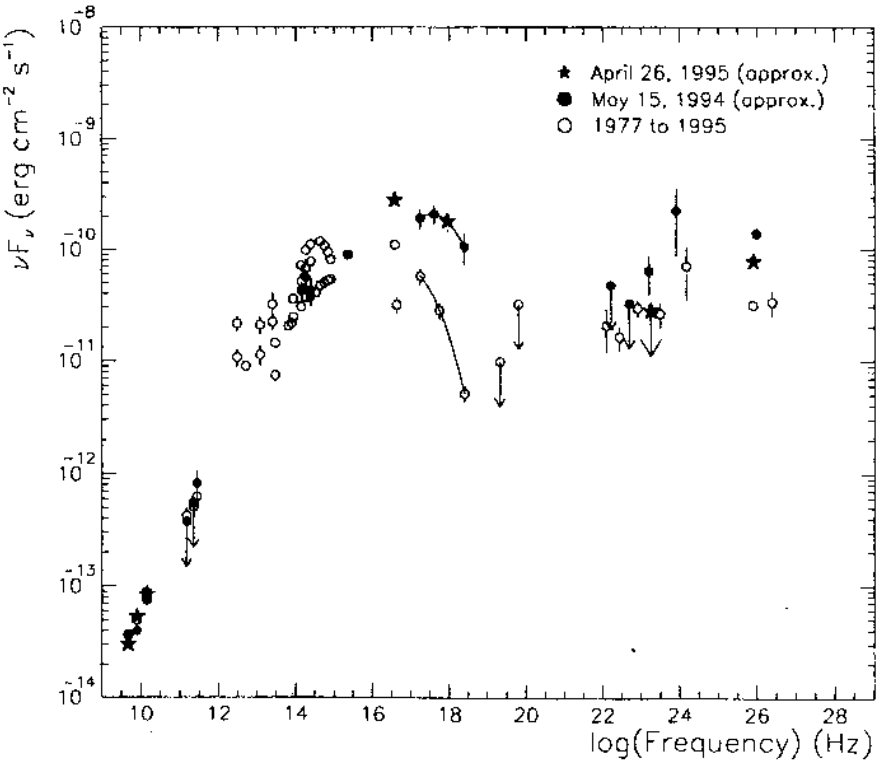

Figure 1.3. Spectral energy distribution for Markarian 421 across a range of energies. The two-humped structure typical of blazars can be seen. (Figure from [27], reproduced by permission of the AAS.)

1.4. The models for this emission may be categorized as either leptonic or hadronic.

In the leptonic models, the low energy hump is due to synchrotron radiation produced by electrons in the jet moving through the magnetic fields within the jet. The high energy hump is due to the inverse-Compton scattering of seed photons from these relativistic electrons. The seed photons may be the original synchrotron photons, or they may come from regions external to the jet. Some models include a combination of the two sources [1].

The hadronic models suggest that protons in the relativistic jet are primarily responsible for the observed radiation. The protons interact with photons or other protons to produce particle cascades (including the π^0 meson), and so VHE radiation may be produced by $\pi^0 \rightarrow \gamma + \gamma$. The low energy bump is produced by protons and charged cascade particles as synchrotron radiation. Alternatively,

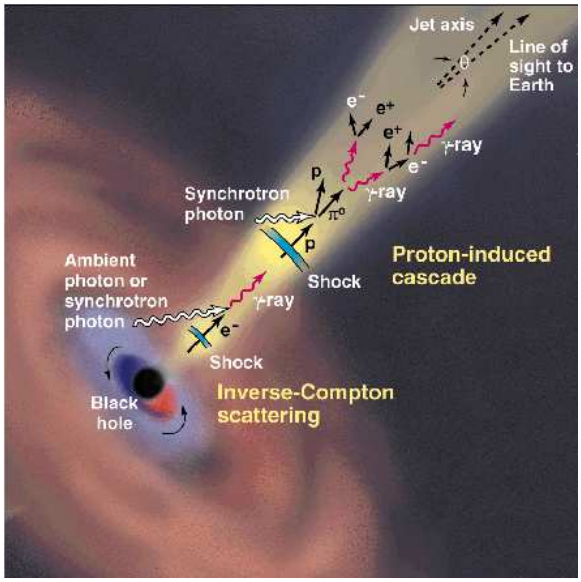

Figure 1.4. Depiction of a supermassive black hole at the center of an AGN. (Reprinted with permission from [Buckley, SCIENCE 279:676-677 (1998)]. Illustration by K. Sutliff. Copyright 1998 AAAS.)

some models predict that ultra-high energy protons ($\sim 10^{20}$ eV) can produce TeV photons via synchrotron emission [1].

Observational results from Mrk 421, particularly the rapid flux changes, put difficult constraints on both the leptonic and hadronic models, but neither is ruled out. However, the leptonic models are currently more favored [1].

1.2.3 Markarian 501 and Other Blazars

Markarian 501, a blazar at a redshift of $z = 0.034$, was the third TeV source discovered. It was detected in 1995 by the Whipple telescope at approximately 0.1 Crab [28], and in a 1997 flare it displayed rapid, large amplitude flux variability [29]. Like Mrk 421, the spectral energy density has two humps, and the production mechanisms appear to be similar to that of Mrk 421 [1].

Other 'A' list blazars include 1ES2344, 1ES1959, PKS2155, and H1426:

- 1ES2344 is at a redshift of $z = 0.044$. It was detected on a single night by the Whipple telescope at the 6σ level in 1995, with a flux of about 0.6 Crab.

In data taken during the months surrounding that night, it was seen at the 4σ level [30]. The HEGRA group has also reported a detection [31].

- 1ES1959 is at a redshift of $z = 0.048$. It was first detected by the Telescope Array in 1999 [32]. In 2002, it was seen to flare to the 5 Crab level. The quiescent flux is reported to be about 0.05 Crabs [20].

- PKS2155 is a southern hemisphere source, lying at a redshift of $z = 0.116$. It was first detected in 1999 by the Durham group [33]. Because of the large redshift, this source is of interest for the study of the extragalactic background light (EBL), which limits the propagation of TeV photons [34]. Results from HESS, which had a 45σ detection, are as yet inconclusive with regards to the EBL [35].

- H1426, which is the most distant 'A' source, lies at a redshift of $z = 0.129$. In 2002, Whipple reported a detection at the 5.5σ level [36], and detection has since been reported by two other groups. The observed source strength is around 0.06 Crab [20]. Like PKS2155, H1426 is of interest for EBL studies because of its large distance.

1.2.4 RX J1713.7-3946

RX J1713.7-3946 is a shell-type supernova remnant, and TeV detection was first claimed by the CANGAROO group [37]. The HESS group has recently reported detection at the 20σ level [38], with a flux of 0.66 Crab, and a spectral index of -2.2. The excess is spread in clumps across a region of $\sim 1^\circ$, and there appears to be a strong spatial correlation with x-ray data (ASCA, XMM-Newton). The correlation suggests that the TeV emission is due to inverse-Compton scattering from high energy electrons. This result is important since it fails to confirm RX J1713.7-3946 as a source of cosmic ray protons (galactic cosmic rays are thought to originate in supernova remnants).

1.2.5 Other Sources

In addition to the sources listed above, it is worth mentioning TeV2032, PSR B1259-63, and the Galactic center:

- TeV2032 was found serendipitously by the HEGRA group after a 2-dimensional search of a long exposure of the Cygnus region [39]. The excess was 4.6σ, posttrials, the spectral index was found to be -1.9, and there was evidence for spatial extension. The source of the gamma rays is not yet clear, but it may be associated with the Cygnus OB2 cluster of hot, massive stars. The Whipple group has been working to confirm the detection [40], but the analysis is incomplete.

- PSR B1259-63 is a binary system comprised of a pulsar bound to a massive Be-star. It was detected at TeV energies by HESS at about 0.05 Crab in early 2004 [41]. The rate was found to depend on the orbital position, with the preperiastron rate $\sim$two times higher than the postperiastron rate. VHE production is assumed to be due to Compton upscattering of the Be-star photons.

- The Galactic center has been observed by many VHE experiments [42, 43], but the most definitive result comes from HESS, which has detected VHE emission at the 9σ level [44]. The measured flux is roughly 0.05 Crab, although some variability could be present. The spectral index measured by HESS is -2.2. There is strong interest that the TeV gamma-ray emission could be due to neutralino-antineutralino annihilation in a dark matter cusp at the center of the galaxy [45]. However, the production mechanism is still not clear, and so a longer exposure is needed [46].

- Correlations found between two all-sky TeV gamma-ray surveys [47, 48] seem to suggest the existence of one or more new, unidentified TeV sources [49]. In data from Milagro, one of these potential sources appears to be extended [50], but the emission mechanism (if the source is real) is unknown.

1.3 Searching for New Sources

As has been noted, there are currently only a handful of known TeV gamma-ray sources. Since observations of these sources have produced valuable results, there is a continual effort to detect new sources. The Tibet Air Shower Array (Tibet AS), which is briefly described in Table 1.2, has produced an all-sky survey in which the positions of 18 unidentified gamma-ray source candidates are reported [47]. The majority of these candidates are probably due to statistical fluctuations (i.e. they are not real sources), but it is possible that one or more of the candidates is a real gamma-ray source. If there is a real source, the implied flux levels should be visible to the Whipple 10-meter telescope (the Whipple telescope) with only a short exposure. In light of these facts, five gamma-ray source candidates from the Tibet AS all-sky survey were chosen for follow-up observation with the Whipple telescope.

The remainder of this dissertation focuses on the Tibet AS all-sky survey and the Whipple telescope follow-up observations. Chapter 2 discusses the development of gamma-ray and hadronic air showers to lay the ground work for the detection techniques of the Whipple telescope and Tibet AS, which are described in more detail in Chapter 3. Chapter 3 also discusses the Tibet AS all-sky survey and the five targets for follow-up observation with the Whipple telescope. The analysis of the Whipple observations is addressed in Chapter 4, while the results are discussed in Chapters 5 and 6.

CHAPTER 2

GAMMA-RAY AIR SHOWERS

The remainder of this dissertation deals with the Whipple 10- meter telescope (hereafter referred to as the Whipple telescope) and the Tibet Air Shower Array, which are ground-based experiments. It is therefore worthwhile to discuss the development of gamma-ray air showers, since both experiments rely on these showers for detection. As cosmic-ray hadrons present a large background, hadron-induced air showers will also be discussed.

2.1 The Atmosphere

Since the atmosphere plays a critical role in the development of air showers, a brief overview is useful. In a simple approximation, the density of the atmosphere may be described as

$$\rho(h) = \rho_0 e^{-\frac{h}{h_0}}$$

where h is the altitude above sea level, and ρ_0 is the density at sea level. The scale height, h_0, is approximately 7 km, but is somewhat dependent on the altitude. The amount of matter that a particle or photon sees as it travels an incremental distance $dx = dh/\cos(Z)$, where Z is the zenith angle, is $\rho(h)dx$, with units of [g cm^{-2}]. The atmospheric depth D is the amount of matter transversed from altitude h to infinity:

$$D = \int_h^\infty \rho(h)dx.$$

Again, the units are [g cm^{-2}]. When a particle or photon enters the atmosphere, the location of first interaction is typically given in terms of atmospheric depth,

and similarly, secondary particle interaction lengths are given in units of [g cm^{-2}]. The formula

$$h(D) = h_0(D) \ln\left(\frac{1030}{D}\right),$$

where $h_0(D) = 6200 + 2.2D$, may be used to convert the atmospheric depth D to altitude h along a vertical path. Here, $h(D)$ and $h_0(D)$ are given in meters [51].

2.2 Gamma-Ray Air Showers

When a VHE photon enters the atmosphere, it usually interacts with a nucleus via pair production, transferring some momentum to the nucleus while converting to an electron-positron pair. In the process, most of the photon energy is given to the electron pair. The radiation length for pair production at VHE energies is 37.1 g cm^{-2}, which corresponds (vertically) to a first-interaction altitude of about 20 km [1]. The average emission angle of the electron pair is on the order of $\theta \sim (0.511 MeV)/E_\gamma$ [52]. For VHE photons, $\theta \sim (0.511 \times 10^6)/10^{12} = 10^{-6}$ rad, so that the pair travels along nearly the same line as the original photon.

As the electron/positron pair travels, each particle will emit bremsstrahlung photons as they interact with atoms in the air. These photons are again of high energy, and so they will pair produce, and thus a particle cascade, or air shower, is generated. As the number of particles in the shower increases, the energy per particle decreases. The shower reaches its maximum development when the average energy emitted through bremsstrahlung radiation becomes equal to the energy lost to ionization of the air [1].

An air shower induced by a gamma ray or an electron (which is indistinguishable from a gamma-ray shower) is classified as an electromagnetic (EM) cascade. In 'Approximation B' of standard EM shower theory [51], the number of charged particles at shower maximum is given by

$$N_{max}(E_0) = \frac{0.31}{\sqrt{\ln(E_0/\epsilon_0) - 0.18}} \frac{E_0}{\epsilon_0},$$

where E_0 is the original photon energy, and ϵ_0, the ionization loss per radiation length, is 84.2 MeV. The atmospheric depth of shower maximum is given by

$$t_{max}(E_0) = 1.01[\ln\left(\frac{E_0}{\epsilon_0}\right) - \frac{1}{2}],$$

where t_{max} is the atmospheric depth in units of radiation length [51]. Applying these equations, for a 1 TeV incident photon, the average number of particles at shower maximum is ∼1200 particles. For the same energy, the average depth of shower maximum is ∼330 g cm^{-2}, which corresponds to an altitude of ∼8 km for vertical incidence.

2.3 Hadron Air Showers

When a VHE hadronic cosmic ray enters the atmosphere, it will interact with nuclei in the air. At 10^{15} eV, the interaction length is 70 g cm^{-2} for protons and 15 g cm^{-2} for iron nuclei [53], corresponding to average first interaction heights of 17 km and 26 km for vertical incidence. As explained by Rao and Sreekantan, the primary interaction produces a spray of nuclear particles (protons, neutrons, alpha, etc.) and mesons (pions, kaons, etc.), with pions being the most numerous. The nuclear particles continue along the path of the primary particle, participating in further interactions. The three varieties of pions are produced with approximately equal probability. The charged pions ($\pi^{\pm}$) either decay, producing muons and neutrinos, or they interact again, producing more hadronic secondaries. The neutral pions (π^0) decay immediately into two gammas (though at extremely high π^0 energies, time dilation makes interaction possible), and these gammas produce EM cascades. Thus, the hadron-induced shower may be thought of as a hadronic core surrounded by muons and EM showers that are produced along the way [51].

The average number of particles may be approximated by

$$N_{max}(E_0) = 0.045\left(\frac{E_0}{0.074}\right)$$

and is approximately independent of the mass of the primary. Here, E_0 is in units of GeV. The average atmospheric depth of shower maximum for a proton is given by

$$D_{max}(E_0) = 36\ln\left(\frac{E_0}{0.074}\right) - 70,$$

where E_0 is in units of GeV, and D_{max} has units of [g cm^{-2}]. For a cosmic-ray nucleus of mass number A, shower maximum is $35.7 \ln(A)$ g cm^{-2} higher relative to a proton of the same energy [51]. According to these equations, an air shower caused by a 1 TeV proton has on average 610 particles at shower maximum, which is about half the number for a gamma-ray shower of the same energy. The shower maximum occurs at an average atmospheric depth of 270 g cm^{-2}, corresponding (vertically) to an altitude of $\sim$9 km.

2.4 Comparison: Gamma Ray versus Hadron

A great difficulty in VHE gamma-ray astronomy is the background of charged cosmic rays, which outnumber gamma rays by a factor of $\sim 10^4$. It is therefore desirable to find ways to reject showers initiated by cosmic ray nuclei while retaining most of the gamma ray showers. The simplest method of differentiation is to determine the arrival direction of the initial photon or nucleus (for both gamma-ray showers and hadron showers, the arrival direction of the initial photon may be determined with reasonable accuracy). Because of the Galactic magnetic field, the arrival direction of charged cosmic rays has been randomized and is thus isotropic, except perhaps at extremely high energies. In contrast, gamma rays emitted by a point source have a common origin. Therefore, accurate determination of the primary arrival direction may be used to enhance the signal from a gamma-ray point source. (This strategy is less effective for a diffuse source.)

In addition to directionality, a number of differences between gamma-ray and hadron showers make further discrimination possible. Foremost among these is the spread of the shower perpendicular to the shower axis, as illustrated in Figure 2.1. In a gamma-ray shower (EM cascade), a small lateral spread is caused by multiple Coulomb scattering of the charged particles. In a hadron shower, multiple EM cascades are spawned by π^0 production in the shower core. These pions are produced with a large momentum (around 400 MeV/c) perpendicular to the shower axis [51]. This large transverse momentum, coupled with the production of multiple EM cascades, makes hadron showers broad and patchy compared to gamma-ray

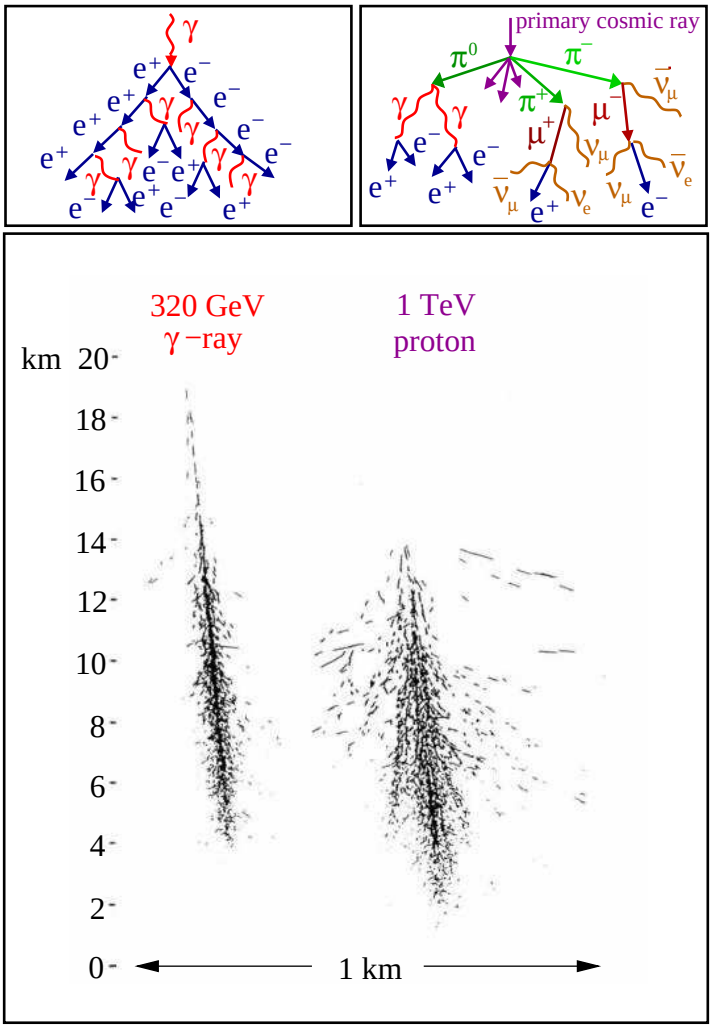

Figure 2.1. Simulated gamma-ray and proton air showers. The top frame depicts typical interactions for each shower. Note the large lateral spread of the proton shower. (Figure from [1], reproduced by permission of IOP Publishing.)

showers, which tend to be smooth and compact.

Another difference between photon and hadron showers is muon production. In an electromagnetic shower, muon production is possible via pair production or nuclear photodisintegration, but these are unlikely. In contrast, hadronic showers contain many muons due to $\pi^{\pm}$ and $K^{\pm}$ decay [51].

One more difference of note is the amount of Cherenkov light that is produced as the shower moves through the atmosphere (see below for a discussion of Cherenkov

light). As is noted in the next section, electrons with energies down to ∼20 MeV are capable of causing Cherenkov emission, while the threshold for muons and protons is considerably higher. This means that electrons and positrons are largely responsible for the Cherenkov light generated during an air shower. In a gamma-ray shower, nearly all of the particles produced are electrons and positrons. In a hadron-induced shower, electrons and positrons are produced via π^0 decay, but in smaller numbers since only 1/3 of the pions are π^0. As a result, gamma-ray showers produce two to three times as much Cherenkov light as hadronic showers of the same energy [1].

Figure 2.2 shows a simulated gamma shower with a simulated proton shower, both at 1 TeV, as seen by the Whipple telescope camera. The gamma shower is smooth and compact, while the proton shower is fragmented and contains less light. The fragmentation is due to multiple EM showers spawned by π_0 decay.

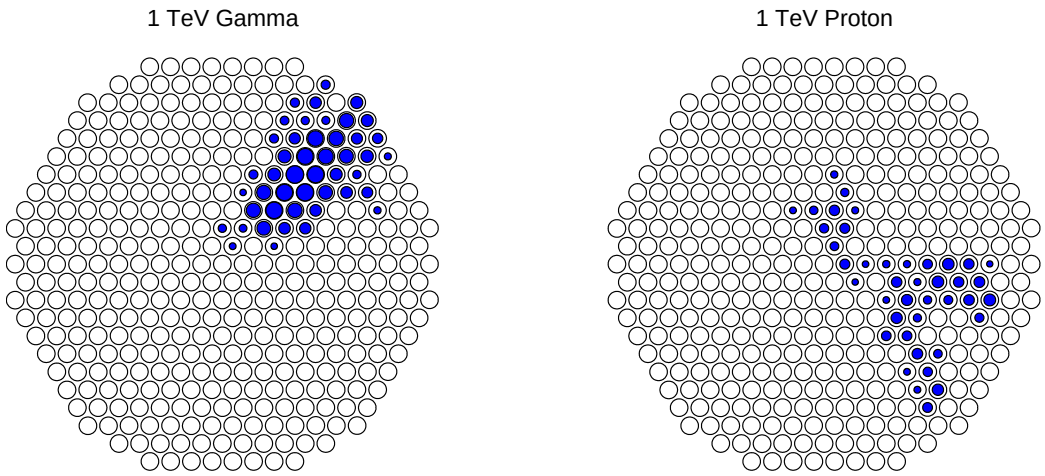

Figure 2.2. Simulated 1 TeV gamma-ray and proton air showers as viewed by a simulated Whipple telescope camera centered on the source point. The impact parameter, which is the perpendicular distance between the shower axis and the telescope, was 80 meters for both primaries. The zenith angle was 20° in each case. The fragmentation of the proton shower indicates that several small, separate electromagnetic showers occurred.

2.5 Cherenkov Radiation

When a charged particle moves through a dielectric, such as air, the dielectric surrounding the charge become polarized, as illustrated in Figure 2.3. After the particle passes by a point on the path, radiation is possible as the polarization relaxes. However, if the particle moves slowly, as in the left frame, the surrounding polarization is approximately spherical. As a result, there is no residual electric field, and no light is produced. Conversely, if the charged particle moves faster than the speed of light in the medium, the particle outruns the effects of its own electric field. This causes an asymmetry in the polarization along the path of the particle, and thus radiation is possible [1]. This phenomenon is known as Cherenkov radiation.

The angle of Cherenkov emission may be derived using simple trigonometry. Figure 2.4 shows a charged particle moving through a medium, causing light to be emitted along the way. The wavefronts emitted at various points form the line which defines the emission angle θ, given by

$$\cos\theta = \frac{c}{vn}$$

Here, v is the velocity of the particle, n is the index of refraction of the medium, and c/n is the speed of light in the medium. For $v \approx c$, $\cos\theta = 1/n$, while the threshold velocity (corresponding to $\theta = 0$) is $v_{\mathrm{t}} = c/n$. Using the relativistic energy formula $E = \gamma mc^2$, where $\gamma = 1/\sqrt{1-(v/c)^2}$, the energy threshold for Cherenkov radiation is

$$\frac{E_{\mathrm{t}}}{mc^2} = \frac{1}{\sqrt{1-(1/n)^2}}.$$

Thus, for a given index of refraction, the energy threshold is directly proportional to the mass of the charged particle. For electrons, muons, and protons at sea level, the Cherenkov threshold energy is 21 MeV, 4.4 GeV, and 39 GeV, respectively.

At sea level, $n = 1.000292$, so that $\theta_{\max} = 1.3°$. Alternatively, n may be written as $n = 1+\eta$, so that for $v \approx c$,

$$1 - \frac{\theta^2}{2} = \frac{1}{1+\eta} \approx 1 - \eta,$$

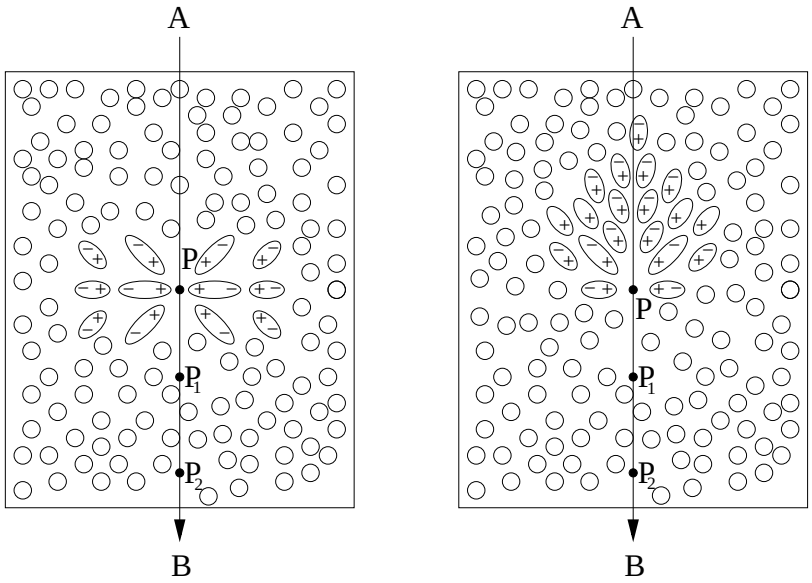

Figure 2.3. Polarization surrounding a charged particle moving through a dielectric medium. On the left, the particle is moving slowly, and the symmetry prevents the emission of light. On the right, the particle is moving faster than the speed of light in the medium. In this case, radiation is emitted because of the asymmetric polarization. (Figure from [1], reproduced by permission of IOP Publishing.)

where $\cos\theta$ was replaced by an approximation appropriate for small θ. Thus, $\theta_{\max} = \sqrt{2\eta}$. Finally, η can be approximately expressed in terms of atmospheric depth D by

$$\eta = 0.000292 \left(\frac{D}{1030}\right) \left(\frac{273.2^\circ K}{(204 + 0.091D)^\circ K}\right),$$

where D is in units of [g cm^{-2}] [51].

The rate of emission per unit length between wavelengths λ_1 and λ_2 is

$$\frac{dN}{dl} = 2\pi\alpha(\frac{1}{\lambda_2} - \frac{1}{\lambda_1})\sin^2\theta \approx 4\pi\alpha\eta(\frac{1}{\lambda_2} - \frac{1}{\lambda_1}).$$

Here, α is the fine structure constant, θ is the angle of emission, and the unit length is the same as is used for the wavelengths. Thus, the emission increases with shorter wavelength. For a relativistic charged particle at sea level, ~ 230 photons are emitted per g cm^{-2} between 350 nm and 500 nm [51].

For a gamma-ray shower, the Cherenkov light arrives at ground level as a disk of photons about 3 nanoseconds thick with a radius (at mountain altitudes, or $\sim$2000

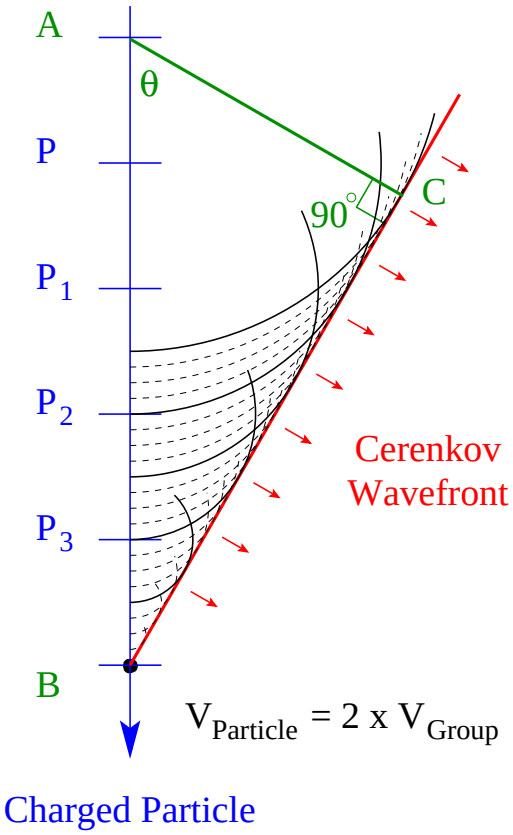

Figure 2.4. Formation of the Cherenkov wavefront due to a charged particle moving through a dielectric medium. In the time the particle moves from point A to point B, the light from point A travels to point C. The Cherenkov angle θ is found using the right triangle. (Figure from [1], reproduced by permission of IOP Publishing.)

meters) of ∼120 meters [54]. The intensity of the Cherenkov light is approximately constant within the disk (∼100 photons/m^2 for a 1 TeV gamma ray), while beyond 120 meters it drops off quickly. While the photon density is quite low, the Cherenkov light can be efficiently observed with a large light collector coupled to a fast detector, such as the Whipple telescope [55]. Referring again to Figure 2.2, the left figure shows the Cherenkov light from a simulated 1 TeV gamma-ray shower, as imaged by the Whipple telescope camera. The the length of the image (i.e., the long axis), corresponds to path of the air shower down through the atmosphere. The width of the image corresponds to the lateral distribution of particles about the shower

axis. This gamma ray originated at the center, and so the part of the image closest to the camera center is from the top of the atmosphere, while the light at the edge of the camera is from a lower altitude. As can be seen in the figure, Cherenkov imaging can provide both hadron rejection and accurate directional information.

CHAPTER 3

THE WHIPPLE TELESCOPE AND THE TIBET AIR SHOWER ARRAY

3.1 Whipple 10-meter Telescope

The Whipple 10-meter telescope (hereafter referred to as the Whipple telescope), shown in Figure 3.1, is located south of Tucson, Arizona at an elevation of 2320 meters. The reflector is made of segmented mirrors in the Davies-Cotton design, and, as the name implies, has a 10-meter aperture. The focal length is 7.3 meters [55], and a camera made of photomultiplier tubes (PMTs) is in the focal plane. There have been a number of different configurations for the camera over the years, but the present camera, shown in Figure 3.2, has been in use since 1999. In the inner camera, 379 PMTs (13mm) are in a close-packed arrangement with 0.12° spacing, giving a 2.6° field of view. Reflective light cones (not shown in the figure) have been placed in front of the PMTs to fill in the dead space between the PMTs [56]. The outer 28mm PMTs were never successfully integrated into the analysis and were removed in 2003. The analysis presented in Chapter 4 uses only the inner pixels.

3.1.1 Data Collection and Processing

The Whipple telescope operates only on dark, moonless nights (duty cycle $\sim$ 10%). During operation, there are two modes of observation. In ON/OFF mode, the telescope collects data from both the ON-source region and an OFF-source region, while in TRACKING mode, no OFF-source data are collected (this will be explained in more detail in Section 3.1.3). Observations of each field (ON or OFF) are made in 28-minute segments, known as runs.

Figure 3.1. The Whipple 10m telescope.

Figure 3.2. The Whipple camera in its 1999-2003 configuration. The large outer PMTs were removed in 2003, but the inner camera remains the same.

During each run, the reflector images light onto the camera, where the light is converted to electrical signals by the PMTs with an efficiency of $\sim 20\%$. The signal from each PMT is amplified and split, with one component going through a delay line to the analog to digital converter (qADC), and the other going through a constant fraction discriminator to the trigger electronics. (A trigger is needed to differentiate a real signal from an air shower (many PMTs fire simultaneously) from random noise. The trigger initiates the readout of the image by the electronics as well as the storage of the data in the computer.) A pattern selection trigger was installed in 1998 and was set to a threefold coincidence for the data in question. Thus, when at least three neighboring PMTs rise above a pre-determined threshold, the trigger is invoked [57]. When triggered, the qADC opens a 20 ns gate which integrates the amplified charge signal over this time. The event is stored in the run file as the number of digital counts in each pixel, along with the event time. (Hereafter, digital counts is referred to as ADCs, and the term pixel refers to the PMT plus all of the electronics behind it.) The typical trigger rate is $\sim$ 15-30 Hz.

All of the data collected during a run are stored in a single file (one file per run). In addition to event data, the run file contains telescope pointing information, an estimate of the weather quality, and other useful information. The weather quality is assigned a grade of 'A'(-), 'B'(+/-), or 'C'(+/-) by the observers who operate the telescope, with 'A' meaning perfect weather and 'C' meaning completely overcast (this estimate is obviously subjective, but it is meant as a guide).

Low-level data processing, which is performed on the stored run files, consists of the following steps:

- Pedestal Subtraction: In the post-PMT electronics, each qADC channel is kept at a small positive offset, called the pedestal, to allow for negative fluctuations in the night sky background (NSB). The pedestal and NSB are calculated using noise events, which are randomly-triggered (i.e., not triggered by an air shower) snapshots recorded at a rate of 1 Hz. For a given pixel, the pedestal is the mean number of ADCs during the noise events, while the NSB is related to the standard deviation about the mean. The pedestal for

each pixel is about 20 ADCs, while the NSB (noise) is around 4 ADCs if no stars are present. The pedestal for each pixel is subtracted from the signal for each event.

- Padding: When corresponding OFF-source data are used to estimate the ON-source background, differing NSB levels between the ON and OFF fields can introduce a bias when the analysis is applied. Padding attempts to correct for this. The NSB values are compared between the two fields on a pixel by pixel basis, and artificial noise is computationally added to the quieter pixel according to the equation

$$N_{\mathrm{add}} = RG\sqrt{N_{\mathrm{n}}^2 - N_{\mathrm{q}}^2}.$$

  Here, N_{n} is the NSB in the noisier pixel, N_{q} is the NSB in the quieter pixel, and RG represents a random number pulled from a Gaussian distribution with a mean of 0 and a standard deviation of 1. Thus, the noise levels are approximately equalized between the ON and OFF fields [58].

- Cleaning: The NSB causes fluctuations in individual pixels that are unrelated to the shower image. To reduce the effects of this, each event must be cleaned, and in this analysis the events are cleaned on a pixel by pixel basis. For a given event, the signal in each pixel is compared to the NSB. Pixels with signals above 4.25σ, where σ is the NSB for that pixel, pass the cleaning. In addition, pixels above 2.25σ are saved if they border a 4.25σ pixel. Figure 3.3 is shown as an example. Note that when padding is involved, cleaning is applied at the padded noise level.

- Flat-Fielding: The gain of each pixel, relative to the rest of the camera, is calculated using the cosmic-ray background (which should be isotropic across the camera). The signal in each pixel is then scaled according to that pixel's gain.

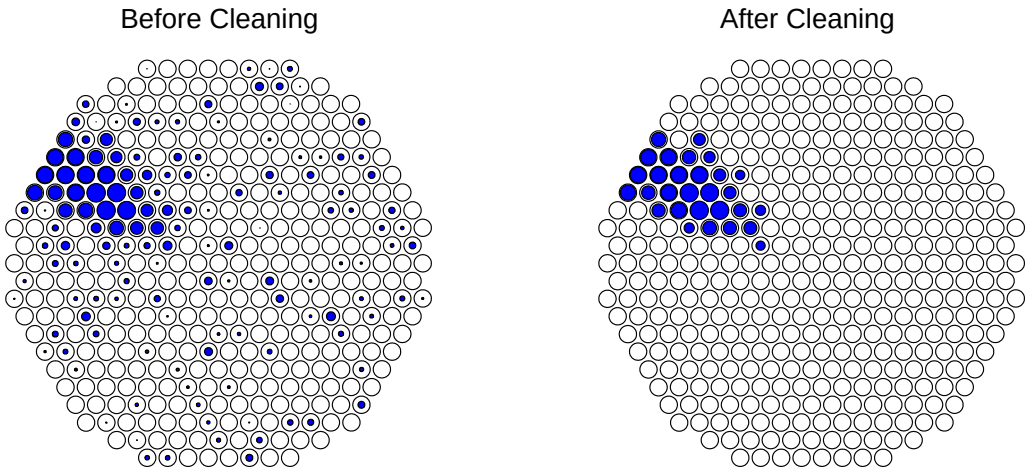

Figure 3.3. A real image before and after cleaning. Note that the pedestals have already been subtracted.

3.1.2 Standard Analysis

After the low-level processing (described above) is completed, each event image is parameterized. Moment analysis is used to find the centroid, *Length*, *Width*, and angle (with respect to the camera axes) of each image. The *Length* and *Width* are the second moments of charge along the image axes. Other image parameters include *Max1* and *Max2*, the two brightest pixels, *Distance* and *Alpha*, which are calculated with respect to the center of the camera, and *Size*, which is the total charge in the image. Figure 3.4 illustrates the parameters *Length*, *Width*, *Distance*, and *Alpha*.

In the analysis, cuts are made on the *Width* and *Length* to eliminate a large part of the background. This is possible because gamma-ray air showers tend to be more compact than hadron-induced showers, as was explained in Chapter 2. Further discrimination is achieved with a *Length*/*Size* cut, which reduces the local muon contribution, and a *Distance* cut. Finally, since event images point back to the source location, an *Alpha* cut is applied (this assumes a point-source at the center). The standard cuts, known as Supercuts [59], are listed below:

- $Max1\,, Max2 > 30 ADC$

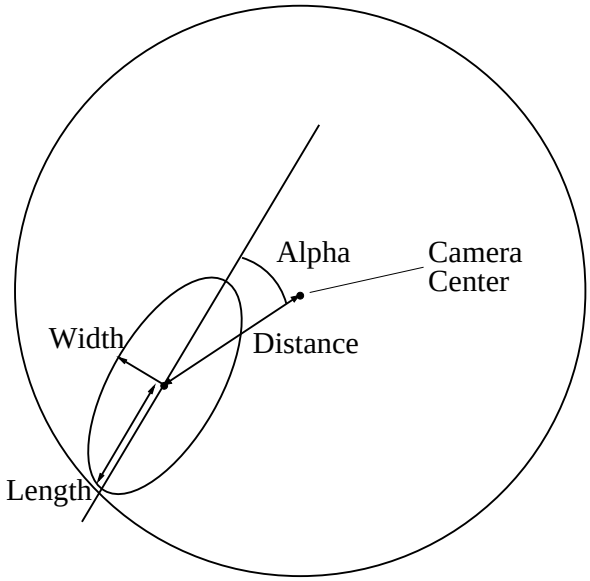

Figure 3.4. The image parameters *Length*, *Width*, *Alpha*, and *Distance*.

- $Length/Size < 0.0004[deg/ADC]$
- $0.13^\circ < Length < 0.25^\circ$
- $0.05^\circ < Width < 0.12^\circ$
- $0.4^\circ < Distance < 1.0^\circ$
- $Alpha < 15^\circ$

3.1.3 Background Estimation

As was noted in Section 3.1.1, the Whipple telescope has two modes of observation, corresponding to two types of background estimation. In ON/OFF mode, the telescope collects data from both the ON-source region and an OFF-source region. The OFF field is at the same Declination as the ON, but it is offset by 30 minutes in Right Ascension (RA), either before or after. For example, if OFF follows ON, the telescope tracks the ON position for 28 minutes, leaving 2 minutes to slew to the OFF position. The OFF position is then tracked for 28 minutes, so that the telescope tracks through exactly the same part of the local sky for

both exposures. This way, the OFF data may be used to estimate the ON-source background. Figure 3.5 shows the *Alpha* plot for 20 ON/OFF pairs on the Crab Nebula, after the other Supercuts2000 were applied. The ON-OFF excess in the signal region ($Alpha < 15°$) is 18σ using the Li and Ma method [60].

In TRACKING mode, no OFF data are collected. Instead, the background in the signal region is estimated using the region $20° < Alpha < 65°$ in the ON-source data. As is seen in Figure 3.5, the OFF *Alpha* plot is relatively flat, and so such an estimate is reasonable. The scaling factor, known as the tracking ratio, is calculated using many OFF runs. The tracking ratio is typically slightly larger than 3, but the value is known to change over time. The data shown in Figure 3.5 are all from the same period, during which the tracking ratio was calculated to be 3.03. Thus, if the ON data are treated as TRACKING data, the calculated excess is 20σ.

3.2 Tibet Air Shower Array

The Tibet Air Shower Array (Tibet AS), shown in Figure 3.6, has been operated since 1990 by the TibetASγ collaboration [61]. It is an array of particle detectors

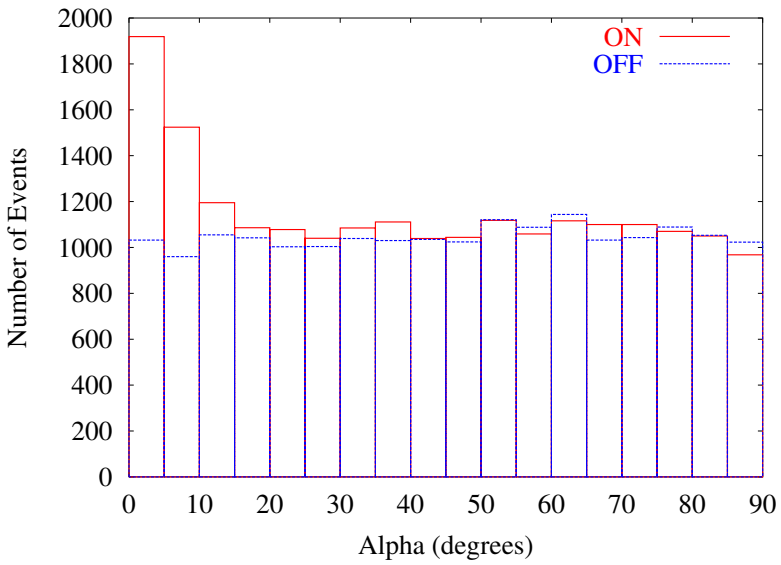

Figure 3.5. *Alpha* plot for 20 ON/OFF pairs (9.3 hours on-source) taken with the Crab Nebula on-axis. All of the Supercuts2000 have been applied, except for *Alpha*. The excess in the first 3 bins is 18σ.

Figure 3.6. The Tibet Air Shower Array, in its 1999-2002 state. (Figure: http://www.icrr.u-tokyo.ac.jp/em/tibet_exp/gallery/exp/view/kawata/array.jpg)

located in Tibet at 90.53° E., 30.11° N., at an elevation of 4300 m. Each particle detector is a 0.5 m^2 scintillator, coupled to a fast-timing PMT. A 5-mm lead plate is placed on top of each scintillator to allow the detection of air shower photons. The Tibet II HD array, which operated from 1996 to 1999, achieved a 5175 m^2 area using 109 detectors on a 7.5-m grid. The upgrade to Tibet III began in 1999, and by 2001, it included 533 detectors with the same spacing to cover an area of 22050 m^2. For both detectors, the angular resolution of individual showers is 0.9° and the mode energy is 3 TeV for proton showers [61, 62].

Tibet AS has a field of view of over one steradian, and the duty cycle is nearly 90%. Gamma-ray sources are seen as an excess above the large but isotropic cosmic-ray background. The Tibet II HD array detected the Crab Nebula and Markarian 501 [61, 63], while Tibet III has detected the Crab and Markarian 421 [64].

3.2.1 All-Sky Survey

A wide angle survey was conducted with the Tibet II HD array on data taken between February 1997 and October 1999 [47]. During this period, the array ran at a trigger rate of 115 Hz, but only events with zenith angle less than 30° were included in the survey. The sky was divided into 0.1° RA by 0.1° Declination bins,

and the events were binned accordingly. A 1° radius search window, as shown in Figure 3.7, was used to look for potential gamma-ray sources. For a particular point in the sky, the small bins within or in contact with the search window constituted the signal for that point. The background was estimated using twenty similar 1° windows at the same Declination but offset in RA, with ten taken from each side. The background windows were separated from each other by 2° in RA. The Tibet group found that the cosmic-ray distribution was not uniform in RA, and so rather than just averaging the background windows, a 2nd order polynomial fit was used [47].

The search was performed between 10° and 50° Declination and covered all RA values. The search increment was 0.1° along each axis (not true angle in RA). In the search, the Crab Nebula was detected with a significance of 4.8σ. In addition, 18 other locations with significance above 4σ were found. The Tibet group noted that these may be explained as statistical fluctuations [47]. However, it should also be noted that statistics would allow one or more of these locations to be a real source with a flux near the sensitivity limit of Tibet AS. (Recently, correlations were found between this survey and a sky survey by Milagro, and so it is likely that one or more is a real source [49].)

In order to select a few candidates for follow-up observation with the Whipple telescope, a 1° radius search was performed around each of the 18 locations in radio, optical, x-ray, and gamma-ray catalogues. Four promising candidates were chosen for observation during the 2001-2002 observing season. After receiving an update from new Tibet III data, one more candidate was selected for observation during the 2002-2003 season. The selections were based on the expected flux level extrapolated from the Tibet AS measurements, as well as possible correlation with interesting x-ray and gamma-ray selected objects. Features in the Tibet AS data were also considered, such as evidence of steady emission. A summary of the targets is given in Table 3.1, while the specific reasons for each selection are listed below:

- Tibet1 had a high significance and showed steady increase through Tibet-II HD data.

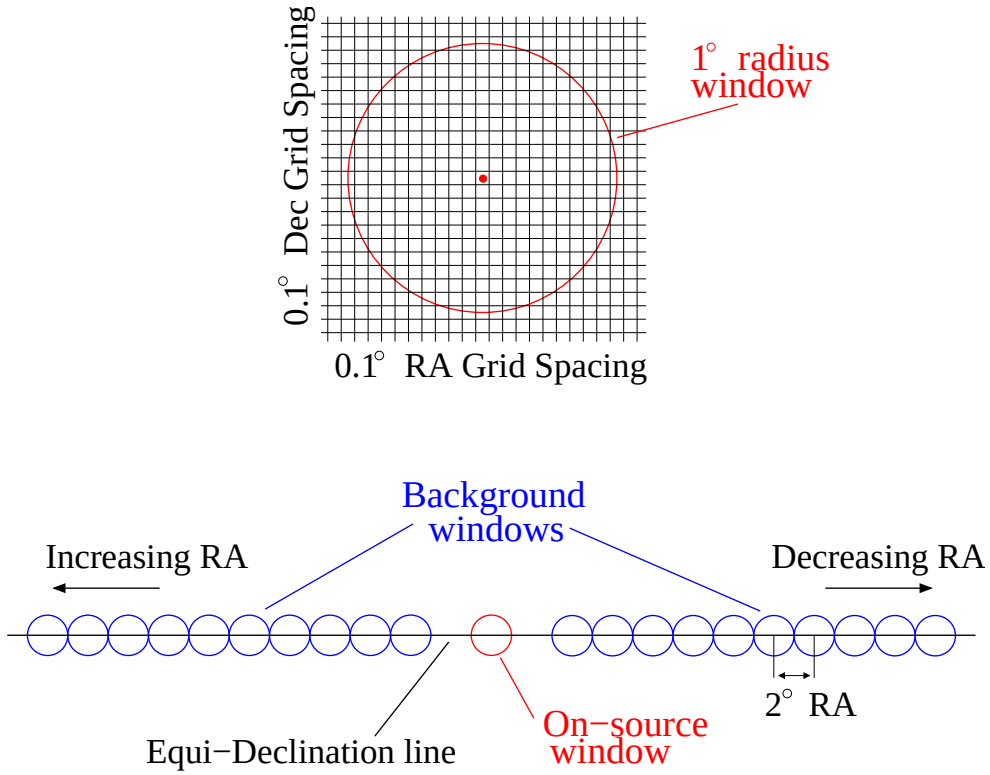

Figure 3.7. Illustration of the search method used in the Tibet sky survey. Top figure: bins inside or in contact with the 1° radius search window constitute the signal for that point. Bottom Figure: the on-source background is estimated using 20 similar background windows at the same Declination. The search increment was 0.1° in both axes, resulting in a large oversampling factor.

Table 3.1. Tibet candidates chosen for observation with the Whipple telescope

Name	Tibet Dataset	RA	Dec	Tibet Excess
*Crab	Tibet-II HD	5h 33.2m	22.2°	4.8σ
Tibet1	Tibet-II HD	3h 47.2m	34.2°	4.9σ
Tibet9	Tibet-II HD	13h 38.4m	24.2°	4.2σ
Tibet14	Tibet-II HD	20h 21.6m	37.9°	4.2σ
Tibet16	Tibet-II HD	21h 29.6m	45.3°	4.8σ
*Crab	Tibet-II HD + III	5h 34.4m	22.0°	5.4σ
Tibet0554	Tibet-II HD + III	5h 54.8m	30.1°	4.8σ

*Crab included for reference

- Tibet9 is 0.3° from a Seyfert 1 galaxy (IRAS J13349+2438).
- Tibet14 is 0.7° from an EGRET unidentified (3EG J2021+3716).
- Tibet16 had a high significance and is in the Cygnus star field.
- Tibet0554 showed steady increase through Tibet-II HD and Tibet-III and was second in significance to the Crab.

CHAPTER 4

ANALYSIS TECHNIQUES

4.1 Analysis Technique

The limited angular resolution of Tibet AS introduces uncertainty into the source coordinates of each of the candidates. Therefore, two-dimensional (2-D) analysis is required for the Whipple data. The necessary search radius is unknown, but it may be estimated by considering known sources detected by Tibet AS. In the Tibet-II HD dataset, the peak position for the Crab was offset by 0.4° from the Crab coordinates [47], and in the Tibet-III dataset the offset was 0.3° for the Crab and 0.6° for Mrk 421 [64].It is therefore reasonable to expect a true source, if it exists, to be within 1° of the given candidate coordinates.

4.1.1 Event Selection – Standard Parameters

The analysis for a source at the center of the field of view is well developed. As described in Chapter 3, a set of shape cuts (*Length*, *Width*, and *Length/Size*) is applied to select potential gamma ray images, and *Alpha* and *Distance* cuts are used to further reduce the background. This method can be modified for use in the 2-D analysis, but the effect of an off-axis source on the image parameters (particularly the *Length*) must be considered. Figures 4.1 and 4.2 show the *Length* and *Width* distributions for simulated 1 TeV gamma rays for a source at both the center and at 1° offset. The *Width* is largely unaffected by the source position, but the images tend to be longer for an offset source, as is expected. Figure 4.3 shows that lower energies are affected as well.

It is clear that using the standard *Length* cut for an off-axis source is not ideal, especially at higher energies. This is of particular concern when analyzing the Tibet candidates because of the high energy threshold of Tibet AS. To compensate

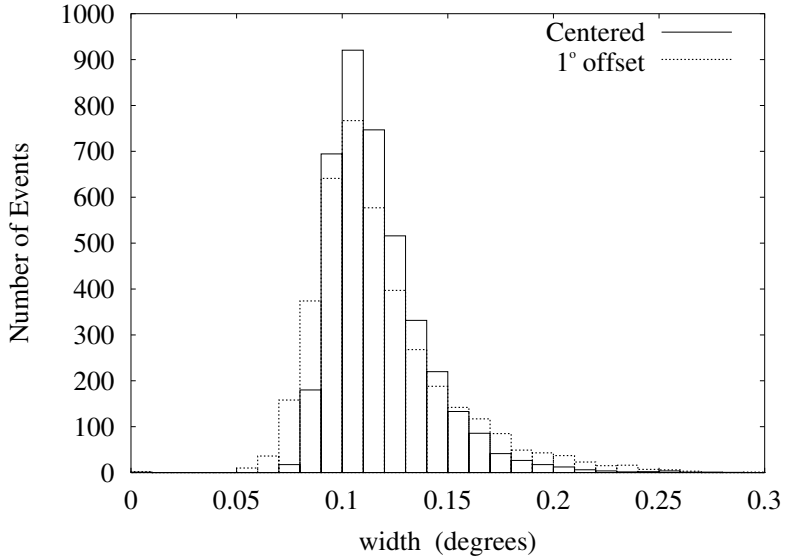

Figure 4.1. *Width* distribution for simulated 1 TeV gamma rays with a source at the center compared to a source at 1° offset. A minimum *Size* cut was applied in both cases to avoid severely truncated images.

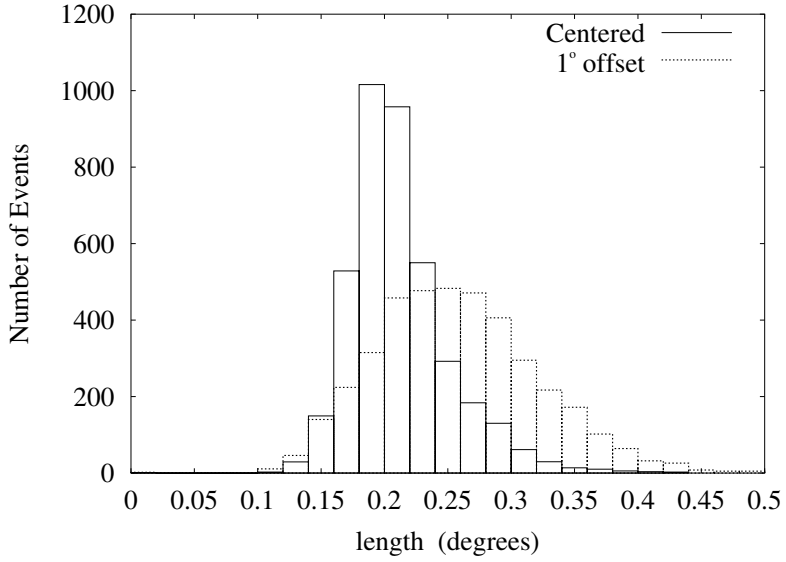

Figure 4.2. *Length* distribution for simulated 1 TeV gamma rays with a source at the center compared to a source at 1° offset. A minimum *Size* cut was applied in both cases.

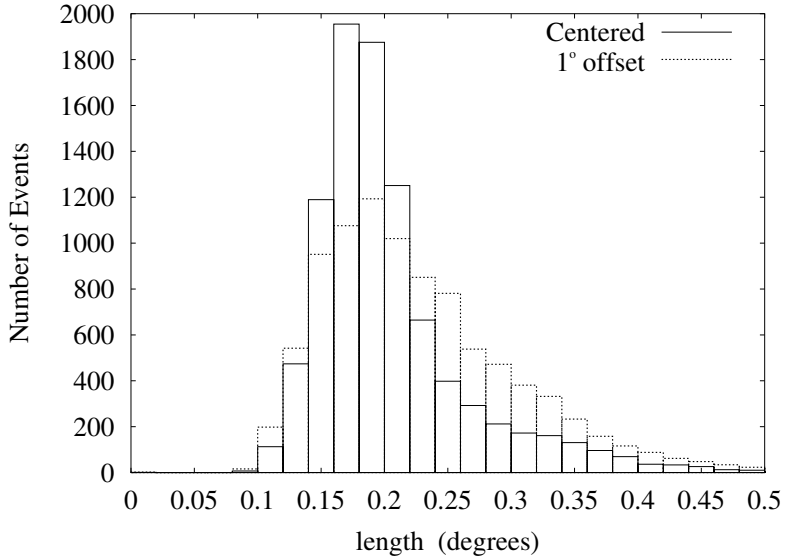

Figure 4.3. *Length* distribution for simulated 487 GeV gamma rays with a source at the center compared to a source at 1° offset. A minimum *Size* cut was applied in both cases.

for this, the length cut must be modified. Figure 4.4 shows the *Length* versus $\ln(Size)$ distributions for 1°-offset simulations at three energies. A cut of the form $Length < a_{\rm len} \ln(Size) + b_{\rm len}(O)$ is shown in the figure, where $a_{\rm len}$ is a constant and $b_{\rm len}$ is a function of the source offset O. The slope of the cutting line is $a_{\rm len} = 0.02°$, and this was found to work well for all of the offsets. The value of $b_{\rm len}(O)$ was found for simulations at 5 offsets ranging from 0° to 1.3°, and a 2nd order polynomial was fit to it. Thus, the equation for the modified length cut is

$$Length < 0.02 \ln(Size) + (0.052°(O)^2 + 0.056°(O) + 0.14°),$$

where O is the offset of the source from the camera center.

The *Width* parameter is also correlated with the size, and so the *Width* cut may be written $Width < a_{\rm wid} \ln(Size) + b_{\rm wid}$, where $a_{\rm wid}$ and $b_{\rm wid}$ are both constants (the same at every offset). Figure 4.5 shows the *Width* versus $\ln(Size)$ distributions for simulations at 1° offset. As as seen in the figure, $a_{wid} = 0.02°$ and $b_{wid} = 0°$, and so the *Width* cut is given by $Width < 0.02 \ln(Size)$. Note that a stricter or looser cut may be applied by decreasing or increasing the value of $b_{\rm wid}$.

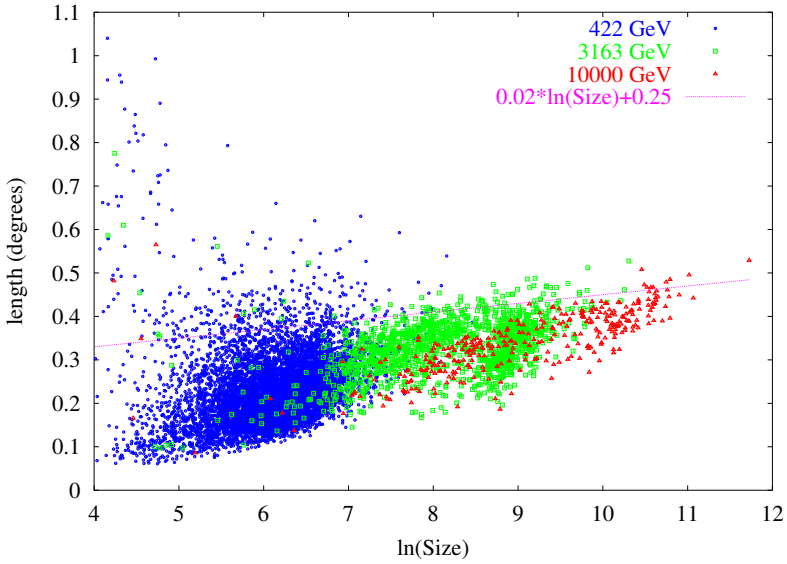

Figure 4.4. *Length* versus ln(*Size*) distributions for simulated gamma rays at 1° offset and 20° zenith angle. A cut of *Alpha* < 15° has been imposed to avoid images distorted by noise. The line represents the *Length* cut, which at this offset is $Length < 0.02\ln(Size) + 0.248$.

Figure 4.6 shows $Width/\ln(Size)$ for simulated gamma rays versus real background data. Here, the simulated gamma rays follow a Crab-like spectrum (dN/dE $\sim E^{-2.5}$). The effectiveness of the *Width* cut is clear. Figure 4.7 shows the $(Length - 0.25)/\ln(Size)$ distributions for the same datasets, but after the *Width* cut was applied. The separation between the distributions is small, but the *Length* cut is still useful.

The cuts presented here, as well as those described later, are quite broad. Stricter values for the cuts may improve the signal to noise ratio, but the distributions will change slightly depending on the noise, how many pixels are turned off, the zenith angle, and so on. The cuts used here are purposely broad enough to allow for these minor variations, as well as unseen imperfections in the simulations, without significantly affecting the final results of the analysis.

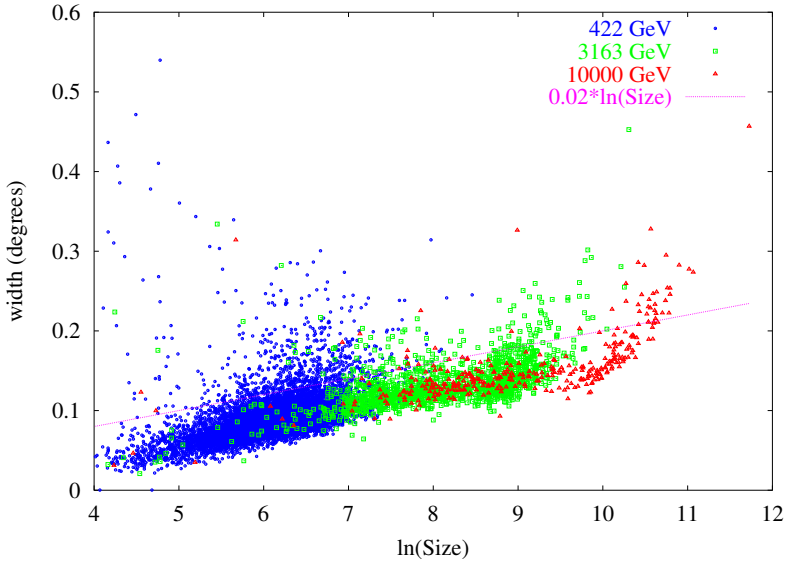

Figure 4.5. *Width* versus ln(*Size*) distributions for simulated gamma rays at 1° offset and 20° zenith angle. A cut of $Alpha < 15°$ has been imposed to avoid images distorted by noise. The line represents the *Width* cut, which is given by $Width < 0.02° \ln(Size)$ for all offsets.

4.1.2 Event Selection – χ^2

As was already noted, modifying the *Length* cut was necessary for selecting higher energy gamma rays from an off-axis source. Unfortunately, the modified cut also lets more background events through. Therefore, it is worthwhile to investigate methods of further differentiation between gamma rays and the background. One method is to estimate how much each image looks like a gamma ray by using a χ^2 calculation. In this case, χ^2 is defined as

$$\chi^2 = \sum_i \frac{(f(P) - q_i)^2}{\sigma_i^2}$$

where $f(P)$ is the function describing a parameterized gamma ray image in ADCs, and q_i is the number of ADCs from pixel$_i$. The uncertainty in the signal from pixel$_i$ is σ_i, and the function parameters are denoted by P. It is critical, however, to come up with a suitable parameterized description of a typical gamma ray image.

Figure 4.8 shows the average of many Cherenkov images for simulated gamma rays, with 487 GeV gamma rays on the left, and 1000 GeV gamma rays on the

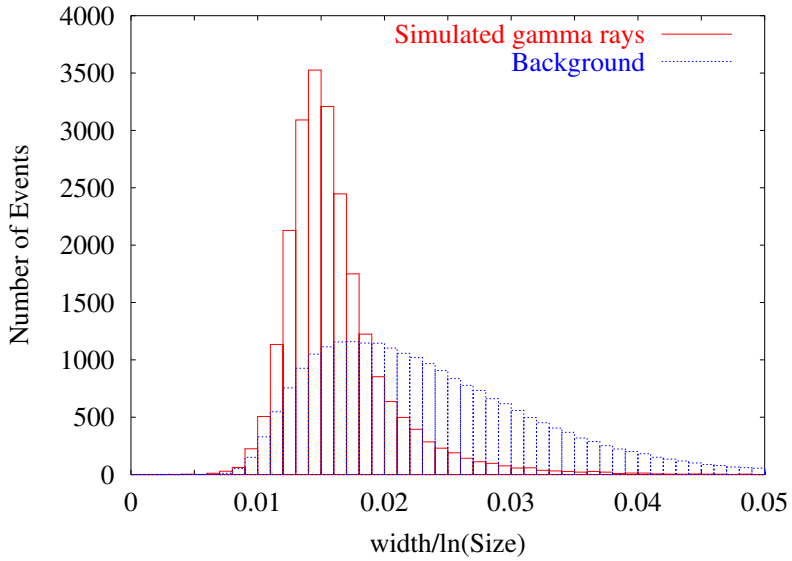

Figure 4.6. $Width/\ln(Size)$ distribution for simulated gamma rays at 1° offset versus background. The *Width* cut corresponds to $Width/\ln(Size) < 0.02$. The simulated gamma rays follow a -2.5 power-law spectrum. A minumum *Size* cut of 400 ADC was applied to each dataset, and a cut of $Alpha < 20°$ was applied to the simulations to avoid events distorted by camera noise. The histograms have been scaled to have equal area.

right. To create the average image, each simulated gamma-ray image was rotated about its center of charge so that its source point lies on the positive x-axis.

Each average image is elliptical, and both are asymmetric toward the right, i.e. toward the direction of the source point. This asymmetry makes the average image difficult to describe using a single elliptical Gaussian, but it is well described using two independent elliptical Gaussians. One Gaussian ellipse (the base) is taken to encompass the entire image, while the second is positioned to fit the asymmetry. The second ellipse is required to lie along and parallel to the major axis of the base. Thus, the function $f(P)$ is defined as

$$f(P) = \frac{A}{(1+\frac{1}{2q}(\frac{(x-X_0)^2}{L^2}+\frac{(y-Y_0)^2}{W^2}))^q} + ae^{\frac{1}{2}\left(\frac{(x-x_0)^2}{l^2}+\frac{(y-y_0)^2}{w^2}\right)}$$

when, for simplicity, an image is oriented with its major axis parallel to x-axis. The first half of the equation was originally used to allow the optimization of q, but for

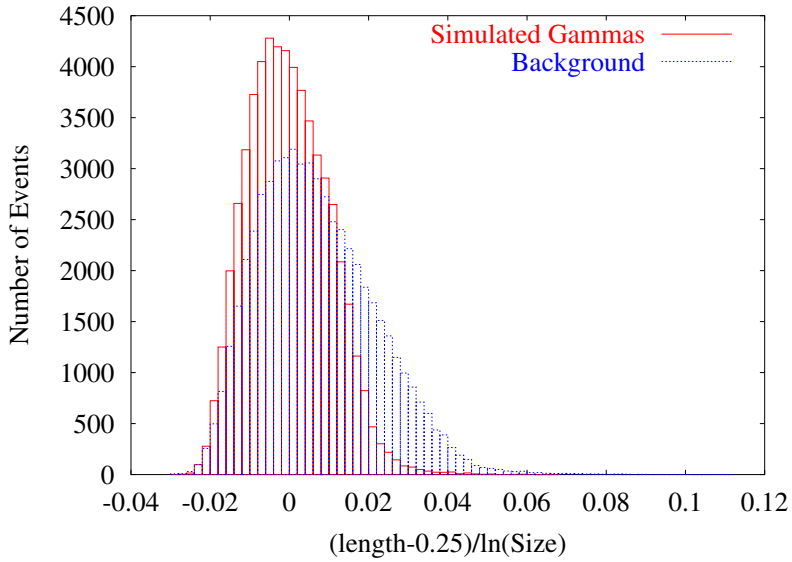

Figure 4.7. $(Length - 0.25)/\ln(Size)$ distribution for simulated gamma rays at 1° offset versus background, after the *Width* cut was applied. The *Length* cut corresponds to $(Length - 0.25)/\ln(Size) < 0.02$. The simulated gamma rays follow a -2.5 power-law spectrum. A minumum *Size* cut of 400 ADC was applied to each dataset, and a cut of $Alpha < 20°$ was applied to avoid events distorted by camera noise. The histograms have been scaled to have equal area.

all the analysis that follows, $q = 6$, and the function is very nearly Gaussian. The function parameters are the amplitude A, centroid (X_0, Y_0), length L, width W, and orientation angle ϕ of the base ellipse, along with the amplitude a, centroid (x_0, y_0), length l, and width w of the second ellipse.

The parameters are found through an iterative process. The initial parameters are just the centroid, *Length*, *Width*, and orientation of the image, calculated using the moments of the image. The amplitude is calculated analytically, using $\partial\chi^2/\partial A = 0$. Then, the resulting function $f(P)$ is subtracted from the image to look for the residual asymmetry. The centroid, length, and width of the residual asymmetry is calculated, and the extra amplitude is found analytically. The final step of the iteration is to subtract the extra ellipse function from the original image and recalculate the length, width, and centroid of the base ellipse. The parameters were found to converge after a few iterations, but 15 iterations were performed in

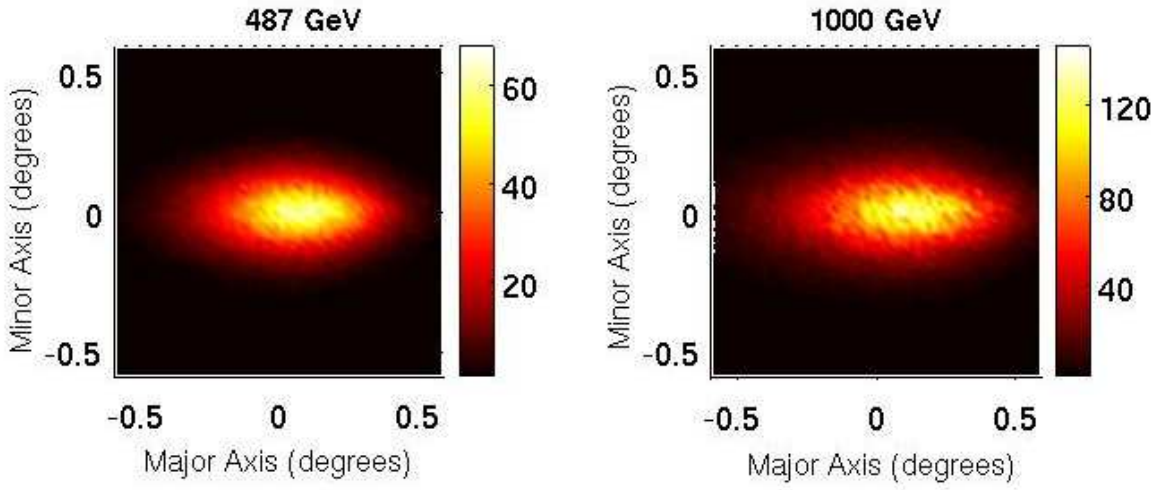

Figure 4.8. Average Cherenkov image derived from many simulated gamma rays. Each simulated image was rotated about the center of charge so that its source point is on the positive x-axis. The individual images were then co-added to obtain the average.

this analysis.

Once the parameters are found, they are used to calculate the reduced χ^2:

$$\chi_0^2 = \frac{1}{N} \sum_i \frac{(f_{\rm pe}(P) - \frac{g_i S_i}{\mu})^2}{\frac{g_i S_i}{\mu} + \frac{g_i^2 NSB_i^2}{\mu^2}}.$$

In this form, each component is in terms of photoelectrons. Here, index i is the pixel number (ranging from 1 to N), g_i is the flat-fielding factor, S_i is the raw number of ADCs, and μ is the photoelectron to ADC conversion factor ($\mu = 3$ in this analysis). Rewriting,

$$\chi_0^2 = \frac{1}{N\mu} \sum_i \frac{(f_{\rm adc}(P) - q_i)^2}{q_i + \frac{g_i^2 NSB_i^2}{\mu}}.$$

where $q_i = g_i S_i$ is the flat-fielded signal in pixel$_i$. Thus, χ_0^2 is found by summing this equation over the pixels in the image and dividing the by the number of pixels.

It was found that χ_0^2 provides good separation between simulated gamma rays and real background data. However, even better differentiation is achieved by dividing χ_0^2 by the peak value of the fitting function ($f_{\rm max}$). This is because gamma

ray images tend to have a higher charge density in the center than corresponding background images in the same *Size* range. Unfortunately, the simulated $\chi_0^2/f_{\max}$ distributions don't line up for different energies. This may be approximately fixed by multiplying $\chi_0^2/f_{\max}$ by $(\ln(Size))^2$, and the product is referred to hereafter as the χ^2 parameter. Figure 4.9 shows the simulated distribution for three energies.

A comparison between simulated gamma rays and the background for the χ^2 parameter is made in Figures 4.10 and 4.11. In both figures, the *Length* and *Width* cuts have already been applied. In each case, there is good separation between the simulations and the background. As is seen in the figures, there is still some disagreement between the different energies, in spite of the $(\ln(Size))^2$ factor. Because of the high energy threshold of Tibet AS, preference is here given to the higher energies. A cut of χ^2 Parameter < 1 cuts out a good amount of the background, and yet is loose enough at higher energies to allow for possible differences between the simulations and real gamma rays.

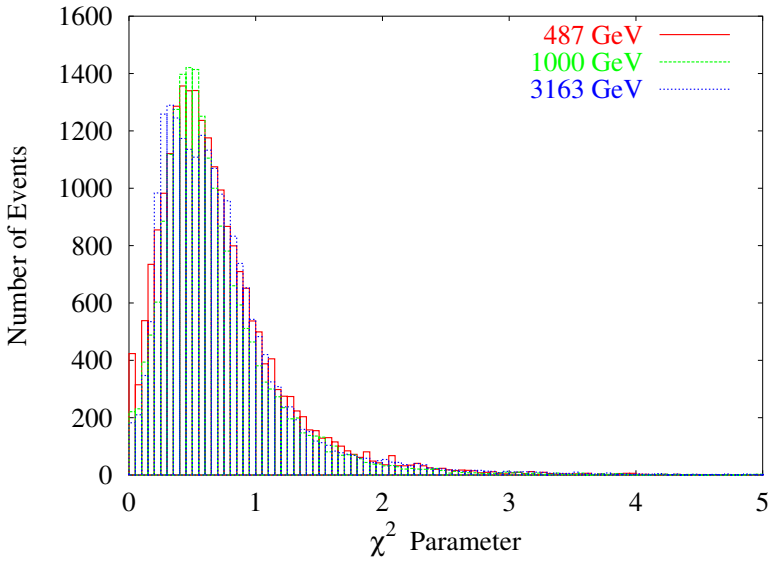

Figure 4.9. χ^2 parameter distributions for simulated gamma rays at 1° offset and 20° zenith angle. The χ^2 parameter is defined as $\chi^2(\ln Size)^2/f_{\max}$. The *Length* and *Width* cuts have been applied.

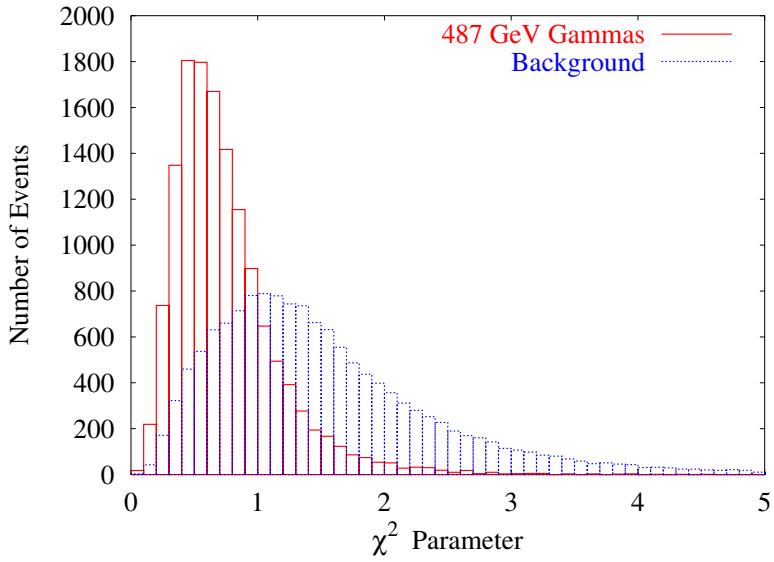

Figure 4.10. χ^2 parameter distribution for simulated gamma rays at 1° offset at a 20° zenith angle and for real background data. For both the gamma rays and the background, *Sizes* between 400 ADC and 1000 ADC were used, and the *Length* and *Width* cuts have already been applied. The histogram amplitudes have been scaled to have equal area.

4.1.2.1 Pointing Determination

It was noted in the discussion of the average gamma-ray images that there is a concentration of charge along the positive x-axis. Because the source point also lies along positive x, the asymmetry provides a clue as to which direction the image is pointed. Because a secondary Gaussian ellipse was used to match the asymmetry, its position relative to the image centroid provides the pointing. Figure 4.12 shows an *Alpha* plot for simulated gamma rays where *Alpha* is determined based on the position of the secondary ellipse.

The plot shows that the method works quite well for small events, and very well for large events. The method loses its effectiveness for events that are severely truncated. Based on this, a compromise is made in this analysis such that the pointing is used unless the event is more than 0.8° from the center and $Alpha < 30°$.

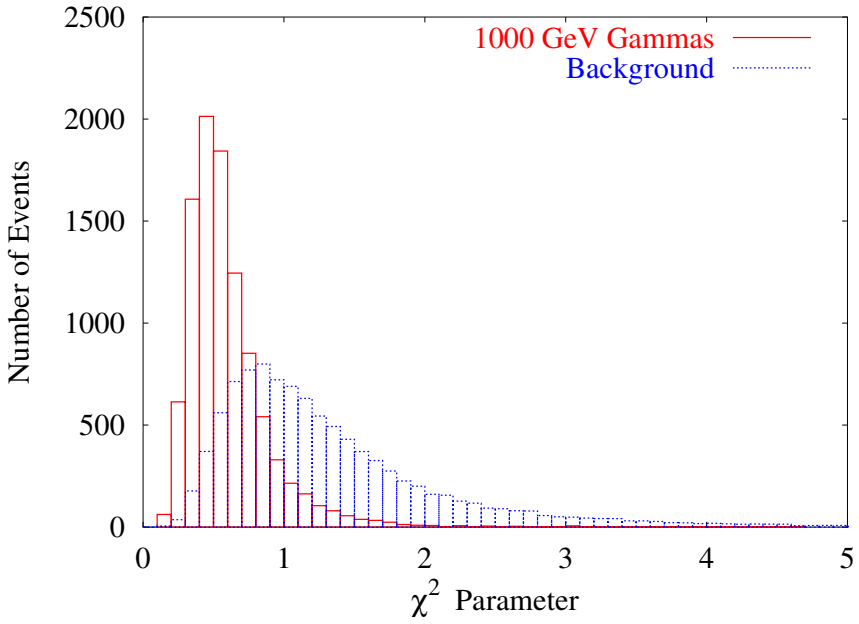

Figure 4.11. χ^2 parameter distribution for simulated gamma rays at 1° offset at a 20° zenith angle and for real background data. For both the gamma rays and the background, *Sizes* above 1000 ADC were used, and the *Length* and *Width* cuts have already been applied. The histogram amplitudes have been scaled to have equal area.

4.1.3 2-D Map

Once the gamma-like events have been selected, a 2-D map may be created. This is done by creating a grid of points with 0.1° spacing, as is shown in Figure 4.13. At each grid point, *Alpha* and *Distance* are calculated for each event. Events satisfying the *Alpha* and *Distance* cuts at a particular grid point are included in the signal for that grid point. The background at the same grid point is estimated in the same way, except the OFF-source data are used. (If no OFF-source data are available, an average of many OFF runs is used instead. This will be discussed in Chapter 5.) The *Alpha* cut is given by $Alpha < 10°$. The *Distance* cut is discussed in the next section.

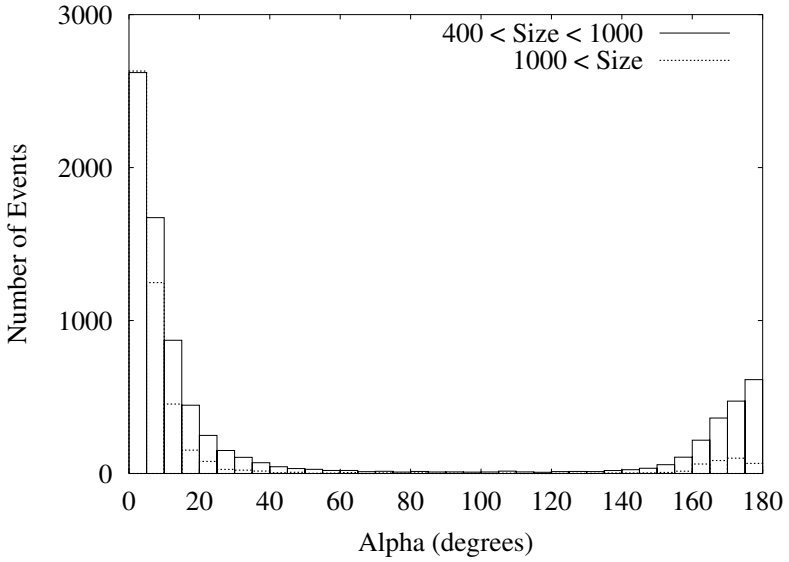

Figure 4.12. *Alpha* plot for simulated gamma rays at 1° offset. The simulated gamma rays follow a -2.5 power-law spectum, and the plots were produced by applying the *Size* cuts as shown.

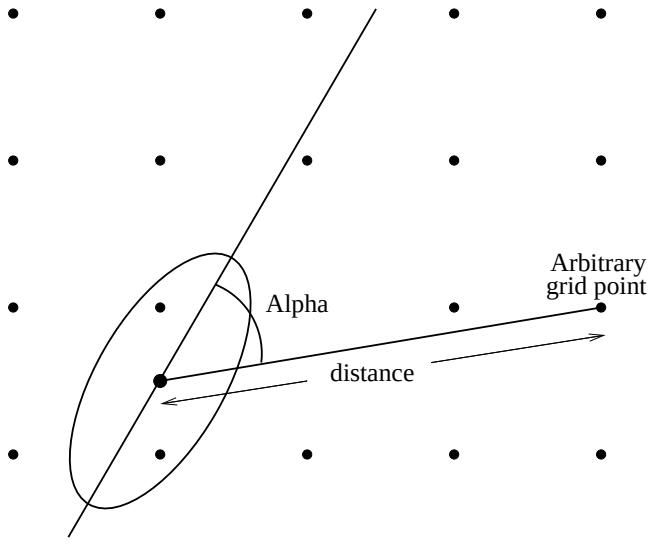

Figure 4.13. Grid for 2-D map. Grid spacing is 0.1°.

4.1.4 *Distance* Cut

As is expected, the *Distance* distribution for an off-axis source is different than for an on-axis source. Figure 4.14 shows that the *Distance* distribution extends over a broad range. Rather than simply using broader cuts, it is worthwhile to consider the *disp* method described in [65]. In it, the estimated distance, or *disp*, is calculated using $disp = \xi(1 - Width/Length)$, where the parameter ξ is determined using either simulations or data from a known source. Unfortunately, as is seen in Figure 4.15, the distribution of the ξ parameter is also broad for an off-axis source. Therefore, in this analysis, the *Distance* cut is actually a cut made on the ξ parameter, where ξ is calculated using

$$\xi = \frac{Distance}{1 - Width/Length}.$$

Using this cut constrains short, wide images to be close to the grid point and long, narrow images to be further away. This reduces the possibility of an event overlapping its supposed source point, which is a common occurence when using a simple *Distance* cut.

Figure 4.16 shows the ξ distribution at three different energies. The cuts are represented by the bounding lines, which are functions of $\ln(Max1 + Max2)$. More signal could be included by raising the upper line, but the increase in the background is too great. Also, Figure 4.16 is for simulations at 1° offset. As the offset decreases, the ξ distribution spreads vertically because of image truncation. To compensate for this, the intercept of the upper line is made a function of the offset O and ranges from 1.15 to 2.0. The slope, however, remains the same. Thus, the *Distance* cut is given by

$$\frac{Distance}{1 - Width/Length} > 0.12\ln(Max1 + Max2) + 0.15,$$

$$\frac{Distance}{1 - Width/Length} < 0.12\ln(Max1 + Max2) + (0.26(O)^2 - 1.11(O) + 2.0).$$

4.1.5 Oversampling

The *Alpha* and *Distance* cuts as presented allow oversampling to occur. This means a single event may contribute to the signal of more than one grid point (see

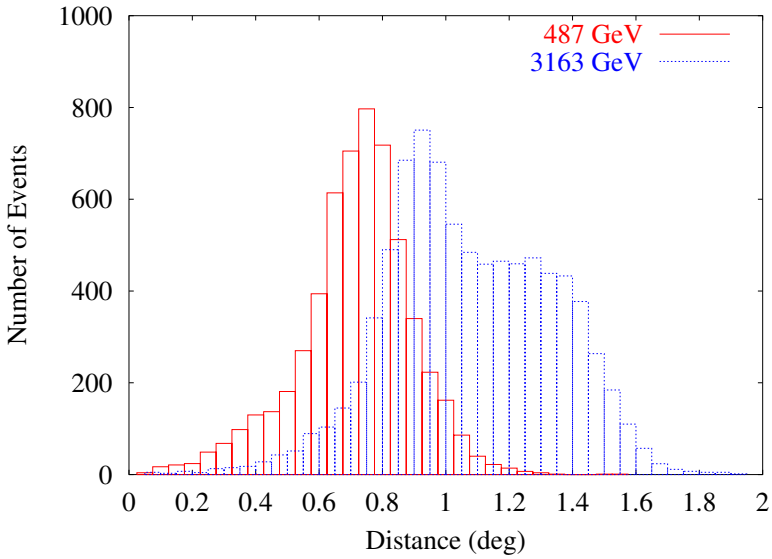

Figure 4.14. *Distance* histogram for simulated gamma rays at 1° offset and 20° zenith angle. Here, *Distance* is the angular distance between the source point and the image centroid.

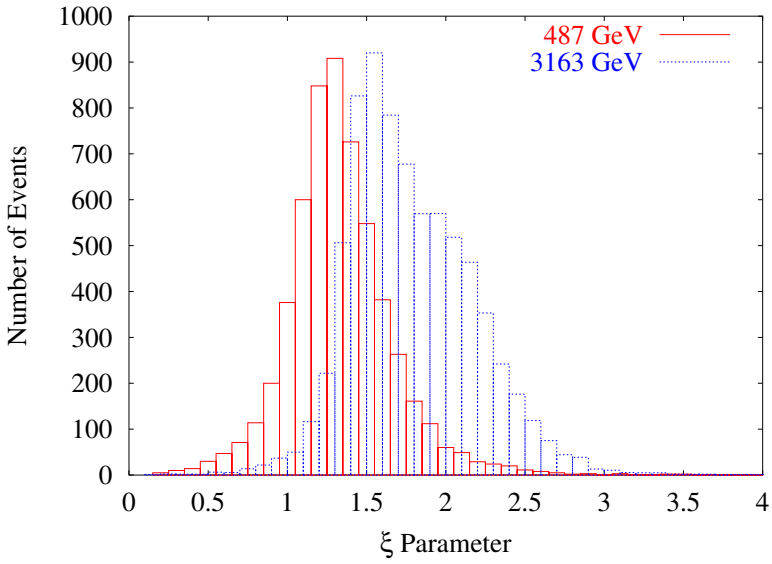

Figure 4.15. Distribution of ξ for simulated gamma rays at 1° offset and 20° zenith angle, where ξ is calculated using $\xi = Distance/(1 - Width/Length)$.

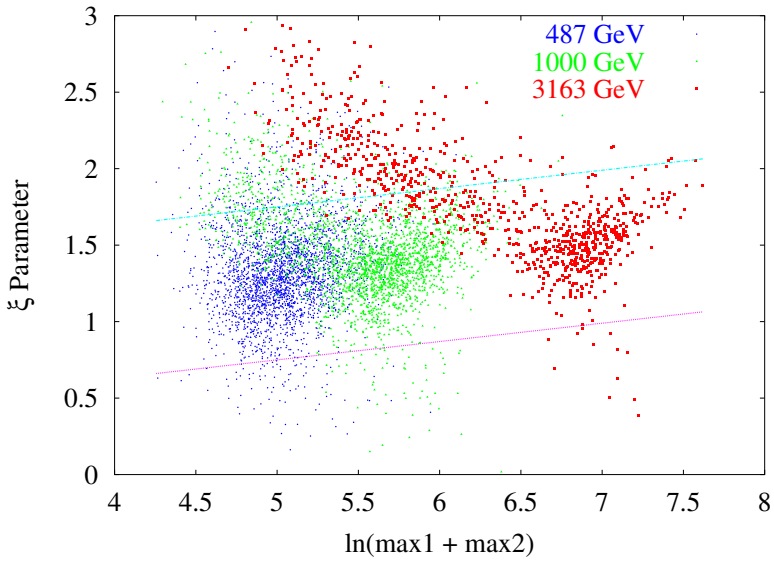

Figure 4.16. ξ vs $\ln(Max1 + Max2)$ distribution for simulated gamma rays at 1° offset and 20° zenith angle. The lower line is given by the equation $0.12\ln(Max1 + Max2) + 0.15$ and is the same for all offsets. The equation for the upper line is $0.12\ln(Max1 + Max2) + 1.15$, but the intercept varies from 1.15 to 2.0, depending on the offset.

Figure 4.13). In this analysis, each event is used an average of 14 times. The effects of oversampling have been investigated through simulations.

In the simulation, two square grids (one ON and one OFF), each with one million points (1000 x 1000), were set up. Each grid was populated, point by point, according to Gaussian statistics with a large mean and a sigma of the square root of the mean. Then, the Li and Ma [60] significance was calculated for two cases: one with no oversampling, and one with massive oversampling. In the case of no oversampling, a single ON grid point was compared to the corresponding OFF grid point, and this was repeated for every grid point (one million trials). In the case of massive oversampling, the signal at a given point was the sum in a 21x21 square bin centered on that point. The OFF signal at the corresponding point in the OFF grid was found the same way. This was repeated for each point in the grid, so that the significance was again calculated one million times, but in this case each point was used 441 times.

Figure 4.17 shows the significance histogram, with log scale in y, for both cases. The histograms are nearly identical. Each is well described by a Gaussian with a mean of zero and a standard deviation of one. Moreover, the tails are similar. This suggests that oversampling does not affect the significance of a measurement.

Figure 4.18 shows, for each case, the distribution of points with significance greater than 4σ. The nonoversampled points are scattered evenly across the grid, while the oversampled points are found in clusters. Thus, oversampling makes neighboring points correlated, so that the signal in a point depends on the signal in its neighbor. It is important to note that although there are only four clusters in the oversampled case, the total number of points above 4σ is on average the same as in the nonoversampled case.

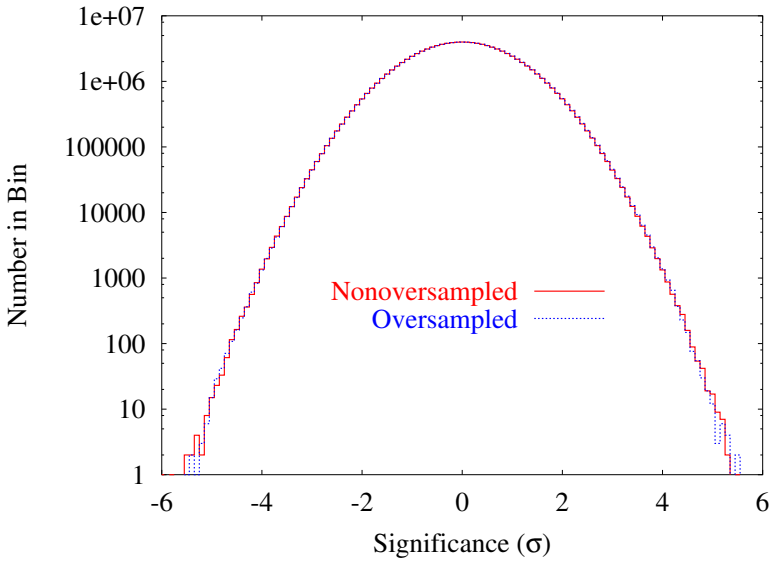

Figure 4.17. Oversampled and nonoversampled distributions of significance for a simulated ON grid compared to a simulated OFF grid, each with 10^6 points. Note that a log scale is used for the y axis. Each grid was randomly populated from a Gaussian distribution with a mean of 10^6 and a sigma of 1000. In the oversampled case, a 21x21 bin was used. The simulation was repeated 100 times to improve statistics.

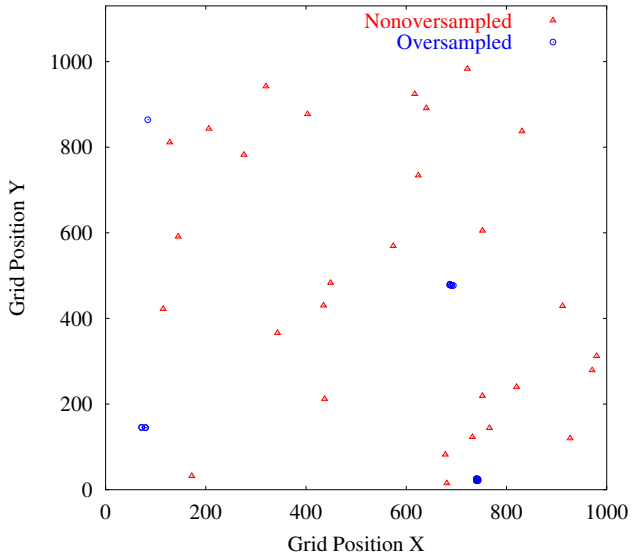

Figure 4.18. Distribution of points with significances greater than 4σ for the grid described in 4.17. The results of a single simulation for each case are shown. The nonoversampled case had 29 points above 4σ. There were 27 points for the oversampled case, but these are clustered in 4 groups. On average, both cases produced about 31 points above 4σ, consistent with a Gaussian statistics for 10^6 trials.

4.1.6 Energy Estimation for Off-Axis Sources

As has already been discussed, Tibet AS has an energy threshold of 3 TeV, while the threshold for Whipple is around 300 GeV. This difference makes it worthwhile to perform energy analysis with the Whipple Telescope, since a source with a non Crab-like spectrum (a monochromatic line source, for example) may otherwise avoid detection. Energy estimators already exist for a source at the center of the field of view, but the techniques, which include a *Distance* dependence, are not exactly suitable for a 2-D analysis. The goal of this analysis is to develop a simple technique that is applicable across the field of view of the Whipple telescope. The method need not be precise enough for a rigorous spectral analysis, but it needs to be reasonably accurate, especially around 3 TeV.

Simulations show that events of a given energy fall into two populations, as is illustrated in Figure 4.19. Events in the main part of the light pool (impact parameter $<$ 135 m) are clearly distinguishable from events in the exponential

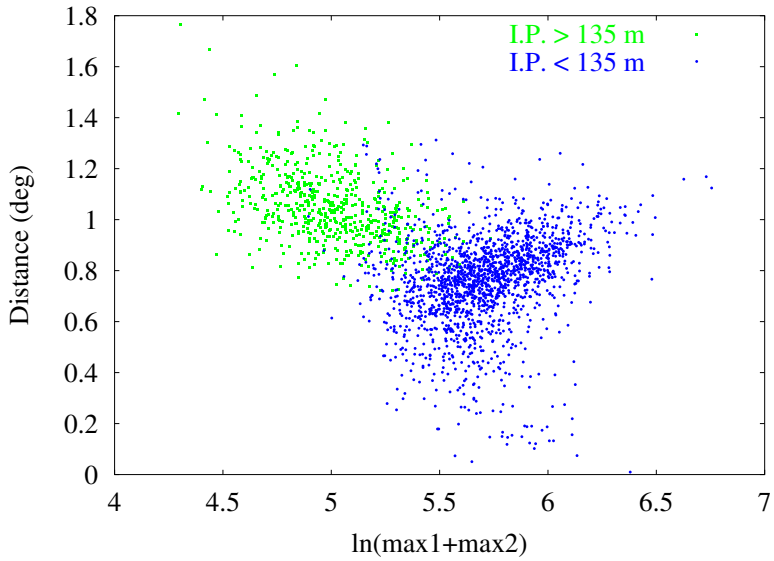

Figure 4.19. *Distance* vs $\ln(Max1 + Max2)$ distribution for simulated 1 TeV gamma rays at 20° zenith angle and 1° offset. The two distributions are separated by whether the impact parameter is greather than or less than 135 meters.

fall-off region (impact parameter > 135 m), and this analysis attempts to treat them separately. Figure 4.20 shows the same distribution at three different energies at 1° offset. The two populations may be approximately separated by the line $d = 0.075 \ln(Max1 + Max2) + 0.5$ at 1° offset, but the slope becomes more gradual as the source offset decreases. For a source at the center of the camera, the approximate separator is constant, $d = 0.88$.

For events falling above the line, the energy is best characterized as a function of *Distance* and $\ln(Max1 + Max2)$. Because of the *Distance* dependence, these events are problematic for 2-D analysis and are therefore excluded from the energy analysis. For events below the dividing line, the energy is well characterized as a function of $\ln(Max1 + Max2)$. Figure 4.21 shows the average value of $\ln(Max1 + Max2)$ versus $\ln(E)$, where E is the energy, for each simulated energy at three different zenith angles. The line in the figure was fit to the 10° data. It was constrained to have a slope of 1 because the relationship between the number of shower particles and the energy of the incident gamma ray is nearly linear. Thus, the energy estimator

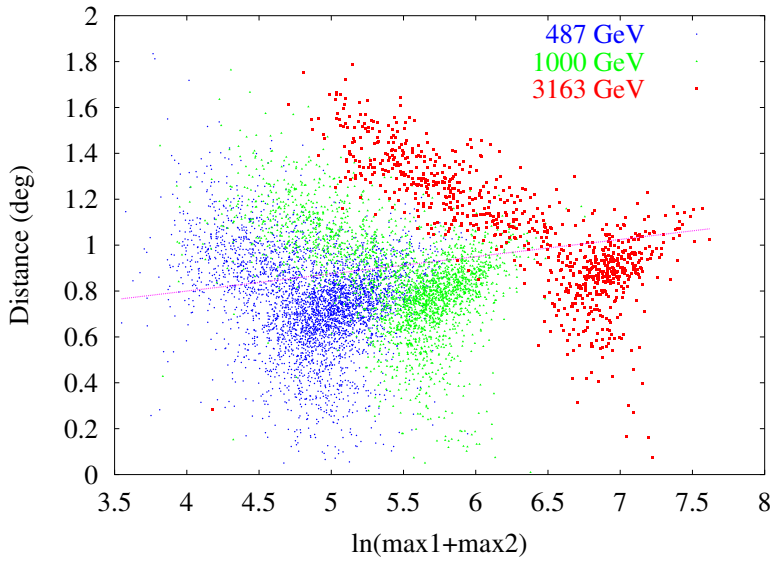

Figure 4.20. *Distance* vs $\ln(Max1 + Max2)$ distribution for simulated gamma rays at 20° zenith angle and 1° offset. The line $d = 0.075\ln(Max1 + Max2) + 0.5$ approximately separates events in the main light pool from events in the exponential drop-off region.

has the form $E_{\rm est} = \ln(Max1 + Max2) + b$. The simulations deviate from the line at the high end because of pixel saturation, while the deviation at the low end is due to cleaning effects.

As is seen in Figure 4.21, the average value of $\ln(Max1 + Max2)$ shifts to the left as the zenith angle increases. This is because the path length from the shower to the telescope increases, which reduces the photon density in two ways. First, it causes greater attenuation of the Cherenkov light, and second, it allows the light pool to spread laterally. To account for this, a zenith angle correction may be incorporated into the energy estimator, so that $E_{est} = \ln(Max1 + Max2) + b(Z)$, where b is a function of the zenith angle Z. Figure 4.22 shows the fitted value of b versus $\cos(Z)$ for simulations at 10°, 20°, 35°, and 46°. The relationship is nearly linear for $\cos(Z)$ near 1, but a quadratic provides a better fit. Thus, the complete equation for energy estimation is

$$E_{est} = \ln(Max1 + Max2) + (2.97\cos^2(Z) - 7.95\cos(Z) + 6.11).$$

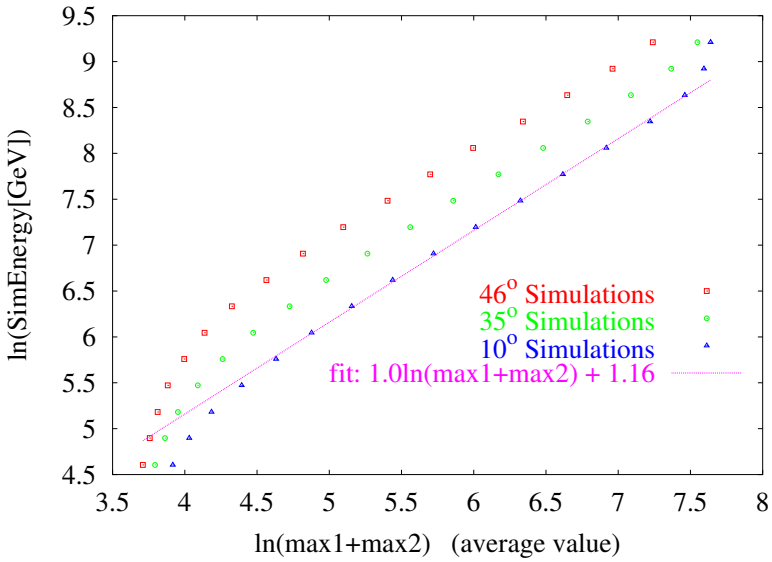

Figure 4.21. Average values of $\ln(Max1 + Max2)$ for simulated gamma rays at 0° offset after shape cuts have been applied. Only those events with $Distance < 0.88$ are included in the average.

Figure 4.23 shows the results of the energy estimator applied to the simulations. Each point shows the average value of the estimated energy, and four different zenith angles were included, with an equal number of events taken at each zenith angle. For the simulations at 422 GeV and above, the average standard deviation in ln space was 0.27, corresponding to an energy resolution of 31%. The estimator begins to fail below 400 GeV and above 7 TeV, but it is reasonably accurate near the 3 TeV threshold of the Tibet Air Shower Array. Since the estimator depends only on $Max1 + Max2$ and not the *Distance*, it is suitable for the 2-D analysis.

4.1.6.1 Test Energy Estimator: Crab On-Axis Data

While it is instructive to test the energy estimation with the simulations, it is also useful to test it on the Crab Nebula, since the Crab is a steady source and has a well-known spectrum. To calculate the Crab spectrum, the following equation was used: $S_i - B_i = R_{ij}T_j$, where i is the energy bin, S_i is the source count, and B_i is the background. R_{ij}, the detector response matrix, and T_j, the true spectrum, are summed over j for each i. R_{ij} accounts for a gamma ray of

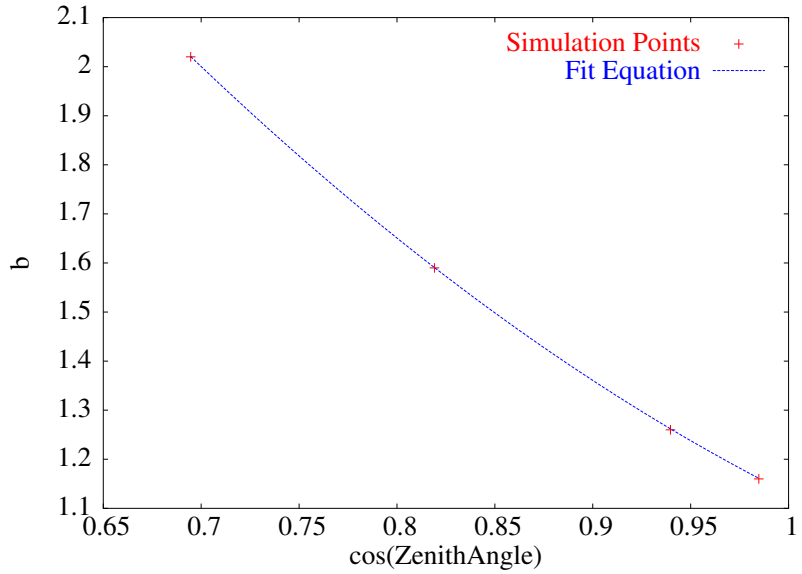

Figure 4.22. Fitted values for b versus $\cos(ZenithAngle)$, where b comes from the equation $E_{est} = \ln(Max1 + Max2) + b(Z)$. Each zenith angle dataset provided a different b value, and the simulations were done at zenith angles of 10°, 20°, 35°, and 46° and at 0° offset. The fitting equation is $b = 2.97\cos^2(Z) - 7.95\cos(Z) + 6.11$, where Z is the zenith angle.

energy j being misconstructed to an energy i ($i \neq j$). T_j is assumed to have the form $T_j = A(E/E_0)^{\gamma}$. A, the amplitude, and γ, the spectral index, are found by minimizing χ^2, where

$$\chi^2 = \sum_i \frac{(R_{ij}T_j - (S_i - B_i))^2}{S_i + B_i}.$$

S_i and B_i are found by applying the cuts and the energy estimation to the ON-source and OFF-source data, and the matrix R_{ij} is calculated by applying the same cuts and energy estimation to simulationed data.

The cuts used here are broader than the normal cuts to allow for possible differences between the simulations and the real data. Since the *Length* and *Width* cuts are defined by a line in *Length*:ln(*Size*) and *Width*:ln(*Size*) space, these cuts are broadened by increasing the offset of the line by 0.05° in each case (the amount was somewhat arbitrary). The *Alpha* and χ^2 cuts were also relaxed, and the upper *Distance* cut was set at 0.88° so that most of the events come from the main light

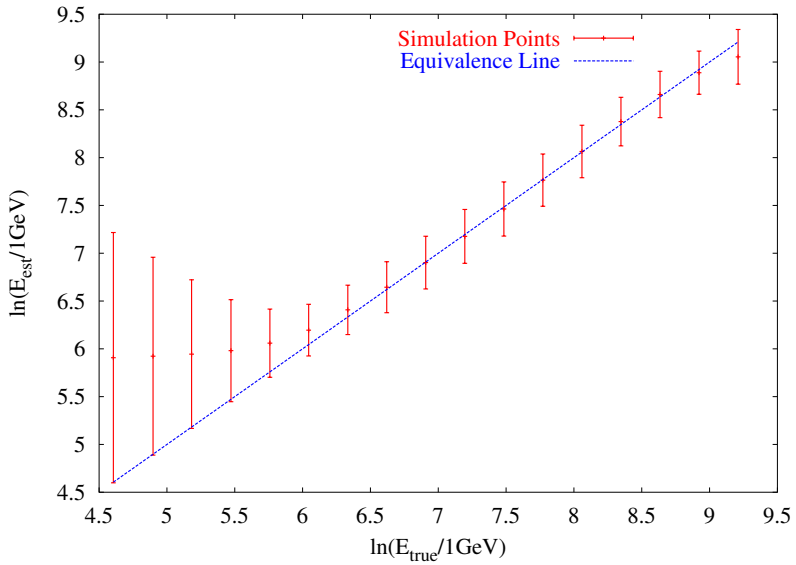

Figure 4.23. Average value of the calculated energy versus the actual energy for simulations at 0° offset and after cuts have been applied. Events at four different zenith angles (10°, 20°, 35°, and 46°) were included in each average, with an equal number of events (before cuts) at each zenith angle. The plotted error bars show the standard deviation (in ln space) from the true value at each point.

pool. Finally, the $Length/Size$ is retained to preserve the muon rejection. Thus, the cuts used are

- $Width < 0.02 \ln(Size) + 0.05$
- $Length < 0.02 \ln(Size) + 0.19$
- $Alpha < 15°$
- $(\chi^2 parameter)(\ln(Size))^2 < 1.2$
- $0.4° < Distance < 0.88°$
- $Length/Size < 0.0004$.

For simulation events falling in the range $0.4° < Distance < 0.88°$ and $Alpha < 15°$, where the $Alpha$ cut is used to limit those events that are distorted by noise, greater than 90% pass these shape cuts.

The method is here applied to 89 ON/OFF pairs taken in 'A' weather during the 2001-2002 and 2002-2003 observing seasons, with the Crab at the center of the field of view. The midrun zenith angle for this data ranges from 10° to 35° and has an average of 18°. Simulations were run with equal spacing in $\cos(ZenithAngle)$ space, with bin midpoints lying at 20°, 35°, and so on. Because the response of Whipple varies with the zenith angle, it is necessary to sort the Crab data into these bins. Approximately 85% of the data lies in the 20° bin, and the rest falls into the 35° bin. Since the statistics for the 35° bin are limited, and since nearly all of the data for the Tibet targets lies in the 20° bin, only the Crab data in the 20° bin will be used here.

After the cuts, there are 26838 events ON-source, and 21383 events remain OFF-source. These events are then binned according to the estimated energy, and the parameters A and γ in $T_j = A(E/E_0)^\gamma$ are found by minimizing χ^2. Thus, the differential flux is calculated to be

$$\frac{dN}{dE} = (3.31 \pm 0.14 \pm 0.44) \times 10^{-7} \left(\frac{E}{TeV}\right)^{-2.53\pm0.06\pm0.37} TeV^{-1}m^{-2}s^{-1}.$$

The first uncertainty listed in each case is statistical and is determined by the χ^2 fit. The second uncertainties are systematic and are estimated by varying the cuts and by using the $ZenithAngle = 10°$ simulations to find the response matrix instead of the 20° simulations (much of the data has $ZenithAngle < 15°$). The system gain was also varied by ±20%, as is justified in [66]. Figure 4.24 shows a graphical representation of the data, along with the fit provided by the χ^2 analysis. Here, the points in the figure were determined by estimating the collection area at each energy, including spillover from other energies with an assumed spectral index of $\gamma = -2.5$. The fitted spectrum is similar to a more thorough analysis performed by Hillas, et al., which found the differential flux to be

$$J = (3.2 \pm 0.17 \pm 0.6) \times 10^{-7} \left(\frac{E}{TeV}\right)^{-2.49\pm0.06\pm0.04} m^{-2}s^{-1}TeV{-}1,$$

where, as above, the statistical uncertainties are listed first, followed by the systematic uncertainties [22].

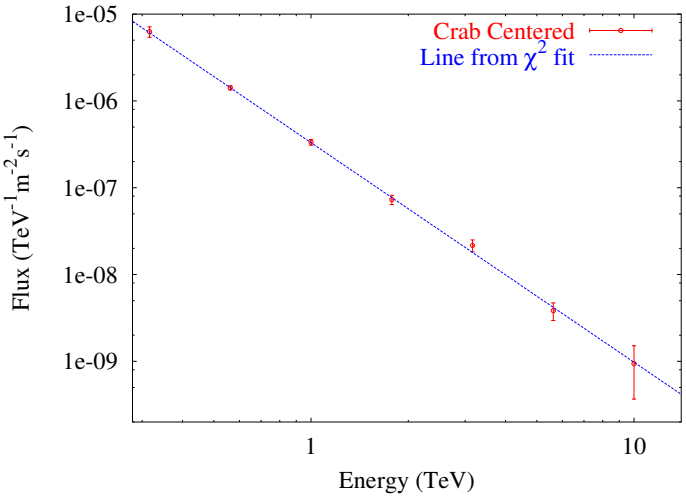

Figure 4.24. Graphical representation of the Crab spectrum as derived by the χ^2 minimization. The points in the graph are given by, for each energy, $(ON - OFF)/(A \times W \times T)$, where A is the collection area in m^2, W is the bin width in TeV, and T is the observation time in seconds. The collection area was calculated for the 20° simulations with an assumed spectral index of -2.5. The fit comes from the χ^2 minimization as described in the text. The data shown here fall into the 20° zenith angle bin and comprise more than 35 hours of ON-source observation.

4.2 Test Analysis Method: Crab Offset Data

There is a fairly large dataset on which the analysis, which was described in the previous section, can be tested. Through the 2002-2003 observing season, there were approximately 30 hours of ON-source data (with corresponding OFF-source data) taken with the Crab Nebula offset from the center of the field of view. A summary of the data tested with this analysis is provided in Table 4.1

Figure 4.25 shows the 2-D significance maps for the Crab at offsets of 0.3°, 0.5°, 0.8°, and 1.3°. The scale to the right of each plot gives the pretrials significance in σ, calculated using the method described by Li and Ma [60]. The cuts used here are

- $Size > 400 ADC$
- $Width < 0.02 \ln(Size)$

Table 4.1. Summary of Crab Nebula offset observations

Offset	Exposure (hours)	Observation Period	Elevation (hours)	Weather (hours)
0.3°	6.1	Dec00 - Dec02	$> 70°$: 4.7 $60° - 70°$: 0.9 $50° - 60°$: 0.5	A: 5.1 B: 0.9 C: 0
0.5°	5.1	Feb00 - Apr02	$> 70°$: 2.3 $60° - 70°$: 1.4 $50° - 60°$: 0.5 $40° - 50°$: 0	A: 3.7 B: 1.4 C: 0.9 C: 0.5
0.8°	7.5	Dec00 - Dec02	$> 70°$: 4.2 $60° - 70°$: 2.3 $50° - 60°$: 0 $40° - 50°$: 0	A: 5.6 B: 1.9 C: 0 C: 0.9
1.0°	3.3	Feb00 - Nov02	$> 70°$: 1.9 $60° - 70°$: 1.4 $50° - 60°$: 0	A: 2.8 B: 0.5 C: 0
1.3°	6.5	Dec00-Mar03	$> 70°$: 3.3 $60° - 70°$: 2.3 $50° - 60°$: 0.9	A: 6.1 B: 0.5 C: 0

- $Length < 0.02 \ln(Size) + (0.052°(O)^2 + 0.056°(O) + 0.14°)$
- $\chi^2 Parameter < 1$
- $Alpha < 10°$ (with pointing)
- $\frac{Distance}{1 - Width/Length} > 0.12 \ln(Max1 + Max2) + 0.15$
- $\frac{Distance}{1 - Width/Length} < 0.12 \ln(Max1 + Max2) + (0.26(O)^2 - 1.11(O) + 2.0)$
- $Length/Size < 0.00045$.

The last cut was derived from the Crab offset data and is slightly higher than in the standard Supercuts, but this is to be expected since the *Length* increases for an offset source.

Each 2-D significance map is $1.5° \times 1.5°$, and the grid spacing is $0.1°$ along each axis. Thus, each map has 961 grid points (31×31), and so the significance

was calculated 961 times. The 961 significances may be histogrammed to find the distribution of significances; if no source were present, the distribution (on average) would be Gaussian with a width of 1. Figure 4.26 shows the distribution of significances for all of the Crab offset maps combined. Since the Crab is in the field of view, the distribution deviates significantly from the curve labelled 'Null Distribution', which is the expected distribution if no source were present.

As can be seen from Figure 4.25, the Crab shows up with good significance, even out to 1.3° offset. However, it is worthwhile to examine the effect of each cut in more detail. The following Figures were made using all of the Crab offset data combined, but with the *Alpha* (without pointing, for now) and *Distance* cuts applied with respect to the location of the Crab. A lower *Size* cut of 400 ADC, along

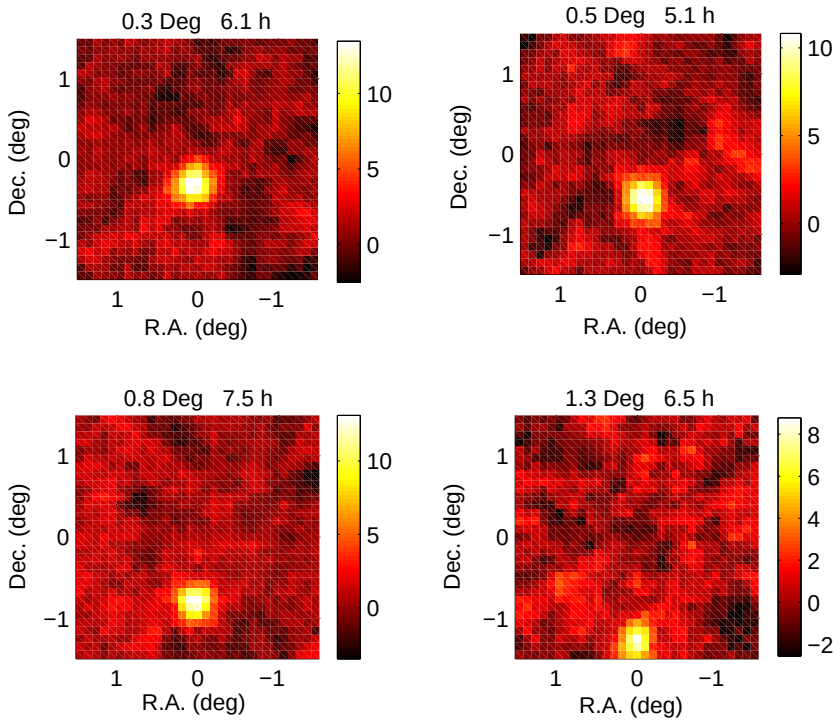

Figure 4.25. 2-D significance maps for the Crab Nebula. The offset for each map is noted at the top of each map, as well as the ON-source exposure. The scale is in pre-trials significance in σ. The R.A. and Dec. scales are relative to the center of the field of view.

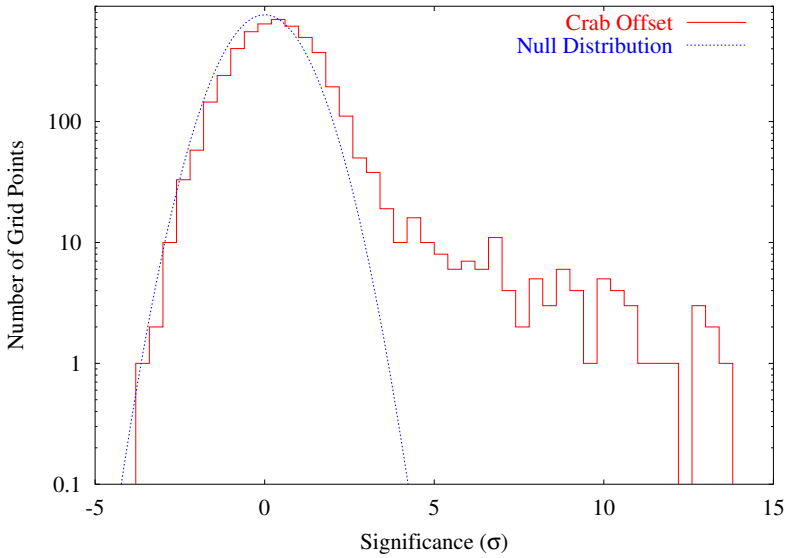

Figure 4.26. Distribution of significances for the five Crab offset 2-D significance maps combined. The 'Null Distribution' curve shows the expected distribution if no source were present. It is just a Gaussian distribution with a mean of 0, a width of 1, and an amplitude of $(0.4 \times 5 \times 961)/\sqrt{2\pi}$. The factor 961 is the number of points in each map, and 0.4 is the bin width. Note that the y-axis is on a log scale.

with the $Length/Size$ cut were also applied. Figure 4.27 shows the $Width/ln(Size)$ distributions for ON and OFF source. Figure 4.28 shows the $(Length - (0.052(O)^2 + 0.056(O) + 0.14))/ln(Size)$ distributions after the $Width$ cut. The χ^2 parameter distributions are shown in Figure 4.29, and here the $Width$ and $Length$ cuts have already been applied. Based on the figures, all of the cuts seem reasonably placed.

To check the pointing method, it is instructive to break the events that pass the previous cuts into two $Size$ regions since different behavior is expected. Figure 4.30 shows the $Alpha$ plot for $400ADC < Size < 1000ADC$, while Figure 4.31 is for $1000ADC < Size$. In both figures, $Alpha$ was calculated using the compromise pointing method described earlier.

As was seen in the simulations, the pointing is more accurate for larger events, but in both cases it is quite accurate. For the $400ADC < Size < 1000ADC$ case, 22% of the events are mis-pointed, and the background drops by 43%. For $1000ADC < Size$, 14% of the events are mis-pointed, and the background drops

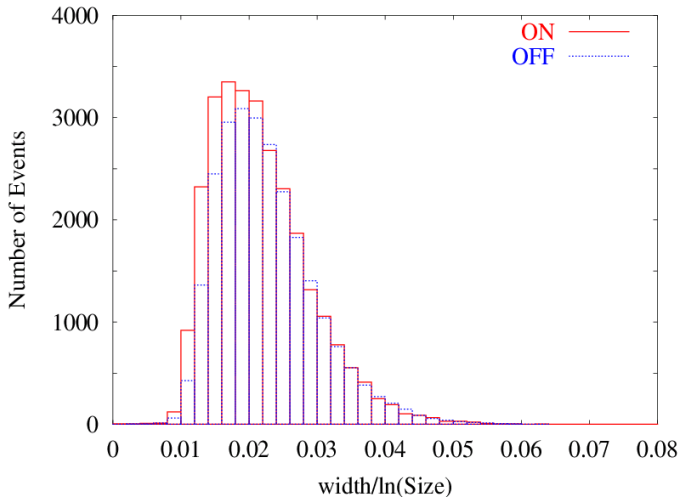

Figure 4.27. *Width*/*ln*(*Size*) distribution for all Crab offset data combined. *Alpha*, *Distance*, *Size*, and *Length*/*Size* cuts, as described in the text, have already been applied to weed out some of the background, with *Alpha* and *Distance* calculated with respect to the location of the Crab. This figure shows that the line $0.02\ln(Size) + 0.0°$ provides a reasonable upper *Width* cut.

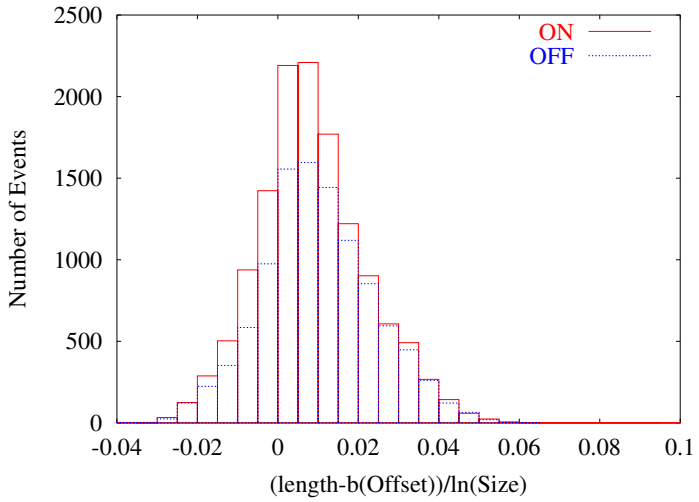

Figure 4.28. $(Length - (0.052°(O)^2 + 0.056°(O) + 0.14°))/\ln(Size)$ distribution for all Crab offset data combined, after the *Width* cut. *Alpha*, *Distance*, *Size*, and *Length*/*Size* cuts, as described in the text, have also been applied, with *Alpha* and *Distance* calculated with respect to the location of the Crab. This figure shows that the line $0.02°\ln(Size) + (0.052°(O)^2 + 0.056°(O) + 0.14°)$ provides a reasonable upper *Length* cut.

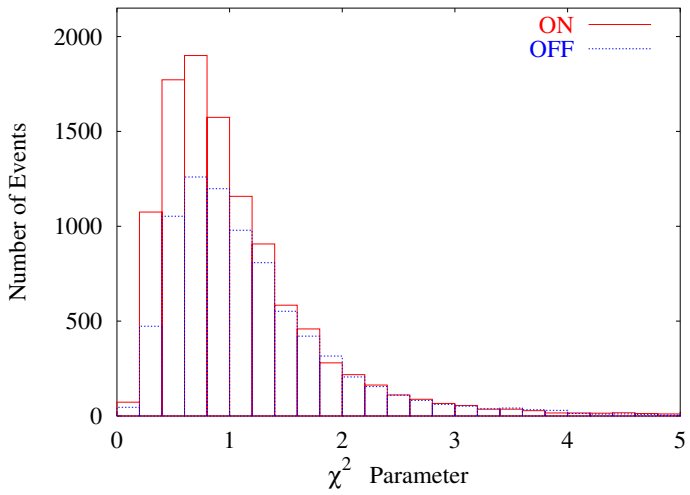

Figure 4.29. χ^2 Parameter distributions for the Crab offset data combined, after the *Width* the *Length* cuts. *Alpha*, *Distance*, *Size*, and *Length*/*Size* cuts, as described in the text, have also been applied, with *Alpha* and *Distance* calculated with respect to the location of the Crab. The cut used in this analysis is χ^2 Parameter < 1.0.

by 49%. Thus, it is especially useful for high energy gamma rays.

As was stated earlier, one of the goals for this analysis was to allow high-energy gamma rays through the cuts. Table 4.2 shows the results of the analysis for the Crab, both on-axis and off-axis, broken down into different *Size* regions. The analysis described here is labeled NEW, and the results using Supercuts, labeled SC, are included for comparison. Crab Center is for data taken with the Crab on-axis. Crab Inner is a combination of the 0.3° and 0.5° offset data, and Crab Outer includes the 0.8°, 1.0°, and 1.3° offset data. In each case, the significance is estimated using the simple formula $(ON - OFF)/\sqrt{ON + OFF}$.

As is seen in the table, there is not a large difference between Supercuts and the new cuts near the center of the field of view. In the outer regions, however, the new cuts are much more sensitive.

In conclusion, the analysis described here works well for 2-D analysis, and it is well-suited for high energy gamma rays. Its effectiveness has been demonstrated with the Crab offset data.

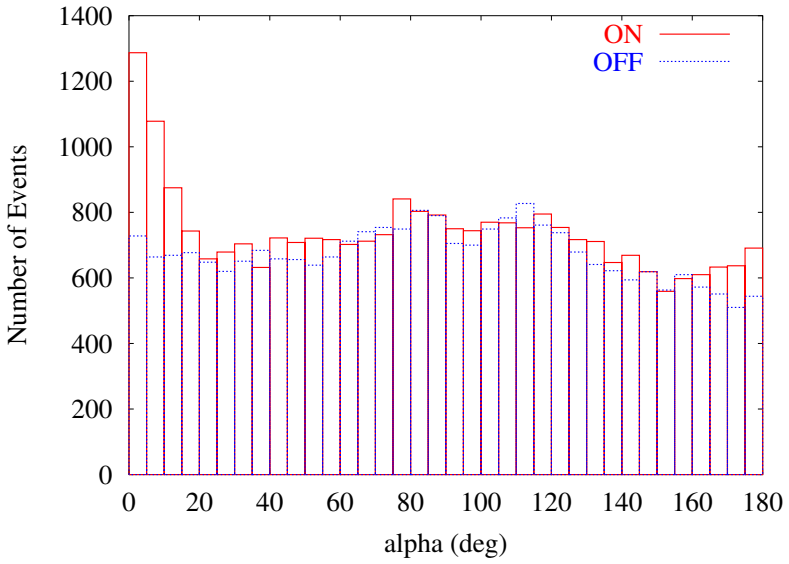

Figure 4.30. *Alpha* plot for $400 ADC < Size < 1000 ADC$ for combined Crab offset data, with *Alpha* calculated with respect to the location of the Crab. All other cuts have been applied.

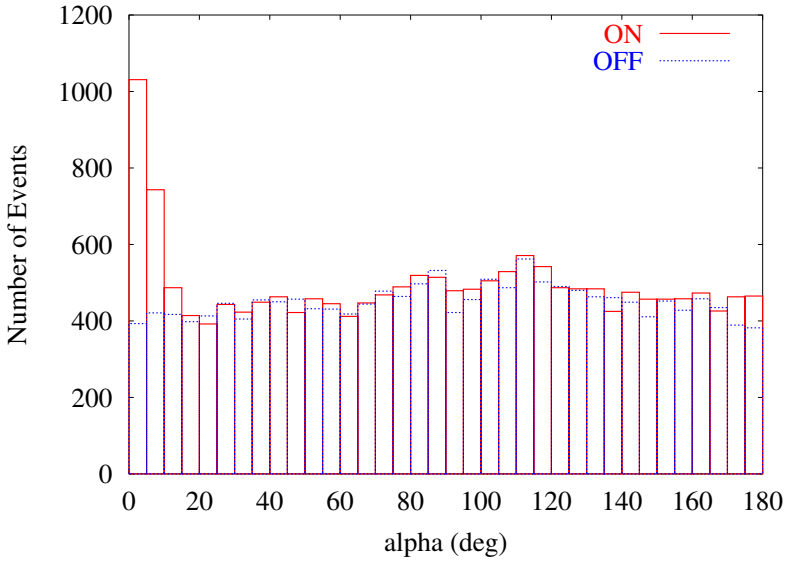

Figure 4.31. *Alpha* plot for $1000 ADC < Size$ for combined Crab offset data, with *Alpha* calculated with respect to the location of the Crab. All other cuts have been applied.

Table 4.2. Summary of Crab Nebula offset data

		< 1000			$1000 - 4000$			> 4000		
		ON	OFF	Signif.	ON	OFF	Signif.	ON	OFF	Signif.
Crab	SC	2350	1378	15.9σ	738	249	15.6σ	58	2	7.2σ
Center	NEW	1732	872	16.9σ	914	392	14.4σ	131	39	7.1σ
Crab	SC	2226	1577	10.5σ	445	135	12.9σ	14	2	3.0σ
Inner	NEW	1537	936	12.1σ	734	359	11.7σ	107	49	4.6σ
Crab	SC	1736	1356	6.8σ	402	194	8.5σ	9	2	2.3σ
Outer	NEW	828	456	10.4σ	749	338	12.5σ	177	72	6.7σ

CHAPTER 5

ANALYSIS OF THE DATA

5.1 Data Summary

The Whipple observations of the Tibet gamma-ray source candidates are summarized in Table 5.1; only data used in the analysis are included in this table. The elevation given is the mid-run elevation of the target. The weather was estimated by combining the observer's estimate of sky quality with the cosmic-ray throughput. The 'C' weather data for Tibet14 is of reasonable quality based on these factors, but it should be noted that other data were dropped.

Table 5.1. Summary of Whipple observations of Tibet targets

Name	RA	Dec	Whipple Observations	Exposure (hours)	Elevation (hours)	Weather (hours)
Tibet1	3.79 h	34.2°	Oct01 - Feb02	5.1	$> 70°$: 4.2 $60° - 70°$: 0.9 $50° - 60°$: 0	A: 3.7 B: 1.4 C: 0
Tibet9	13.64 h	24.2°	Feb02 - Jun02	4.2	$> 70°$: 2.8 $60° - 70°$: 0.9 $50° - 60°$: 0.5	A: 3.3 B: 0.9 C: 0
Tibet14	20.36 h	37.9°	May02 - Jul02	4.2	$> 70°$: 2.8 $60° - 70°$: 1.4 $50° - 60°$: 0	A: 2.3 B: 0.5 C: 1.4
Tibet16	21.49 h	45.3°	Oct01 - Jun02	4.2	$> 70°$: 2.3 $60° - 70°$: 1.9 $50° - 60°$: 0	A: 0.4 B: 3.7 C: 0
Tibet0554	5.91 h	30.1°	Dec02-Feb03	7.9	$> 70°$: 4.7 $60° - 70°$: 2.3 $50° - 60°$: 0.9	A: 6.1 B: 1.9 C: 0

5.2 Analysis Logistics

It is useful to outline the 2-D analysis process. Once the camera has been calibrated (see Chapter 3), each event is cleaned and parameterized (centroid, length, width, etc.). Each event is derotated, as described below, and the shape cuts are applied. The remaining events populate the 2-D grid according to the *Alpha* and *Distance* cuts, and the signal at each grid point is compared to the estimated background, which is also discussed below.

5.2.1 Field Derotation

Because the Whipple Telescope is on an altazimuth mount (one axis points to zenith), field rotation results as it tracks each target about the celestial pole. This is manifested as a rotation about the center of the camera. For example, an off-axis star moves along an arc about the camera center as field rotation occurs, as is shown in Figure 5.1. The rotation angle may be defined as the angle between the line to the pole (the declination axis) and the line to zenith (the altitude axis). This is illustrated in Figure 5.2. The spherical law of sines is used to relate the rotation angle R to the hour angle H, so that

$$\sin(R) = \frac{\cos(L)\sin(H)}{\sin(Z)},$$

where L is the latitude and Z is the zenith angle. An Euler rotation may be used to express $\sin(Z)$ $(= \cos(Altitude))$ in terms of hour angle and declination (D), so that the rotation angle is given as

$$R = \sin^{-1}\left[\frac{\cos L \sin H}{\sqrt{(\sin D \cos L - \cos H \cos D \sin L)^2 + \sin^2 H \cos^2 D}}\right].$$

For this analysis, all of the data has been derotated to the $H = 0$ position. This way, runs on the same target but at different hour angles can be co-added.

5.2.2 Background Estimation

All of the observations for Tibet0554 included corresponding OFF-source data, which allows a straightforward estimation of the background. Unfortunately, almost no OFF-source observations were made for the other four targets. In their case,

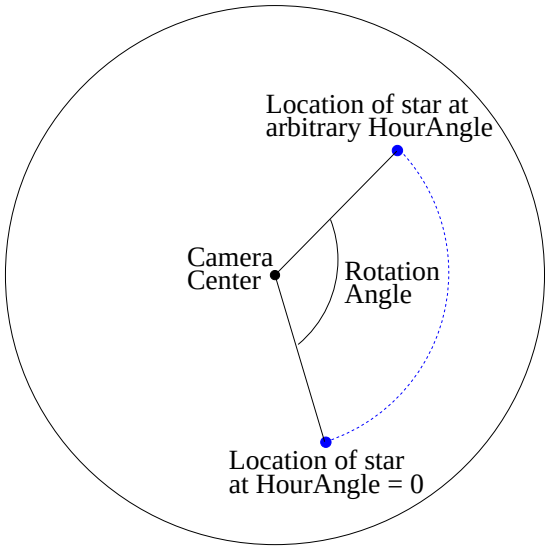

Figure 5.1. Field rotation as seen in the camera. The rotation angle may be given as a function of the declination and hour angle of the camera center, and the latitude (measured from Earth's equator).

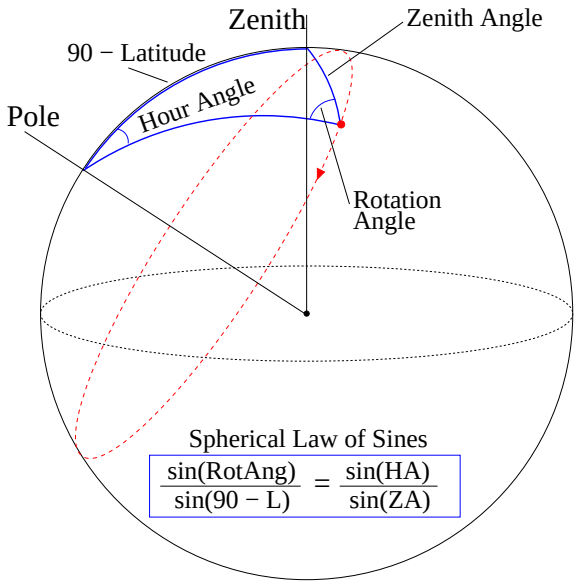

Figure 5.2. For an altazimuth mount tracking the dot about the pole, the field rotation angle is the angle between the declination axis (the line to the pole) and the altitude axis (the line to zenith). The spherical law of sines may be used to relate the rotation angle to the hour angle, the latitude, and the zenith angle.

a combination of many OFF runs for other targets was used to find the average behavior of the background across the camera. In general, the background was found to depend on both r and ϕ, where r is the radial distance from the camera center, and ϕ is the polar angle about the center of the camera. In addition, camera pixels that were turned off because of field stars were found to create spots of false excess relative to the average background.

To correct for the effects of off pixels, a set of ~ 10 OFF runs was chosen for each ON-source run. These were required to have no bright field stars (no extra pixels turned off) and to come from roughly the same time as the target run. The set was then padded by the target run, analyzed with the same pixels turned off that were off in the target run, and derotated according to the ON-source derotation. Finally, the set was used to generate a map of tracking ratios (described in Chapter 3) for the 2-D grid. At grid point i, the tracking ratio TR_i is defined as the ratio of the number of events in the $0^\circ < Alpha_i < 10^\circ$ region to the number in the $20^\circ < Alpha_i < 65^\circ$ region. This way, the background at grid point i in the ON-source data was estimated as the number of events in the $20^\circ < ONAlpha_i < 65^\circ$ region, multiplied by TR_i.

This method was found to provide a good estimate of the background. Figures 5.3 and 5.4 show both types of analysis applied to the same ON-source data. In each figure, roughly the same structure can be seen. It should be noted, however, that the method is not well suited for an extended source.

5.3 Analysis Results

5.3.1 2-D Maps: Significance

The 2-D analysis has been applied to the data for the five Tibet targets. Figure 5.5 shows the 2-D significance map for the Tibet1 region, and the corresponding distribution of significance is shown in Figure 5.6. Similarly, Figures 5.7 and 5.8 are for the Tibet9 region, Figures 5.9 and 5.10 are for the Tibet14 region, Figures 5.11 and 5.12 are for the Tibet16 region, and Figures 5.13 and 5.14 are for the Tibet0554 region. In each of the significance maps, the scale represents the significance in pretrials σ, where the significance was calculated using the method described by

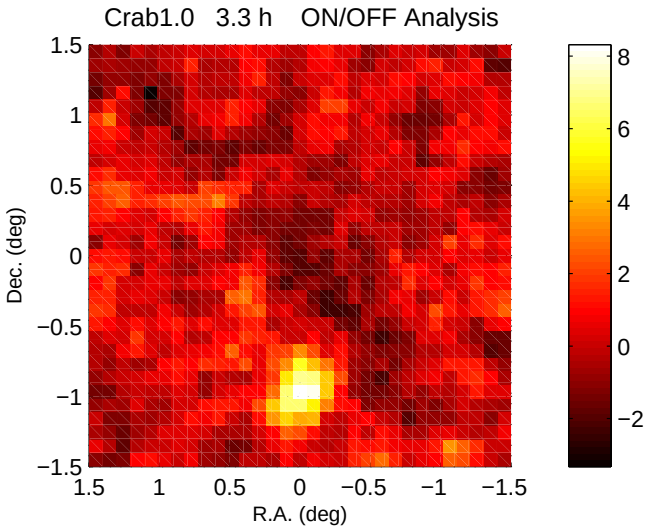

Figure 5.3. 2-D significance map for the Crab nebula at 1° offset with a 3.3 h exposure. The scale to the right represents significance in pretrials σ. The background at each grid point was estimated directly from corresponding OFF-source data.

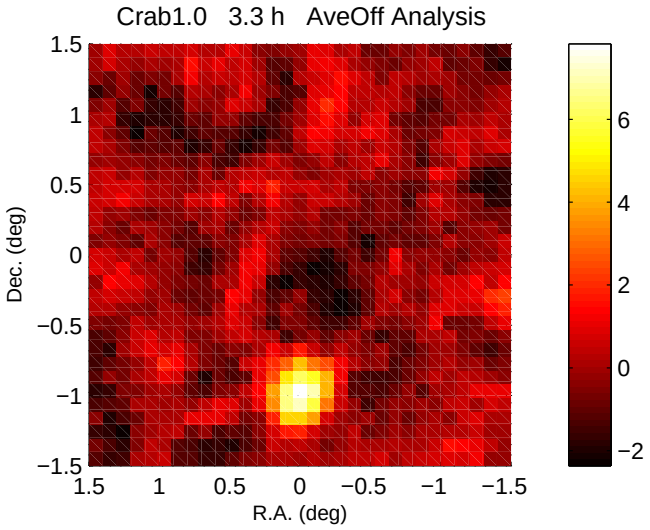

Figure 5.4. 2-D significance map for the Crab nebula at 1° offset with a 3.3 h exposure. The scale to the right represents significance in pretrials σ. The background at each grid point was estimated using many OFF-source runs from other targets. The OFF set was used to find a tracking ratio map suitable for this field, and this map was applied to the ON-source data.

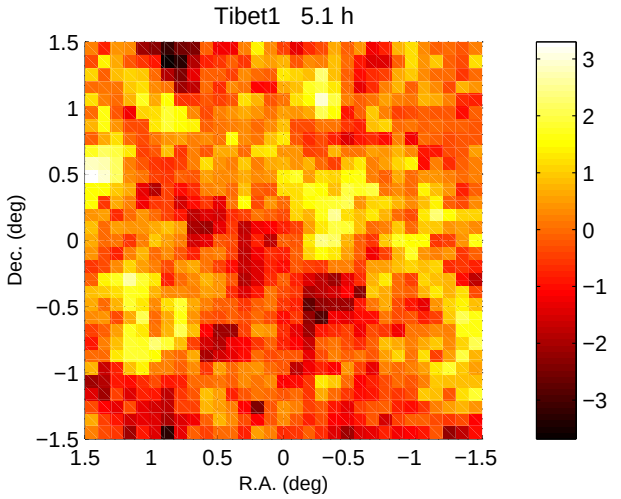

Figure 5.5. 2-D significance map for a 5.1 hour exposure centered on the Tibet1 coordinates. The x and y axes are relative to the Tibet1 coordinates (3h47m12s, $+34.2°$), and the units are true degrees. The scale to the right represents the significance in pretrials σ. For the inner $1°$, the maximum pretrials significance is 2.5σ. The background for this map was estimated using a combination of many OFF runs from other targets.

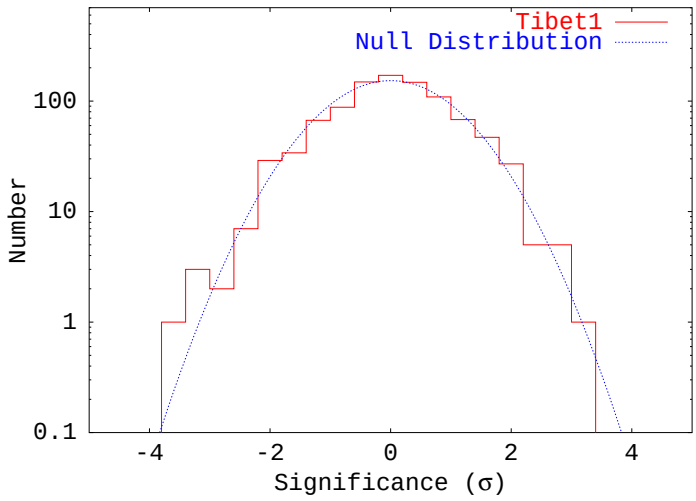

Figure 5.6. Distribution of significances from the 2-D significance map for Tibet1. The 'Null Distribution' curve shows the expected distribution if no source were present. It is just a Gaussian distribution with a mean of 0, a width of 1, and an amplitude of $(0.4 \times 961)/\sqrt{2\pi}$. The factor 961 is the number of points in each map, and 0.4 is the bin width. Note that the y-axis is on a log scale.

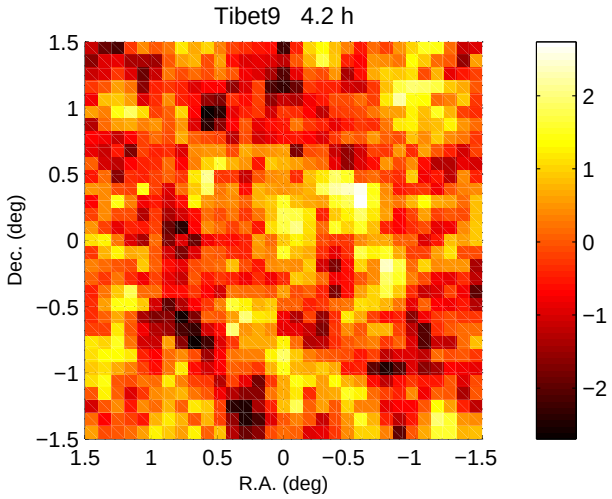

Figure 5.7. 2-D significance map for a 4.2 hour exposure centered on IRAS 13349+2438 (a Seyfert 1 galaxy), near the Tibet9 coordinates. The x and y axes are relative to the coordinates (13h37m18s, +24.38°), and the units are true degrees. The scale to the right represents the significance in pretrials σ. For the inner 1°, the maximum pretrials significance is 2.7σ. The background for this map was estimated using a combination of many OFF runs from other targets.

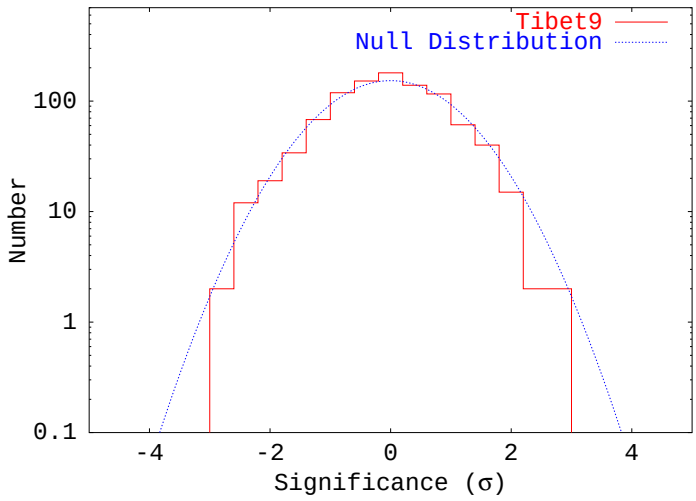

Figure 5.8. Distribution of significances from the 2-D significance map for Tibet9. The 'Null Distribution' curve shows the expected distribution if no source were present. It is just a Gaussian distribution with a mean of 0, a width of 1, and an amplitude of $(0.4 \times 961)/\sqrt{2\pi}$. The factor 961 is the number of points in each map, and 0.4 is the bin width. Note that the y-axis is on a log scale.

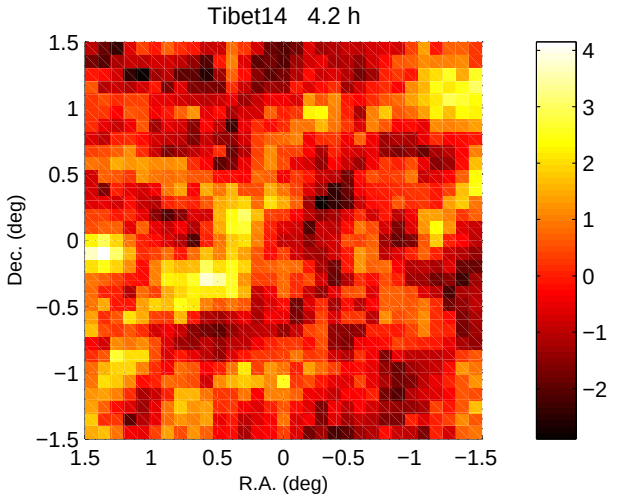

Figure 5.9. 2-D significance map for a 4.2 hour exposure centered on the Tibet14 coordinates. The x and y axes are relative to the Tibet14 coordinates (20h21m36s, +37.9°), and the units are true degrees. The scale to the right represents the significance in pretrials σ. For the inner 1°, the maximum pretrials significance is 3.8σ. The background for this map was estimated using a combination of many OFF runs from other targets.

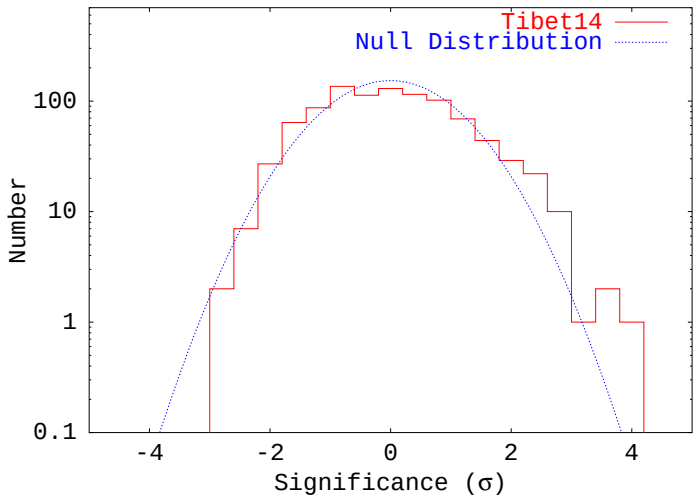

Figure 5.10. Distribution of significances from the 2-D significance map for Tibet14. The 'Null Distribution' curve shows the expected distribution if no source were present. It is just a Gaussian distribution with a mean of 0, a width of 1, and an amplitude of $(0.4 \times 961)/\sqrt{2\pi}$. The factor 961 is the number of points in each map, and 0.4 is the bin width. Note that the y-axis is on a log scale.

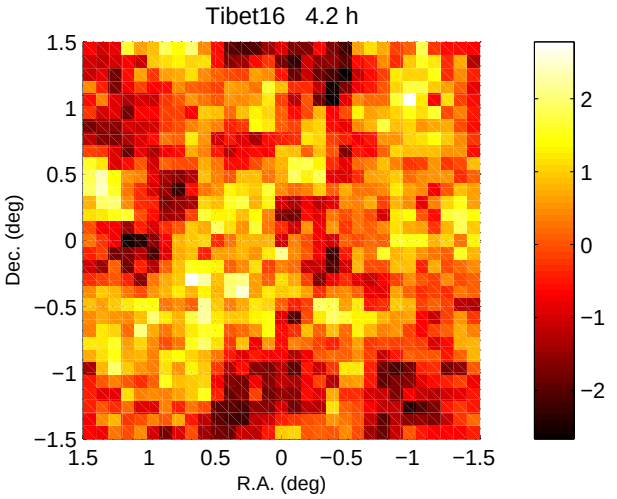

Figure 5.11. 2-D significance map for a 4.2 hour exposure centered on the Tibet16 coordinates. The x and y axes are relative to the Tibet16 coordinates (21h29m36s, +45.3°), and the units are true degrees. The scale to the right represents the significance in pretrials σ. For the inner 1°, the maximum pretrials significance is 2.8σ. The background for this map was estimated using a combination of many OFF runs from other targets.

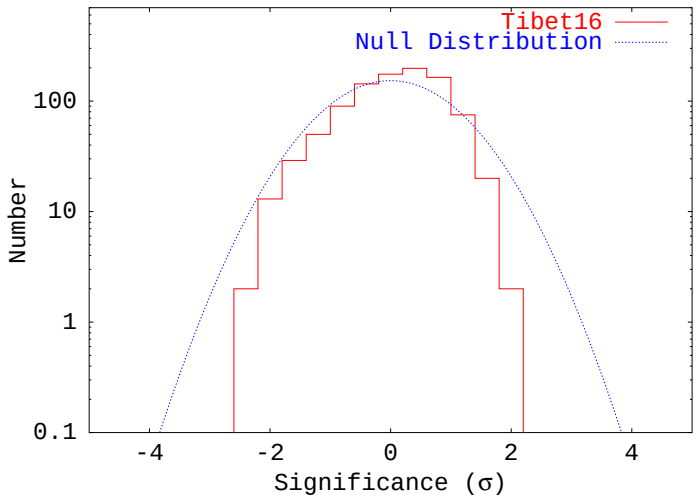

Figure 5.12. Distribution of significances from the 2-D significance map for Tibet16. The 'Null Distribution' curve shows the expected distribution if no source were present. It is just a Gaussian distribution with a mean of 0, a width of 1, and an amplitude of $(0.4 \times 961)/\sqrt{2\pi}$. The factor 961 is the number of points in each map, and 0.4 is the bin width. Note that the y-axis is on a log scale.

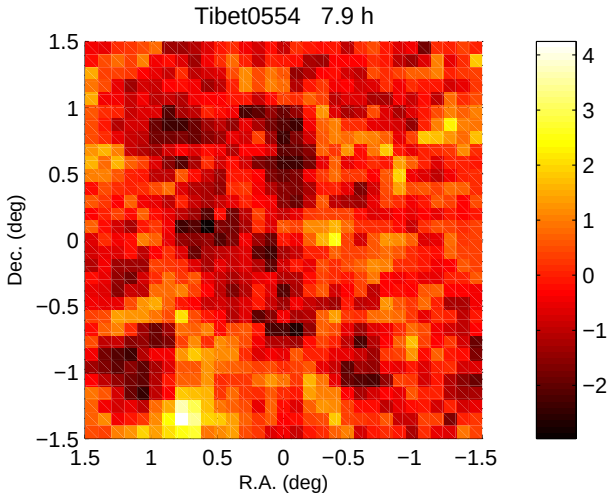

Figure 5.13. 2-D significance map for a 7.9 hour exposure centered on the Tibet0554 coordinates. The x and y axes are relative to the Tibet0554 coordinates (5h54m48s, +30.1°), and the units are true degrees. The scale to the right represents the significance in pretrials σ. For the inner 1°, the maximum pretrials significance is 2.5σ. The background for this map was estimated directly from corresponding OFF-source data.

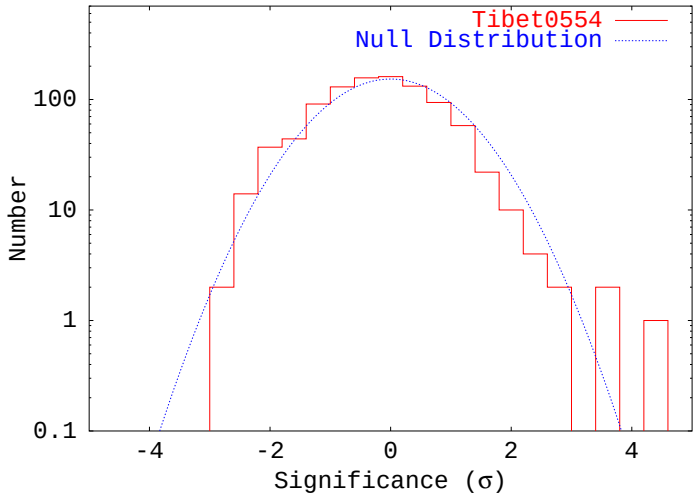

Figure 5.14. Distribution of significances from the 2-D significance map for Tibet0554. The 'Null Distribution' curve shows the expected distribution if no source were present. It is just a Gaussian distribution with a mean of 0, a width of 1, and an amplitude of $(0.4 \times 961)/\sqrt{2\pi}$. The factor 961 is the number of points in each map, and 0.4 is the bin width. Note that the y-axis is on a log scale.

Li and Ma [60]. As can be seen from the significance maps, no source has been detected in any of the regions. Moreover, all of the distributions of significance are in reasonable agreement with the Gaussian 'Null Distribution' curve, which is the expected distribution if no source is present.

5.3.2 Upper Limits

As was noted above, the 2-D analysis has failed to detect a gamma-ray source in any of the Tibet regions. Therefore, it is worthwhile to estimate the gamma-ray flux upper limits for each region. The upper limits are calculated across a range of offsets, and so an understanding of the detector response versus source offset is desirable.

5.3.2.1 Response vs. Offset

The effect of source offset on the sensitivity has been estimated using real Crab data as well as simulations. The 2-D analysis was applied to 93 ON/OFF pairs with the Crab on-axis, and an average of 68 γ/run was found to pass the cuts (2.4 γ/min). The same calculation was performed with the Crab at offsets of 0.3°, 0.5°, 0.8°, 1.0°, and 1.3°, and the scaled results are shown in Figure 5.15. The Figure also includes estimates provided by the simulations. The efficiency may be more complicated than the simple curve shown in the figure, but the estimator is reasonably accurate.

5.3.3 2-D Maps: Upper Limits

For each region, the 95% flux upper limits were calculated at each grid point using the Helene method [67]. Figures 5.16, 5.17, 5.18, 5.19, and 5.20 give the 2-D upper limit maps for each region, in terms of number per run. To give values across the map the same meaning, the upper limit at each grid point has been divided by the estimated response $R_{\rm est}$ (given by $R_{\rm est} = 0.35(O)^2 - 1.0(O) + 1.0$).

To give a reference point by which the upper limits may be interpreted, Table 5.2 shows the flux expected for each target if a point source were present, given the Tibet AS measurement. Because TibetAS has a higher energy threshold than

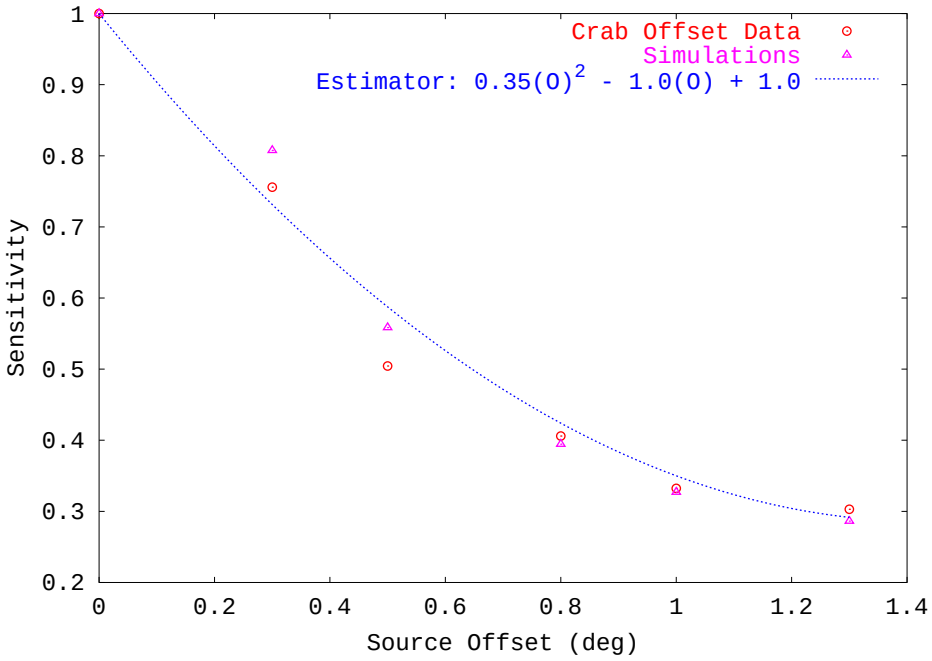

Figure 5.15. Efficiency versus source offset, relative to a source at the center of the field of view. The error bars are not shown for clarity but are around 0.05 for the Crab offset data and 0.005 for the simulated data. The estimator is a function of the source offset.

Whipple (3 TeV compared to ∼300 GeV), the source spectral index is important, and so spectral indices of -2.5, -2.25, -2.0, -1.75, and -1.5 are included in the table. (No energy cut is used here, for reasons discussed in the next section.) The values in the table were obtained by applying the analysis to simulated datasets with each of the given spectral indices. The five datasets were constrained (precuts) to have the same number of events above 3 TeV. As an example, the flux expected if a -2.0 spectral index source were present is given by

$$F_{-2.0} = \left(\frac{N_{-2.0}}{N_{-2.5}}\right) \Phi_c R_T,$$

where $N_{-2.0}$ is the number of events to pass the cuts from the -2.0 spectrum dataset, and $N_{-2.5}$ is the number of events to pass for the simulated Crab spectrum. Thus, given a -2.0 spectrum point source with a flux of 1 Crab above 3 TeV, $(N_{-2.0}/N_{-2.5})$ is the flux ratio of that source to the Crab that would be seen by the Whipple telescope. This was related to real data by the Crab flux seen by the Whipple

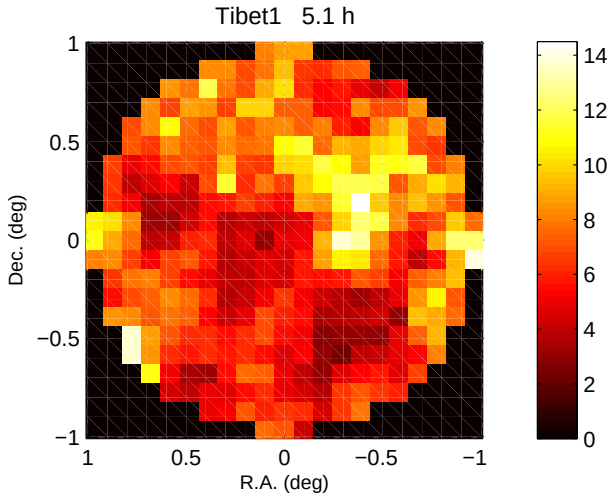

Figure 5.16. 2-D 95% upper limit map for the Tibet1 region. The scale to the right is in units of number per run. To give values across the map the same meaning, the value at each grid point has been scaled according to the estimated sensitivity. Based on the Tibet AS measurement for Tibet1 (Tib1Sig/CrabSig=1.0), the expected flux is 68γ/run for a -2.5 spectral index, 24γ/run for a -2.0 spectral index, and 7.6γ/run for a -1.5 spectral index.

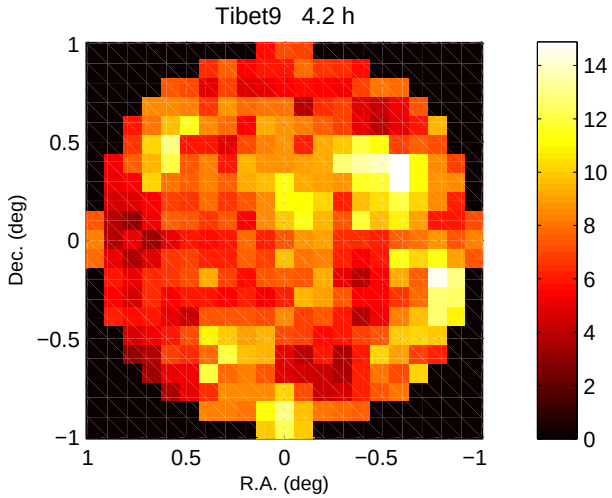

Figure 5.17. 2-D 95% upper limit map for the Tibet9 region, in units of number per run. To give values across the map the same meaning, the value at each grid point has been scaled according to the estimated sensitivity. Based on the Tibet AS measurement for Tibet9 (Tib9Sig/CrabSig=0.9), the expected flux is 61γ/run for a -2.5 spectral index, 21γ/run for a -2.0 spectral index, and 6.8γ/run for a -1.5 spectral index.

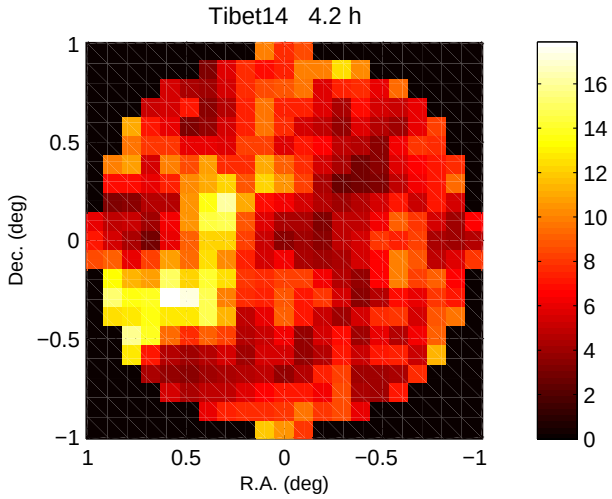

Figure 5.18. 2-D 95% upper limit map for the Tibet14 region, in units of number per run. To give values across the map the same meaning, the value at each grid point has been scaled according to the estimated sensitivity. Based on the Tibet AS measurement for Tibet14 (Tib14Sig/CrabSig=0.9), the expected flux is 61γ/run for a -2.5 spectral index, 21γ/run for a -2.0 spectral index, and 6.8γ/run for a -1.5 spectral index.

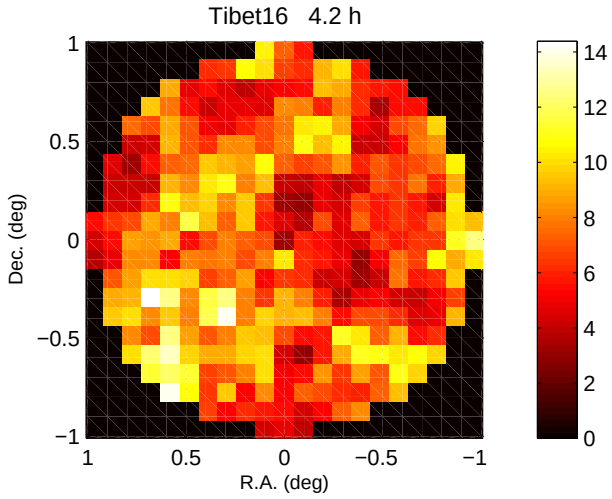

Figure 5.19. 2-D 95% upper limit map for the Tibet16 region, in units of number per run. To give values across the map the same meaning, the value at each grid point has been scaled according to the estimated sensitivity. Based on the Tibet AS measurement for Tibet16 (Tib16Sig/CrabSig=1.0), the expected flux is 68γ/run for a -2.5 spectral index, 24γ/run for a -2.0 spectral index, and 7.6γ/run for a -1.5 spectral index.

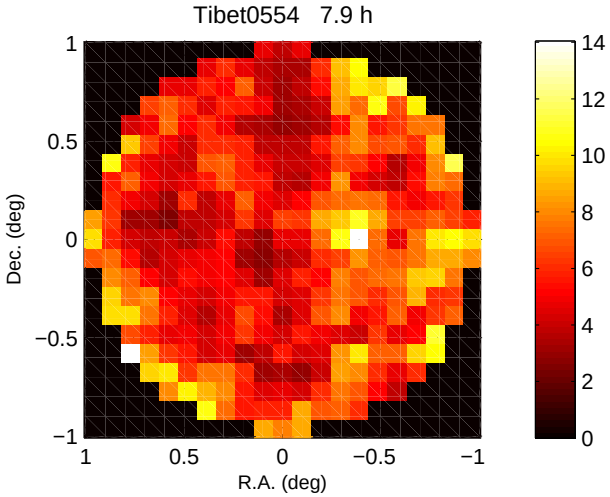

Figure 5.20. 2-D 95% upper limit map for the Tibet0554 region, in units of number per run. To give values across the map the same meaning, the value at each grid point has been scaled according to the estimated sensitivity. Based on the Tibet AS measurement for Tibet0554 (Tib0554Sig/CrabSig=0.9), the expected flux is 61γ/run for a -2.5 spectral index, 21γ/run for a -2.0 spectral index, and 6.8γ/run for a -1.5 spectral index.

Table 5.2. Expected flux for the Tibet targets, if a point source were present, across a range of spectral indices, in units of γ/run.

Name	Flux Ratio to Crab	-2.5 Spect	-2.25 Spect	-2.0 Spect	-1.75 Spect	-1.5 Spect
Crab	1	68	–	–	–	–
Tibet1	1.0	68	40	24	14	7.6
Tibet9	0.9	61	36	21	12	6.8
Tibet14	0.9	61	36	21	12	6.8
Tibet16	1.0	68	40	24	14	7.6
Tibet0554	0.9	61	36	21	12	6.8

telescope, Φ_c, which was measured at 68 γ/run. Finally, R_T is the flux ratio (to the Crab) measured by Tibet AS, where the Tibet AS flux was assumed to scale linearly with significance.

As is seen in each of the 2-D maps, the 95% upper limits are below the expected flux down to a -1.75 spectrum, at which point the upper limits and the expected flux are approximately equal.

5.3.4 2-D Maps: Energy Cuts Applied

Tibet AS has an energy threshold of 3 TeV, while the threshold for Whipple is around 300 GeV. Because of this difference, if Tibet AS detected a source with a non Crab-like spectrum (a monochromatic line source, for example), it may be washed out in the Whipple data unless energy cuts were applied. The effect of a lower-limit energy cut was investigated using simulations with spectral indices of -2.5, -2.25, -2.0, -1.75, and -1.5, and improved sensitivity was seen only for the -1.5 index (the improvement was modest). Therefore, only monochromatic line sources are considered here. Simulations indicate that for a 3 TeV line source with a flux equal to 1 Crab above 3 TeV, the sensitivity is maximized when a lower-limit energy cut of $\sim$ 2 TeV is used. Similarly, for a 7 TeV line source, a lower-limit energy cut of $\sim$5 TeV is best. Unfortunately, the Crab flux above 3 TeV is very low, and according to simulations, none of the exposures was long enough to detect such a low flux. As expected, nothing of interest is found in any of the significance maps, and so they are not shown. However, upper limits have been calculated. Figures 5.21, 5.22, 5.23, 5.24, and 5.25 show the 95% upper limits per run when lower-limit energy cuts of 2 TeV and 5 TeV are applied. As before, the upper limit values across the map have been scaled by the response as a function of offset.

A reference point is needed to give the upper limits meaning. Table 5.3 shows the flux expected from each target if a monochromatic point source were present, given the Tibet AS measurement. The values were obtained by applying the analysis to simulated 3.2 TeV and 7.5 TeV datasets, as well as a simulated dataset with a -2.5 spectral index (to simulate the Crab). The three datasets were constrained to have an equal number of events (pre-cuts) above 3 TeV. The expected flux for a given

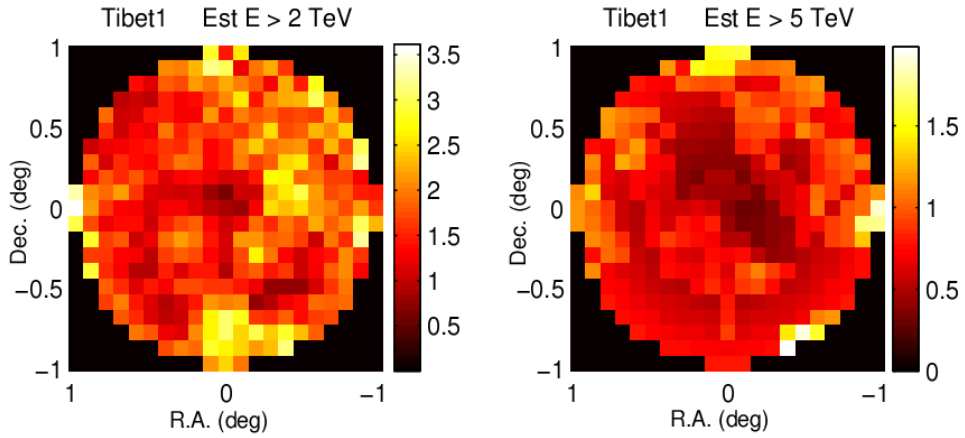

Figure 5.21. 2-D 95% upper limit maps for the Tibet1 region, with lower-limit energy cuts of 2 TeV applied on the left and 5 TeV applied on the right. The scale to the right of each map is in units of number per run. To give values across the map the same meaning, the value at each grid point has been scaled according to the estimated sensitivity. Based on the Tibet AS measurement for Tibet1 (Tib1Sig/CrabSig=1.0), the expected flux is 2.7γ/run for a 3 TeV line source and 2.3γ/run for a 7 TeV line source.

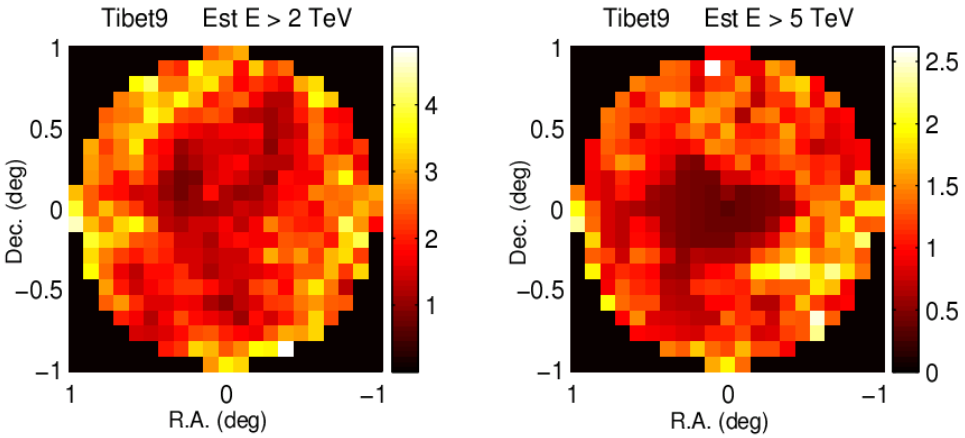

Figure 5.22. 2-D 95% upper limit maps for the Tibet9 region in units of number per run, with lower-limit energy cuts of 2 TeV applied on the left and 5 TeV applied on the right. To give values across the map the same meaning, the value at each grid point has been scaled according to the estimated sensitivity. Based on the Tibet AS measurement for Tibet9 (Tib9Sig/CrabSig=0.9), the expected flux is 2.4γ/run for a 3 TeV line source and 2.1γ/run for a 7 TeV line source.

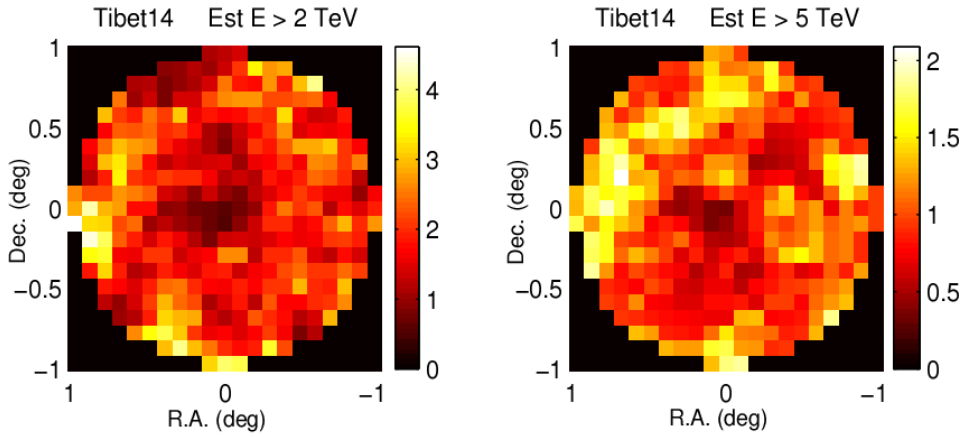

Figure 5.23. 2-D 95% upper limit maps for the Tibet14 region in units of number per run, with lower-limit energy cuts of 2 TeV applied on the left and 5 TeV applied on the right. To give values across the map the same meaning, the value at each grid point has been scaled according to the estimated sensitivity. Based on the Tibet AS measurement for Tibet14 (Tib14Sig/CrabSig=0.9), the expected flux is 2.4γ/run for a 3 TeV line source and 2.1γ/run for a 7 TeV line source.

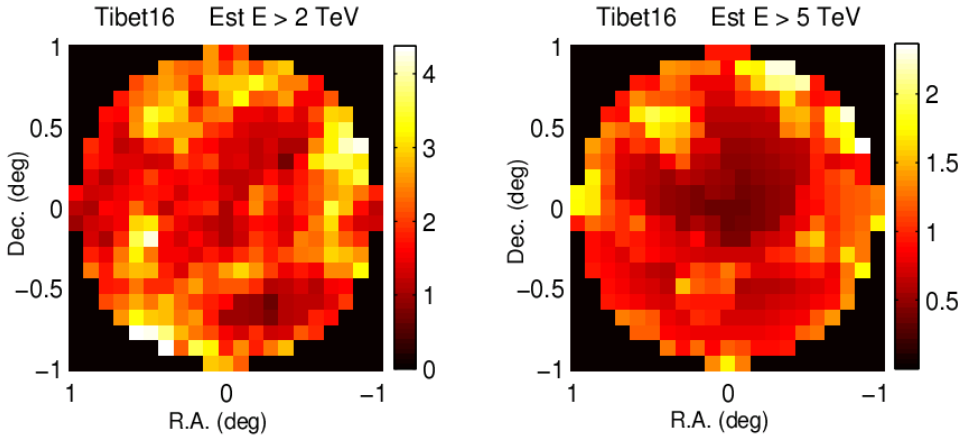

Figure 5.24. 2-D 95% upper limit maps for the Tibet16 region in units of number per run, with lower-limit energy cuts of 2 TeV applied on the left and 5 TeV applied on the right. To give values across the map the same meaning, the value at each grid point has been scaled according to the estimated sensitivity. Based on the Tibet AS measurement for Tibet16 (Tib16Sig/CrabSig=1.0), the expected flux is 2.7γ/run for a 3 TeV line source and 2.3γ/run for a 7 TeV line source.

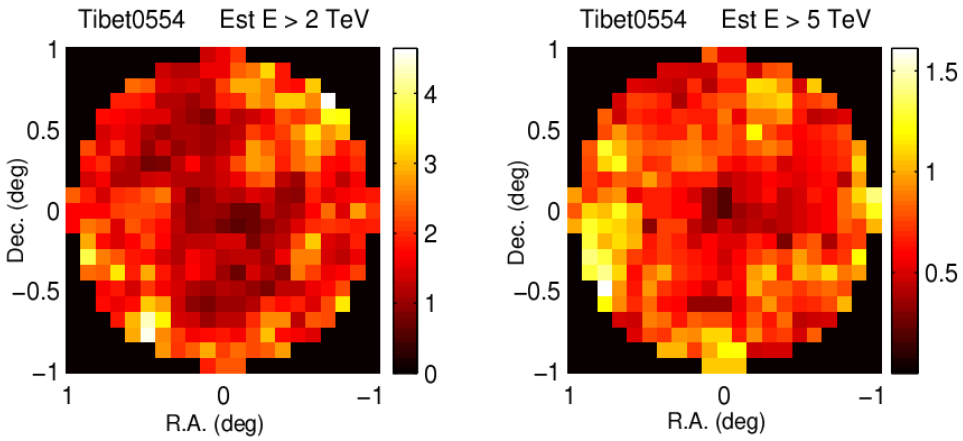

Figure 5.25. 2-D 95% upper limit maps for the Tibet0554 region in units of number per run, with lower-limit energy cuts of 2 TeV applied on the left and 5 TeV applied on the right. To give values across the map the same meaning, the value at each grid point has been scaled according to the estimated sensitivity. Based on the Tibet AS measurement for Tibet0554 (Tib0554Sig/CrabSig=0.9), the expected flux is 2.4γ/run for a 3 TeV line source and 2.1γ/run for a 7 TeV line source.

Table 5.3. Expected flux (given the Tibet AS measurement) for the Tibet targets if a monochromatic point source were present, in units of γ/run.

Name	Flux Ratio to Crab	3.2 TeV (γ/run)	7.5 TeV (γ/run)
Tibet1	1.0	2.7	2.3
Tibet9	0.9	2.4	2.1
Tibet14	0.9	2.4	2.1
Tibet16	1.0	2.7	2.3
Tibet0554	0.9	2.4	2.1

monochromatic line is

$$F_E = \left(\frac{N_e}{N_{-2.5}}\right) \Phi_c R_T,$$

where N_E is the number of simulated events that pass the cuts for monochromatic line energy E, and $N_{-2.5}$ is the number of events that pass for the simulated Crab spectrum. Thus, given a monochromatic line source with a flux of 1 Crab above 3 TeV, $(N_E/N_{-2.5})$ is the flux ratio to the Crab that would be seen by the Whipple telescope. This ratio was related to real data by the Crab flux seen by the Whipple telescope, Φ_c, which was measured at 68 γ/run. Finally, R_T is the flux ratio (to the Crab) measured by Tibet AS, where the Tibet AS flux was assumed to scale linearly with significance.

The upper limits in each 2-D map are above the expected values for a 3 TeV monochromatic source. For a 7 TeV line source, the upper limits are close to the expected values, and for Tibet1 and Tibet0554, they are actually below. Thus, for a monochromatic source, the Whipple measurements are unable to constrain the Tibet AS measurements for energies below $\sim 10TeV$.

CHAPTER 6

CONCLUSION

6.1 Whipple Observations: Discussion

Observations have been made by the Whipple telescope of five of the gamma-ray source candidates from the Tibet AS sky survey. As was noted in Chapter 5, no source was detected in any of the Whipple observations. However, it is useful to discuss each target field in a little more detail.

6.1.1 Tibet1

The EGRET unidentified gamma-ray source 3EG J0348+3510 [3] is 1.0° from the Tibet coordinates. This source was seen by EGRET with a flux of $\sim 5\%$ of the Crab and a spectral index of -2.16 ± 0.27. Figure 6.1 shows the EGRET measurement along with the 95% upper limit from the Whipple observation (assuming that the exact location of 3EG J0348+3510 lies within 1° of the Tibet1 coordinates) in a plot of the spectral energy distribution. The Whipple upper limit is the maximum found within 1° of the Tibet coordinates and 0.74° of the EGRET coordinates (0.74° is the 95% confidence radius). The two lines in the figure are the upper and lower limits of the spectral index extended out to VHE energies. The Whipple upper limit provides little constraint. However, if a single power-law spectrum is assumed (along with the assumption that the exact location of 3EG J0348+3510 lies within 1° of the Tibet1 coordinates), the Whipple upper limit constrains the spectral index to be less than -2.06.

6.1.2 Tibet9

The Seyfert 1 galaxy IRAS 13349+2438 is 0.3° from the Tibet9 coordinates. This active galaxy is at a redshift of $z = 0.107$ [68], and so it is unlikely to have been detected by Tibet AS due to the extragalactic background light (the interaction of

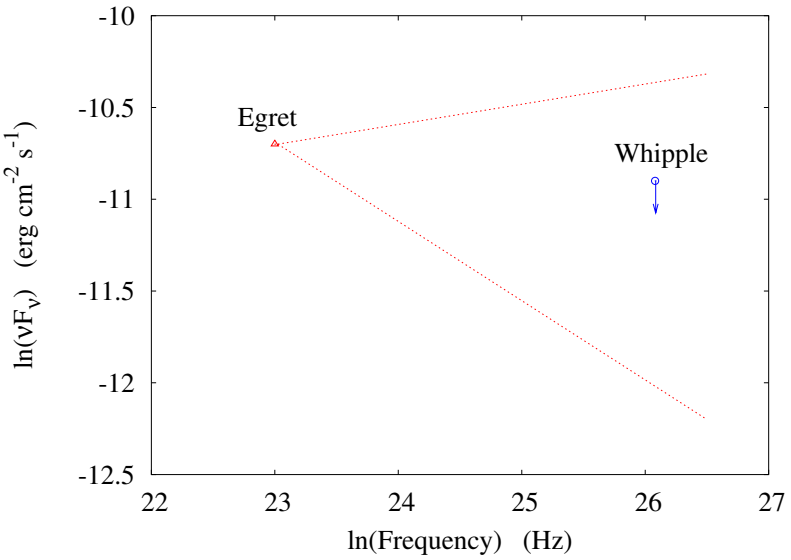

Figure 6.1. Spectral energy distribution for 3EG J0348+3510, showing the EGRET measurement with the Whipple upper limit. The Whipple upper limit is the maximum found within 1° of the Tibet coordinates and within the EGRET 95% confidence radius. The lines are the upper and lower limits of the spectral index extended out to VHE energies.

gamma rays with the extragalactic background light increases with gamma-ray energy). However, it has been an object of interest at other wavelengths, and detection with the Whipple telescope is possible at that distance (recall H1426 from Chapter 1). Figure 6.2 shows the spectral energy distribution; the infrared points come from [69], [70], and [71], while the x-ray point is from [72]. Since this is an active galaxy, the typical double hump structure is expected, but unfortunately there are not enough data points. (The infrared peak is not to be interpreted as the low energy hump. It is believed to be due to a warm torus surrounding the nucleus [73].) As a result, it is difficult to assign any meaning to the Whipple upper limit.

6.1.3 Tibet14

The EGRET source 3EG J2021+3716 is 0.6° from the Tibet14 coordinates. Recently, this was tentatively identified with the newly discovered pulsar PSR J2021+3651 [74]. The pulsar is just over 1° from the Tibet14 coordinates, and

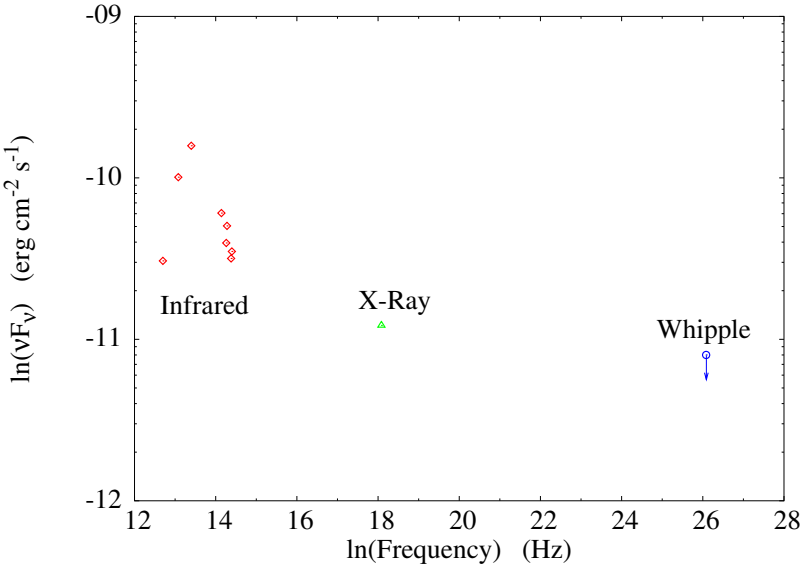

Figure 6.2. Spectral energy distribution for the active galaxy IRAS 13349+2438, showing measurements in the infrared and xray, along with the Whipple upper limit. The Whipple upper limit was calculated at the location of the galaxy. The infrared peak is not to be interpreted as the low energy hump typically found for an active galaxy. Rather, it is believed to be due to a warm torus surrounding the nucleus [73].

so an upper limit was calculated for this position. Figure 6.3 shows the Whipple upper limit in the plot of the spectral energy distribution, along with measurements taken in the radio [74], x-ray [75], and with EGRET [3] (assuming 3EG J2021+3716 corresponds to the pulsar). Since this is a pulsar, a double hump structure is expected, but there are not enough data points to resolve this. As a result, no attempt is made to give a physical interpretation of the Whipple upper limit.

6.1.4 Tibet16 and Tibet0554

For these two targets, there are no objects of interest within 1° of the Tibet coordinates, and therefore, not much can be said. One item of note is the 4σ spot near the bottom of the Tibet0554 significance map. This was found to correspond to a hole in the OFF-source data, and is therefore unlikely to be due to a real source.

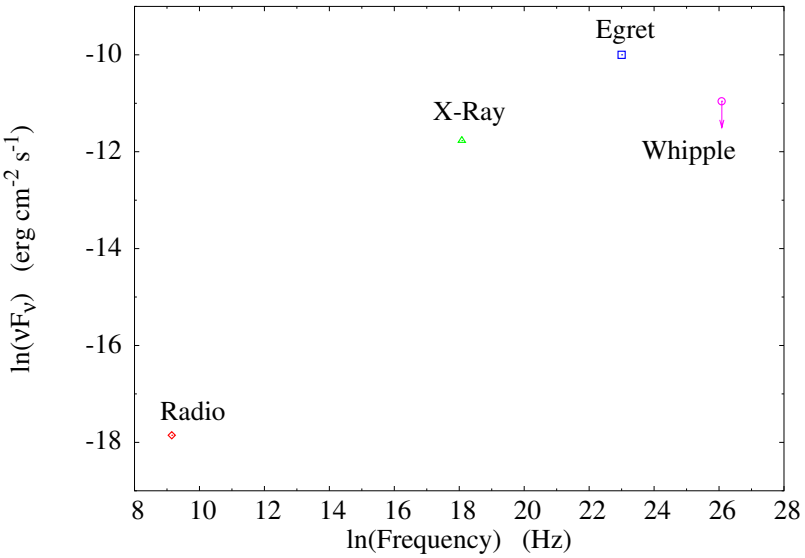

Figure 6.3. Spectral energy distribution for the newly discovered pulsar PSR J2021+3651 showing measurements in radio and x-ray. The EGRET point assumes that 3EG J2021+3716 corresponds to the pulsar. The Whipple upper limit was calculated at the position of the pulsar. Unfortunately, there are not enough points to resolve the expected double hump structure.

6.2 Correlation with the Milagro Sky Survey

The results from Chapter 5 suggest that the Tibet AS gamma-ray source candidates observed by the Whipple telescope were either statistical fluctuations in the Tibet AS data, or the gamma-ray emission was diffuse or episodic. However, a correlation was recently found [49] between the Tibet AS sky survey (1997-1999, covering 10° <Declination< 50°) and an independent survey performed with Milagro (2001-2003, covering 0° <Declination< 80°) [48]. The Tibet AS survey reported the locations of 18 potential gamma-ray sources, while the Milagro survey reported the locations of 9 gamma-ray source candidates. Out of these, three pairs between the two surveys were found to be separated by $\Delta\theta \leq 1.5°$. According to simulations, the chance probability of three such pairings is approximately 10^{-4}. Thus, it strongly appears that one or more of the Tibet AS source candidates is a real TeV gamma-ray source.

One of the pairings corresponds to Tibet14, which was observed by the Whipple

telescope. As was noted in Chapter 5, no point like sources with a Crab-like spectrum were found in the Whipple field of view. However, recent results from Milagro indicate the presence of a diffuse gamma-ray source in the region (angular extent $\sim 5^\circ$) [50]. The Whipple analysis used here is not well suited for an extended source, and a suitable analysis would be difficult because there is no OFF-source data for this region. Therefore, more observations are needed, employing observation and analysis strategies which improve sensitivity to large ($> 2^\circ$) diffuse gamma-ray sources.

6.3 Summary

In VHE gamma-ray astronomy, a considerable amount of time and effort have been devoted to the discovery of new sources. Tibet AS has performed an all-sky survey for this purpose. In the survey, a number of potential TeV gamma-ray sources have been found with implied fluxes near the level of the Crab Nebula. Unfortunately, most or all of these are probably due to stastical fluctuations in the Tibet AS data. However, it is possible that one or more of these potential sources is real, and the high flux levels suggested by the Tibet AS measurements make it sensible to do follow-up observations with the Whipple telescope.

Five gamma-ray source candidates from the Tibet AS all-sky survey have been observed by the Whipple telescope, with observation times ranging from 4.2 hours to 7.9 hours. No point sources with a Crab-like spectrum were found in any of the target regions, and 95% upper limits of 0.2 - 0.3 Crab have been set. For the five targets in question, this suggests that the excess seen in the Tibet AS data was either statistical, or it was due to gamma-ray emission that was episodic or diffuse, or that followed an unconventional (not Crab-like) spectrum.

REFERENCES

[1] T. C. Weekes, *Very High Energy Gamma-Ray Astronomy*, Institute of Physics Publishing, Bristol, 2003.

[2] W. Hermsen, Space Science Reviews **36**, 61 (1983).

[3] R. C. Hartman et al., Astrophysical Journal Supplements **123**, 79 (1999).

[4] N. Gehrels and P. Michelson, Astroparticle Physics **11**, 277 (1999).

[5] C. E. Fichtel et al., Astrophysical Journal **198**, 163 (1975).

[6] G. F. Bignami et al., Space Science Instrumentation **1**, 245 (1975).

[7] C. E. Fichtel et al., Astrophysical Journal Supplements **94**, 551 (1994).

[8] C. Winkler, New Astronomy Review **48**, 183 (2004).

[9] S. Mereghetti et al., The AGILE gamma-ray astronomy mission, in *ESA SP-459: Exploring the Gamma-Ray Universe*, pages 603–606, 2001.

[10] G. R. Ricker and HETE Science Team, Bulletin of the American Astronomical Society **33**, 833 (2001).

[11] N. Gehrels and et. al, Astrophysical Journal **611**, 1005 (2004).

[12] S. Mereghetti, D. Götz, and A. Tiengo, Memorie della Societa Astronomica Italiana **75**, 426 (2004).

[13] G. G. Lichti et al., Baltic Astronomy **13**, 311 (2004).

[14] J. P. Finley and et. al, The Granite III upgrade program of the Whipple Observatory, in *27th International Cosmic Ray Conference (Hamburg: Copernicus)*, edited by K. H. Kampert, G. Heinzelmann, and C. Spiering, volume OG2.5, pages 2827–2830, 2001.

[15] G. Pühlhofer et al., Astroparticle Physics **20**, 267 (2003).

[16] M. Amenomori et al., Astrophysical Journal **598**, 242 (2003).

[17] R. Atkins et al., Astrophysical Journal **595**, 803 (2003).

[18] W. Benbow and The H. E. S. S. Collaboration, Status and Performance of H.E.S.S., in *γ2004 Heidelberg. To be published in AIP Conference Proceedings*, 2004.

[19] F. Krennrich et al., New Astronomy Review **48**, 345 (2004).

[20] D. Horan and T. C. Weekes, New Astronomy Review **48**, 527 (2004).

[21] T. C. Weekes et al., Astrophysical Journal **342**, 379 (1989).

[22] A. M. Hillas et al., The Astrophysical Journal **503**, 744 (1998).

[23] F. Aharonian and et. al, Accepted for publication in the Astrophysical Journal (2004).

[24] O. C. de Jager et al., The Astrophysical Journal **457**, 253 (1996).

[25] M. Punch et al., Nature **358**, 477 (1992).

[26] J. A. Gaidos et al., Nature **383**, 319 (1996).

[27] J. H. Buckley et al., Astrophysical Journal Letters **472**, L9+ (1996).

[28] J. Quinn et al., Astrophysical Journal Letters **456**, L83+ (1996).

[29] M. Catanese et al., Astrophysical Journal Letters **487**, L143+ (1997).

[30] M. Catanese et al., Astrophysical Journal **501**, 616 (1998).

[31] M. Tluczykont and et. al, Observations of 54 Active Galactic Nuclei with the HEGRA Cherenkov Telescopes, in *28th International Cosmic Ray Conference (Tokyo: ICRR)*, edited by T. Kajita, Y. Asaoja, A. Kawachi, Y. Matsubara, and M. Sasaki, volume OG2.2, pages 2547–2550, 2003.

[32] T. Nishiyama and et. al, Detection of a new TeV gamma-ray source of BL Lac object 1ES 1959+650, in *American Institute of Physics Conference Series*, pages 369–+, 2000.

[33] P. M. Chadwick et al., Astrophysical Journal **513**, 161 (1999).

[34] F. W. Stecker, Astroparticle Physics **11**, 83 (1999).

[35] A. Lemiere and The H. E. S. S. Collaboration, AGN observations with H.E.S.S. First results on PKS2155-304 and Mkn421, in *γ2004 Heidelberg. To be published in AIP Conference Proceedings*, 2004.

[36] D. Horan et al., Astrophysical Journal **571**, 753 (2002).

[37] H. Muraishi et al., Astronomy & Astrophysics **354**, L57 (2000).

[38] D. Berge et al., Observations of SNR RX J1713.7-3946 with H.E.S.S., in *γ2004 Heidelberg. To be published in AIP Conference Proceedings*, 2004.

[39] F. Aharonian et al., Astronomy & Astrophysics **393**, L37 (2002).

[40] J. P. Finley and VERITAS Collaboration, AAS/High Energy Astrophysics Division **8**, (2004).

[41] S. Schlenker et al., Discovery of the Binary Pulsar PSR B1259-63 in VHE Gamma Rays with H.E.S.S., in *γ2004 Heidelberg. To be published in AIP Conference Proceedings*, 2004.

[42] K. Tsuchiya et al., Astrophysical Journal Letters **606**, L115 (2004).

[43] K. Kosack and et. al, Astrophysical Journal Letters **608**, L97 (2004).

[44] L. Rolland and The H. E. S. S. Collaboration, Sagittarius A* with HESS, in *γ2004 Heidelberg. To be published in AIP Conference Proceedings*, 2004.

[45] R. Aloisio, P. Blasi, and A. V. Olinto, Journal of Cosmology and Astro-Particle Physics **5**, 7 (2004).

[46] D. Horns, Interpretation of the gamma-ray signal from the Galactic center, in *γ2004 Heidelberg. To be published in AIP Conference Proceedings*, 2004.

[47] M. Amenomori and et. al, A Wide Sky Survey to search for TeV gamma-ray sources by the Tibet Air shower array, in *27th International Cosmic Ray Conference (Hamburg: Copernicus)*, edited by K. H. Kampert, G. Heinzelmann, and C. Spiering, volume 6, pages 2544–+, 2001.

[48] R. Atkins et al., Astrophysical Journal **608**, 680 (2004).

[49] G. Walker, R. Atkins, and D. Kieda, Astrophysical Journal Letters **614**, L93 (2004).

[50] A. Smith and The Milagro Collaboration, Astrophysics With Milagro, in *γ2004 Heidelberg. To be published in AIP Conference Proceedings*, 2004.

[51] M. V. S. Rao and B. V. Sreekantan, *Extensive Air Showers*, World Scientific, Singapore, 1998.

[52] B. Rossi and K. Greisen, Reviews of Modern Physics **13**, 240 (1941).

[53] P. Sokolsky, *Introduction to Ultrahigh Energy Cosmic Ray Physics*, Addison-Wesley, 1989.

[54] A. M. Hillas, Space Science Reviews **75**, 17 (1996).

[55] D. A. Lewis, Experimental Astronomy **1**, 213 (1990).

[56] J. P. Finley et al., The Status of the Whipple 10m GRANITE III Upgrade Program, in *American Institute of Physics Conference Series*, pages 301–+, 2000.

[57] S. M. Bradbury, A. M. Burdett, M. D'Vali, P. A. Ogden, and H. J. Rose, Whipple Telescope observations of the Crab Nebula with a Pattern Selection Trigger, in *26th International Cosmic Ray Conference*, edited by B. L. Dingus, D. B. Kieda, and M. H. Salamon, volume 5, pages 263–266, 2001.

[58] D. J. Fegan, Space Science Reviews **75**, 137 (1996).

[59] P. T. Reynolds et al., Astrophysical Journal **404**, 206 (1993).

[60] T.-P. Li and Y.-Q. Ma, The Astrophysical Journal **272**, 317 (1983).

[61] M. Amenomori et al., Astrophysical Journal Letters **525**, L93 (1999).

[62] M. Amenomori et al., Astrophysical Journal **580**, 887 (2002).

[63] M. Amenomori et al., Astrophysical Journal **532**, 302 (2000).

[64] S. W. Cui, C. T. Yan, and The Tibet ASγ Collaboration, A Wide Sky Survey for TeV gamma-ray Sources by Using the Tibet-III Air Shower Array, in *28th International Cosmic Ray Conference (Tokyo: ICRR)*, edited by T. Kajita, Y. Asaoja, A. Kawachi, Y. Matsubara, and M. Sasaki, volume OG2.2, pages 2315–2318, 2003.

[65] R. W. Lessard, J. H. Buckley, V. Connaughton, and S. Le Bohec, Astroparticle Physics **15**, 1 (2001).

[66] F. Krennrich et al., Astrophysical Journal Letters **560**, L45 (2001).

[67] O. Helene, Nuclear Instruments and Methods **212**, 319 (1983).

[68] K. Enya et al., Astrophysical Journal Supplements **141**, 23 (2002).

[69] L. Spinoglio, M. A. Malkan, B. Rush, L. Carrasco, and E. Recillas-Cruz, Astrophysical Journal **453**, 616 (1995).

[70] T. H. Jarrett, T. Chester, R. Cutri, S. E. Schneider, and J. P. Huchra, Astronomical Journal **125**, 525 (2003).

[71] M. Moshir and et al., IRAS Faint Source Catalogue, version 2.0., in *IRAS Faint Source Catalogue, version 2.0 (1990)*, pages 0–+, 1990.

[72] J. N. Reeves and M. J. L. Turner, Monthly Notices of the Royal Astronomical Society **316**, 234 (2000).

[73] M. Sako et al., Astronomy & Astrophysics **365**, L168 (2001).

[74] M. S. E. Roberts et al., Astrophysical Journal Letters **577**, L19 (2002).

[75] J. W. T. Hessels et al., Astrophysical Journal **612**, 389 (2004).